Metal-doped silicon diodes for radiation sensing applications

by

Joseph Oluwadamilola Bodunrin

submitted in accordance with the requirements for the degree of

DOCTOR OF PHILOSOPHY

in the subject

PHYSICS

at the

UNIVERSITY OF SOUTH AFRICA

SUPERVISOR: PROF. S. J. MOLOI

March 2022

Declaration

Student number: 66205107

I Joseph Oluwadamilola Bodunrin declare that "**Metal-doped silicon diodes for radiation sensing applications**" is my own work and that all the sources that I have used or quoted have been indicated and acknowledged with complete references.

I further declare that I have not previously submitted this work for examination at UNISA for another qualification or at any other higher education institution.

.... 22 / 03 / 2022

SIGNATURE

(Joseph Oluwadamilola Bodunrin) DATE

Acknowledgement

My sincere adulation goes to the almighty God, the author and finisher of faith who graciously granted me the wisdom, knowledge, and understanding to make this journey a success.

With great appreciation, I shall acknowledge my supervisor, Prof. S.J. Moloi for the guidance and consistent support he gave me as his student. He was always accessible and happy to share his valuable knowledge and experience. I was blessed to have a great man who is just not a supervisor, but a teacher that cares so much about my work and my personal well-being.

I am grateful to all staff members of the Physics department for the assistance they offered. Working with them was great fun. I would also like to acknowledge Mr T. Miller and Dr. M. Madhuku of NRF iThemba LABS, Gauteng for their assistance during ion implantation, *RBS* characterisation, and device irradiation. I am also grateful to Prof. M. Diale, Prof. D. Auret, Dr E. Omotosho, and Dr. H. Tanga of the University of Pretoria for the diode fabrication process.

I want to express my gratitude to the National Research Foundation and The World Academy of Science (Grant number 116113) for student funding. I want to thank Dr J.A. Oke, Dr D.O. Idisi, Dr D.A. Oeba, Mr M.O. Mnisi, Mr B.I.T. Bello, and other colleagues in the department for their support and sharing of experience.

I deeply appreciate my lovely parents, Mr and Mrs Bodunrin, for their immerse love and unalloyed support throughout this journey. It has always been a blessing to have such wonderful parents who are always ready to do all to give their wards the best life. To my beautiful siblings, Dr M.O. Bodunrin, Mrs A.E. Adeniji, and their spouses, I am grateful for your unalloyed love and support throughout this journey. I am so blessed to have you guys as my siblings. Oluwadamilola, your consistency is indeed worthy of emulation.

To my friends, Femi, Raphael, Yele, Lanre, Jaji, Funsho, Yomi, Tia, Surprise, Precious, Shoky, Football for Fun guys, Housing Lions guys, and everyone that supported me throughout the programme, I thank you all. I appreciate every genuine comrade out there representing the interest of the masses and fighting for a country that will work for all regardless of your background. My leader, Omoyele Sowore, thank you for being an inspiration.

Dedication

I dedicate this thesis to God almighty and the less privileged out there who cannot afford formal education.

Abstract

Using an ion implantation method, crystalline silicon (Si) of different concentration types (*n*-, *p*-, and *i*-types) was doped with iron (Fe) and cadmium (Cd) metals. Energy dispersive X-ray spectroscopy (*EDS*), X-ray diffraction (*XRD*) and Rutherford backscattering spectrometry (*RBS*) techniques were used to confirm the presence of the doped metals in Si. The effect of Fe- and Cd-doping on the electrical properties of the fabricated Si diodes was investigated using current-voltage (*I-V*) and capacitance-voltage (*C-V*) techniques. The generation and recombination (*g-r*) centres have been induced in Si by metal-doping, as evidenced by a change in diode *I-V* trends from typical exponential to ohmic behaviour. The *C-V* trends, on the other hand, reveal that holes generated by metal-induced defects in Si are immobile, causing electrons stored in the space charge region (SCR) to dominate measured capacitance at a frequency of 5 kHz. *I-V* properties of the metal-doped based Si diodes are less sensitive to 4 MeV proton-irradiation, implying that Fe and Cd suppress radiation damage in Si. The findings in this study suggest that Fe and Cd are promising dopants in a study to improve Si radiation-hardness using a defect-engineering method. As a result, the research is crucial for an ongoing quest to enhance the efficiency of Si radiation detectors for current and future high-energy physics experiments and other applications.

KEY TERMS

Semiconductors; Silicon; Metal-doping; Iron; Cadmium; *EDS*; *XRD*; *RBS*; Schottky diodes; Defects; Current-voltage; Capacitance-voltage; Radiation sensors.

Table of Contents

Declaration ii

Acknowledgement iii

Dedication v

Abstract vi

Chapter 1 1

Introduction 1

1.1 Motivation 1

1.2 Literature review 4

1.3 Novelty statement 8

1.4 Aim and objectives 9

1.5 Thesis outline 9

References 11

Chapter 2 14

Theoretical overview 14

2.1 Silicon crystal structure 14

2.2 Band gap of silicon 15

2.3 Synthesis of silicon 16

2.3.1 Czochralski method 16

2.3.2 Float zone method 17

2.4 Intrinsic and extrinsic silicon 18

2.5 Metal-semiconductor (*m*-*s*) contacts 20

2.5.1 Schottky contact 20

2.5.2 Ohmic contact 23

2.6 Conduction mechanisms in Schottky contacts 24

2.6.1 Thermionic emission (TE) mechanism 25

2.6.2 Tunnelling mechanism 26

2.6.3 Generation and recombination mechanism 27

2.7 Non-ideal characteristics of Schottky diodes 28

2.8 Defects in semiconductors 29

2.8.1 Point defects 29

2.8.1.1 Vacancy defect 30
2.8.1.2 Interstitial defect 31
2.8.2 Surface defects 31
2.8.3 Shallow and deep defects 32
2.9 Radiation damage to detectors 33
References 35
Chapter 3 37
Characterisation Techniques 37
3.1 Materials characterisation 37
3.1.1 Energy dispersive X-ray spectroscopy (*EDS*) 37
3.1.2 X-ray diffraction (*XRD*) 39
3.1.3 Rutherford backscattering spectrometry (*RBS*) 40
3.2 Device characterisation. 43
3.2.1 Current-voltage (*I-V*) 43
3.2.2 Capacitance-voltage (*C-V*) 46
References 50
Chapter 4 52
Experimental details 52
4.1 Material acquisition and preparation 52
4.2 Stopping and range of ions in matter 53
4.3 Ion implantation 55
4.4 Device fabrication 57
4.5 Device characterisation 59
4.6 Device irradiation 60
References 62
Chapter 5 63
Material characterisation results 63
5.1 Energy Dispersive X-ray Spectroscopy (*EDS*) 63
5.1.1 Undoped and Fe-doped Si 63
5.1.2 Undoped and Cd-doped Si 65
5.2 X-ray diffraction (*XRD*) 65
5.2.1 Undoped and Fe-doped Si. 66

5.2.2 Undoped and Cd-doped Si material. 67
5.3 Rutherford backscattering spectrometry (*RBS*) 68
References 72
Chapter 6 73
Device characterisation results 73
6.1 Current-voltage results 73
6.1.1 Fe-doped Si diodes 73
6.1.1.1 *n*-Silicon diodes 73
6.1.1.2 *p*-Silicon diodes 88
6.1.1.3 *i*-Silicon diodes 94
6.1.2. Cd-doped Si diodes 99
6.1.2.1 *p*-Si diodes 99
6.1.2.2 *i*-Si 103
6.2 Capacitance-voltage (*C*-*V*) measurements 106
6.2.1 Fe-doped Si diodes 107
6.2.1.1 *n*-Si diodes 107
6.2.1.2 *p*-Silicon diodes 112
6.2.1.3 *i*-Silicon diodes 116
6.2.2. Effects of Cd dopant 118
6.2.2.1 *p*-Si diodes 118
6.2.2.2 *i*-Si diodes 120
References 123
Chapter 7 126
***I*-*V* characteristics of 4 MeV proton-irradiated Si diodes 126**
7.1 Undoped and Fe-doped *n*-Si diodes 126
7.2 Undoped and Fe-doped *p*-Si diodes 128
7.3 Undoped and Cd-doped diodes 129
References 130
Chapter 8 131
Conclusions and future work 131
8.1 Material characterisation 131
8.1.1 *EDS* measurements 131

8.1.2 *XRD* measurements....132
8.1.3 *RBS* measurements....132
8.2 Device characterisation....132
8.3 Radiation-hardness test....134
8.4 Future work....135
Appendix A....136
Appendix B....139
Appendix C....140
Appendix D....141
Appendix E....142

LIST OF FIGURES

Fig. 2.1: *Crystal structure of Si* 14

Fig. 2.2: *Band structure of Si at T = 300 K. The upper edge of the valence band is at 0 eV. The energetic difference between the lower edge of the conduction band (at X) is separated by 1.12 eV from the upper edge of the valence band* 15

Fig. 2.3: *Schematic of Czochralski-Si crystal puller used for the growth of large crystals* 16

Fig. 2.4: *Schematic of a modern Float zone Si crystal puller used for the growth of large crystal* 17

Fig. 2.5: *Schematic energy band representation of n-type and p-type Si* 20

Fig. 2.6: *Schematic diagrams of energy band of a metal/n- semiconductor with $\phi m > \phi sc$ materials isolated from each other and (a) at equilibrium after metal and semiconductor are in contact (b)* 21

Fig. 2.7: *Schematic diagrams of energy band of a metal/p- semiconductor with $\phi m < \phi sc$ materials isolated from each other and (a) at equilibrium after metal and semiconductor are in contact (b)* 23

Fig. 2.8: *Schematic diagrams of the energy band of a metal/n-type semiconductor with $\phi m < \phi sc$. Materials isolated from each other (a) and at thermal equilibrium after contact (ideal ohmic contact formation). The ohmic contact formation by low barrier height (c) and high doping contacts (d)* 24

Fig. 2.9: *Four basic conduction mechanisms across Schottky-based diodes in forward bias; Thermionic emission (A), tunneling (B), the recombination of the carrier in the depletion region (C), hole injection from the metal (D)* 25

Fig. 2.10: *Schematic diagram of field emission FE and thermionic emission TFE tunnelling through a Schottky barrier based on heavily doped n- semiconductor. forward bias (a) and reverse bias* 27

Fig. 2.11: *A diagram showing the vacancy, Frenkel-pair defects, the vacancy, self-interstitial, substitutional defects* 30

Fig. 2.12: *The vacancy configuration in the diamond lattice. Four bonds are broken to create vacancy (a). When there is one electron per dangling bond (i.e., for the neutral vacancy V^0), they form two new bonds leading to local distortion (b). When an electron is missing (i.e., for the positive vacancy V^+) one of these two bonds is weakened since it contains only one electron. The distortion is thus different from that in the case of V^0 (c). The 'split vacancy configuration (d)* 31

Fig. 3.1: *Schematic of X-ray emission from an atom.* 38

Fig. 3.2: *Schematic of Energy dispersive X-ray spectroscopy.* 39

Fig. 3.3: *Schematic diagram showing the diffraction according to Bragg's law* 40

Fig. 3.4: *Schematic diagram of scattering trajectory of an incident ion*................................41

Fig. 3.5: *iThemba LABS, Gauteng Accelerator Vault floor plan.* 42

Fig. 3.6: *Equivalent circuit representing a reverse-biased detector*......................................48

Fig. 4.1: *2-D TRIM and 3-D TRIM 2013 simulation showing, collision cascade within Si (a), ion range (b), collision events (c), and mode of energy loss (d) of Fe in Si at 160 keV.* 54

Fig. 4.2: *2-D TRIM and 3-D TRIM 2013 simulation showing, collision cascade within Si (a), ion range (b), collision events (c), and mode of energy loss (d) of Cd in Si at 160 keV.*.........55

Fig. 4.3: *Schematic diagram for the Varian-Extrion 200 – 20A2F model ion implanter at iThemba LABS, Gauteng*..57

Fig. 4.4: *The thermal vacuum deposition system used to fabricate the diodes.* 58

Fig. 4.5: *A typical sample showing circular Schottky contact on the top surface and ohmic contact on the back surface for n-Si (a) and p-Si (b) Schottky diodes.*...................................59

Fig. 5.1: *EDS spectra of undoped Si (a), Fe-doped Si material to the fluence of 10^{15} (b), 10^{16} (c), and 10^{17} (d) ion/cm^2.*..64

Fig. 5.2: *EDS spectra of undoped Si (a) and Cd-doped (b) Si material.*................................65

Fig. 5.3: *XRD pattern of undoped (a), Fe-doped Si material to the fluence of 10^{15} (b), 10^{16} (c), and 10^{17} (d) ion/cm^2.*..66

Fig. 5.4: *XRD pattern of undoped (a) and Cd-doped (b) Si material.*....................................68

Fig. 5.5: *RBS full spectrum of Fe-doped Si sample. Inset: Expanded view of the Fe characteristic RBS peak.*..70

Fig. 5.6: *RBS full spectrum of Cd-doped Si sample.* 71

Fig. 6.1: *I-V characteristics of the diodes fabricated on undoped and Fe-doped n-Si in a linear-linear scale. Inset of Fig. 6.1(c) shows the rescaled I-V characteristics of Fe-doped n-Si to the fluence of 10^{16} ion/cm^2.* 75

Fig. 6.2: *Forward and reverse bias ln(I)-V characteristics of diodes fabricated on undoped and Fe-doped n-Si.*..77

Fig. 6.3: *dV/dln(I)-I(a) and H(I)-I (b) characteristics of the diodes fabricated on undoped and Fe-doped n-Si.*..78

Fig. 6.4: *Diode resistances for undoped and Fe-doped n-Si.*...80

Fig. 6.5: *Ideality factor (a) and Schottky barrier height (b)evaluated from ln(I)-V and Cheung's plot as a function of Fe fluence.*..82

Fig. 6.6: *I-V characteristics of the diodes fabricated on undoped n-Si (a), Fe-doped n-Si at a fluences of 10^{15} (b), 10^{16} (c), and 10^{17}(d) ion/cm^2 in a double logarithmic scale.*....................86

Fig. 6.7: *Rectification ratio (a) and series resistance from dV/dln(I)-I, H(I)-I, and Rj-V (b) versus fluence.*...88

Fig. 6.8: *Forward and reverse bias ln(I)-V characteristics of diodes fabricated on undoped and Fe-doped p-Si.*...89

Fig. 6.9: *dV/dln(I)-I (a) and H(I)-I (b) characteristics of the diodes fabricated on undoped and Fe-doped p-Si.*...89

Fig. 6.10: *Diode resistances for undoped and Fe-doped p-Si. Inset: diode resistance for Fe-doped p-Si.* 90

Fig. 6.11: *I-V characteristics of the diodes fabricated on undoped (a) and Fe-doped (b) p-Si in a double logarithmic scale.*...93

Fig. 6.12: Forward and reverse bias ln(I)-V characteristics of diodes fabricated on undoped and Fe-doped i-Si...94

Fig. 6.13: *dV/dln(I)-I (a) and H(I)-I (b) characteristics of the diodes on undoped and Fe-doped i-Si.*...95

Fig. 6.14: *Diode resistances for diodes fabricated on undoped and Fe-doped i-Si.*...............96

Fig. 6.15: *I-V characteristics of the diodes fabricated on undoped (a) and Fe-doped (b) i-Si in a double logarithmic scale.*...98

Fig. 6.16: *Forward and reverse bias ln(I)-V characteristics of diodes fabricated on undoped and Cd-doped p-Si.* 99

Fig. 6.17: *dV/dln(I)-I and H(I)-I plots on undoped p-Si (a) and Cd-doped p-Si diodes (b). Inset: plot of dV/dln(I) and H(I)-I for Cd-doped p-Si diode.* 100

Fig. 6.18: *Diode resistances for undoped and Cd-doped p-Si diodes.*..................................101

Fig. 6.19: *I-V characteristics of the diodes fabricated on undoped p-Si (a) and Cd-doped (b) p-Si in a double logarithmic scale.* 102

Fig. 6.20: *Forward and reverse bias ln(I)-V characteristics of diodes fabricated on undoped and Cd-doped i-Si*. 103

Fig. 6.21: *dV/dln(I)-I and H(I)-I plots on undoped (a) and Cd-doped (b) i-Si diodes.*.........104

Fig. 6.22: *Diode resistances for undoped and Cd-doped i-Si diodes.*..................................104

Fig. 6.23: *I-V characteristics of the diodes fabricated on undoped (a) and Cd-doped (b) i-Si in a double logarithmic scale.*...106

Fig. 6.24: *C–V characteristics of diodes fabricated on undoped n-Si (a), n-Si doped with Fe to a fluence of 10^{15} (b), 10^{16} (c), and 10^{17} (d) ion/cm^2.The inset are the rescaled C-V trend of diodes fabricated on undoped, Fe-doped n-Si to a fluence of 10^{15} and 10^{16} ion/cm^2.* 108

Fig. 6.25: *C^{-2}–V characteristics of diodes fabricated on undoped n-Si (a), Fe-doped n-Si to a fluence of 10^{15} (b), 10^{16} (c), and 10^{17} (d) ion/cm^2*......110

Fig. 6.26: *C–V characteristics of diodes fabricated on undoped (a) and Fe-doped p-Si (b) with a frequency of 5kHz.* 113

Fig. 6.27: *C^{-2}–V characteristics of diodes fabricated on undoped (a) and Fe-doped p-Si (b) with a frequency of 5kHz*......114

Fig. 6.28: *C–V characteristics of diodes fabricated on undoped (a) and Fe-doped (b) i-Si with a frequency of 5kHz.* 117

Fig. 6.29: *The C^{-2}–V characteristics of diodes fabricated on undoped (a) and Fe-doped (b) i-Si with a frequency of 5kHz.* 118

Fig. 6.30: *C–V characteristics of diodes fabricated on undoped (a) and Cd-doped p-Si (b) with a frequency of 5kHz.* 119

Fig. 6.31: *C^{-2}–V characteristics of diodes fabricated on undoped (a) and Cd-doped (b) p-Si with a frequency of 5kHz*......120

Fig. 6.32: *C–V characteristics of diodes fabricated on undoped (a) and Cd-doped (b) i-Si with a frequency of 5kHz.* 121

Fig. 6.33: *The C^{-2}–V characteristics of diodes fabricated on undoped (a) and Cd-doped (b) i-Si with a frequency of 5kHz.* 121

Fig. 7.1: *ln(I)-V characteristics of the diodes fabricated on undoped (a), Fe-doped n-Si to the fluence 10^{15} (b), 10^{16} (c), and 10^{17} (d) ion/cm^2 prior to and after proton-irradiation*......127

Fig. 7.2: *ln(I)-V characteristics of the diodes fabricated on undoped (a) and Fe-doped (b) p-Si prior to irradiation and after irradiation*......129

Fig. 7.3: *ln(I)-V characteristics of the diodes fabricated on undoped (a) and Cd-doped (b) p-Si prior to irradiation and after irradiation.* 129

LIST OF TABLES

Table 4.1: Details of the Silicon wafers used in this work. 52

Table 5.1: Crystallographic data of phases present in the undoped and Fe-doped Si material. 67

Table 5.2: Crystallographic data of phases present in the Cd-doped Si material. 68

Table 6.1: Device parameters evaluated using different methods for diodes fabricated on undoped and Fe-doped *n*-Si to the fluences of 10^{15}, 10^{16}, and 10^{17} ion/cm^2. 80

Table 6.2: Device parameters evaluated using different methods for diodes fabricated on undoped and Fe-doped *p*-Si. 91

Table 6.3: Device parameters evaluated using different methods for diodes fabricated on undoped and Fe-doped *i*-Si. 96

Table 6.4: Device parameters evaluated using different methods for diodes fabricated on undoped and Cd-doped *p*-Si. 101

Table 6.5: Device parameters evaluated using different methods for diodes fabricated on undoped and Cd-doped *i*-Si. 105

Table 6.6: Diode parameters evaluated from C^{-2}-V plots for diodes fabricated on undoped and Fe-doped *n*-Si to different fluences. 112

Table 6.7: Diode parameters evaluated from C^{-2}-V plots for diodes fabricated on undoped and Fe-doped *p*-Si. 114

Table 6.8: Diode parameters evaluated from C^{-2}-V plots for diodes fabricated on undoped and Fe-doped *i*-Si. 117

Table 6.9: Diode parameters evaluated from C^{-2}-V plots for diodes fabricated on undoped and Cd-doped *p*-Si. 119

Table 6.10: Diode parameters evaluated from C^{-2}-V plots for diodes fabricated on undoped and Cd-doped *i*-Si. 122

Chapter 1

Introduction

Silicon radiation detectors are employed in a wide range of applications, from high-energy physics experiments (HEPE) research to industrial applications including medical physics for advanced medical diagnostic technologies [1-3]. In recent years, radiation damage to silicon (Si) detectors has gotten a lot of attention [4-8]. The study is being carried out to assess the performance degradation of Si detectors in a variety of applications, including solar cells, military, and space physics [2-4]. While radiation detection technology has progressed for these applications, novel materials for the fabrication of detectors that will meet present and future demands are still needed. Damage to Si occurs when the detectors are in use, necessitating the development of novel materials [9]. Several studies have focused on explaining changes in the electrical properties of detectors in terms of radiation-induced lattice defects [10-12]. A thorough knowledge of detector degradation would lead to the development of appropriate strategies for improving Si properties such that radiation damage is minimized or suppressed completely.

1.1 Motivation

Semiconductors and scintillators are the two main types of radiation sensing materials [1, 13]. As a result of their designs that are highly compact and their energy resolution that is better for gamma-ray spectrometry, semiconductors are employed in HEPE, space, and other applications where energy resolution is critical [1]. Their overall disadvantages include higher cost, low efficiency due to their small size, operational complexity, and the requirement for exceptional pure and defect-free crystals in order to achieve complete charge transmission over long distances. Scintillators, on the other hand, are used in cases where energy resolution is less critical than cost and size. They are more powerful for field development, as demonstrated by their employment in oil-well logging [14] and they are the only option for detectors that require large areas of arrays to achieve geometric efficiency [1]. Medical imaging and stand-off security are two examples of scintillator applications. The fluorescence efficiency (large light yield per unit energy) and fluorescence speed of a scintillator material determine its quality [1].

Semiconductors are preferred to scintillators because their electrical properties can be altered by introducing dopants, which in turn affect the conductivity of the material. Carriers that can be collected and recorded with about 100% efficiency are the reason for the semiconductor's efficiency [1]. The energy required to generate carriers (*e-h* pairs) is proportional to the band gap of the material [15]. Other advantages of semiconductors for radiation detection over scintillators include their ability to provide precise position measurement with fascinating readout speed, direct availability of signals in electric form, and the ability to fabricate the detector and readout electronics on the same material [1].

The main elemental semiconductors utilized as radiation sensing materials are silicon (Si) and germanium (Ge), which serve as benchmark materials against which the performance of other semiconductors is measured. Physically, they stand out for their high purity, which is a result of their mono-elemental semiconductor state, making them defect-free to a large extent [16]. Diamond, on the other hand, has a wide band gap (~ 5.5 eV) at room temperature and high carrier mobility, making diamond detectors to collect the data quickly. Furthermore, diamond has demonstrated outstanding radiation hardness. Nonetheless, the high energy (13.1 eV) required for the creation of an *e-h* pair results in relatively weak signals and a lowered signal-to-noise ratio (SNR). Another disadvantage of diamond is its high cost, which is due to a lack of developed technology, as opposed to Si, which has well-developed technology [17].

The band gap of silicon carbide (SiC) is ~ 3.3 eV, allowing it to operate well above room temperature. The *e-h* pair creation energy of SiC, on the other hand, is rather large (8 eV), and carrier mobilities are lower than in Si. In addition, SiC is not a naturally occurring mineral, so it requires excessive furnace techniques to produce the compound from Si [18]. Other compound semiconductors, such as cadmium zinc telluride (CZT), gallium nitride (GaN), and gallium arsenide (GaAs), have been considered and found promising [19-21], but they face a significant challenge in synthesizing crystals of sufficient size and quality due to a high number of impurities that limit the efficiency of the detectors fabricated on them. Due to these flaws, elemental semiconductors surpass compound semiconductors.

Si has been chosen over Ge in radiation sensing applications due to its unique qualities, which include a moderate band gap, low cost due to its abundance in nature, and well-understood technology. Si can be operated up to 150 ^{0}C, while the working temperature of Ge is 70 ^{0}C, hence Si is not easily damaged by excess heat [22-23]. Despite its unique properties, Si still requires tuning in order to reach its full potentials. A defect-engineering of the material has been found promising in improving the radiation hardness of Si in harsh radiation conditions [24]. Defect-engineering of Si entails the deliberate introduction of defects in a regulated manner in order to improve the desired properties while suppressing the detrimental ones. Defect-engineering can be achieved through doping or irradiation. Doping is preferred because parameters like dopant concentration and temperature may be controlled to produce desirable defects [25].

The ion implantation approach was used to dope Si with Fe and Cd in this investigation. The approach was adopted since the depth of the dopants can be controlled by selecting suitable energy and the concentration of dopants. Studies on defect-engineered Si are important to comprehend the impact of dopants (induced defects) on the electrical properties of material-based devices, and thus to choose the best dopant to improve material properties to satisfy present and future demands.

The implanted Si was characterised by *EDS*, *XRD*, and *RBS* techniques to establish the presence of the metals in the material. Schottky diodes were then fabricated on the undoped and metal-doped Si. The fabricated diodes were characterised by *I-V* and *C-V* techniques to investigate a change in the electrical properties of the devices due to Fe- and Cd-doping. This work explains how metal-doping changes diode parameters such as saturation current (I_s), ideality factor (η), Schottky barrier height (ϕ_B), doping density (N_D), built-in voltage (V_{bi}), series resistance (R_s), shunt resistance (R_{sh}), and depletion region width (W_D). These parameters provide information about the diode quality [6] and conduction mechanism [24], as well as metal-induced defect properties in the material.

1.2 Literature review

Si detectors used in HEPE suffer severe radiation damage, resulting in a degradation in their performance [10-11, 14]. When radiation in the range of 1 keV to hundreds of MeV goes through a Si detector, for example, the material gets damaged [12]. Incoming radiation displaces Si atoms from their original position to either substitutional sites or interstitial sites [12].

The sensitivity, energy resolution, and detection efficiency of a radiation-damaged detector are all low [26]. The detector's sensitivity is determined by its ability to establish different ionizing radiation sources [27]. Low-energy radiation, such as alpha and beta radiation, is undetectable by a detector with a low sensitivity [28]. Two adjacent energy peaks cannot be distinguished by a detector with poor energy resolution [27-28]. A radiation-damaged detector is unable to distinguish between two γ-rays of energies 1.12 MeV and 1.13 MeV [28]. Therefore, in applications such as the separation of γ-rays with energy differences of only a few keV, energy resolution is an important consideration when choosing a detector.

The detector's efficiency refers to its ability to convert ionizing radiation into a signal. The efficiency is calculated as the ratio of the density of energetic particles measured to the particle density incident on the detector. [29]. A radiation-damaged detector would not be able to convert all the incident radiation that interacts with the detector volume into a signal. As a result, an unexpected signal emerges that has nothing to do with the radiation that interacts with the detector volume.

Radiation damage causes undesired changes in the detector's electrical properties. The leakage current increases as a result of radiation-induced defects that act as generation and recombination (*g*-*r*) centres. A decrease in the SNR and an increase in power consumption are two negative consequences of high leakage current on detector performance [30]. As a result of the free charge carrier traps created by radiation-induced defects, the detector's effectiveness is reduced. A radiation-hard detector capable of operating in high radiation environments, such as HEPE, is therefore required.

The electrical properties of the irradiated Si have been extensively studied [31,32-36]. The ohmic *I*-*V* behaviour of neutron-irradiated Si-based diodes was explained in terms of the mid gap defect (0.56 eV), defect levels created at the centre of the band gap of Si. In addition to the 0.56 eV defect level, neutron-irradiation creates defect levels at E_{C} -0.42 eV and E_{V} -0.36 eV, where E_{C} and E_{V} are the energies at the bottom of the conduction band and top of the valence band, respectively. These defect levels are responsible for a change in the material's conductivity, affecting the sensitivity of the detector fabricated on the material [27].

An ohmic *I-V* behaviour was observed on neutron-irradiated Si *p-i-n* diodes. Also, the switching voltage and ideality factor increased with neutron fluence [36]. Although, the findings provide recommendations for future radiation-hard detector fabrication, the studies investigated the electrical properties of Si diodes before and after radiation-induced damage by 1 MeV neutrons, hence only damage by neutron-irradiation was considered. As a result, research into the effects of other ionizing radiations, such as protons, on the electrical properties of the material-based devices is required. Understanding the behaviour of device under various ionizing radiations is crucial for practical applications.

The effects of metal dopants such as gold (Au) and platinum (Pt) on the electrical properties of Si have been studied [37-40]. Au, for example, induces three defect levels at E_C + 0.34 eV, E_C – 0.55 eV, and E_V + 0.34 eV [37] in the band gap of Si. Pt, on the other hand, creates three defect levels in Si band gap at E_C – 0.23 eV, E_C – 0.55 eV and E_C + 0.36 eV [38]. It is worth noting that Au and Pt induce a common defect level at 0.55 eV, which is close to the centre of the Si band gap. Defect levels located at the centre of the band gap of Si (0.56 eV) are responsible for the radiation hardness of the material-based detector [39]. Furthermore, Au and Pt have demonstrated the ability to suppress the effects of radiation damage to Si [40, 41]. However, due to their high cost, these metals are prohibitively expensive for research. Furthermore, Au and Pt create other defect levels at E_C + 0.36, E_V + 0.34 and E_C + 0.23 eV, which change the material's conductivity, thereby reducing the sensitivity of the detector fabricated on Si. These shortcomings have prompted an urgent search for alternative dopants in an effort to improve the properties of Si for radiation sensing applications.

Iron (Fe) is a common element in nature that belongs to the transition metal group. Fe has an electronic configuration of {Ar}$3d^6$ $4s^2$ with two valence electrons. The properties of Fe in Si have been previously investigated [42-45]. Fe diffuses interstitially in Si, introducing defect levels in the band gap at E_V + 0.40, E_C + 0.27 eV and E_C – 0.55 eV [42-43]. The Fe-induced defect level at E_V + 0.40 is responsible for minority carriers. These carriers recombine with the excess majority carriers, reducing the density of majority carriers in *n*-Si and increasing the resistivity of the material. The Fe-induced defect levels at E_C + 0.27 eV and E_C – 0.55 eV are donor levels and are expected to increase the density of charge carriers, hence lowering the resistivity of the device fabricated on Fe-doped *n*-Si. As a result, the effects of Fe doping on the resistivity of the material are important to fully comprehend the properties of Fe in Si.

Cd is a group II element with two valence electrons and an electronic configuration of {Kr}$4d^{10}5s^2$. The properties of Cd in Si have previously been investigated [46-49]. These studies demonstrate that Cd is a double acceptor with levels at $E_C - 0.54$ eV and at $E_C - 0.33$ eV attributed to substitutional Cd [46]. These acceptor levels are expected to increase(decrease) the resistivity of *n*-Si (*p*-Si). Cd is a lifetime killer, similar to heavy metals, Au and Pt, and it creates recombination centres in Si [47]. After doping Si with Cd, it is expected that the density of charge carriers would reduce, resulting in an increase in material resistivity. Shallow donor levels are attributed to intrinsic interstitial Cd atoms and oxygen vacancies in Si material [48-49]. The resistivity of *p*-Si (*n*-Si) should increase (decrease) due to these donor levels. A study of the electrical characteristics of diodes fabricated on Cd-doped Si is of interest to understand a change in material conductivity due to Cd doping.

The defect levels of main interest induced by Fe and Cd in Si are $E_C - 0.55$ eV and $E_C - 0.54$ eV, respectively. These defect levels are at the Si band gap's centre. The defect levels are comparable to those induced by Au [38] and Pt [50] and they are responsible for the material's relaxation behaviour [51]. Diodes fabricated on a relaxation material have been reported to have ohmic *I-V* behaviour with high electrical resistivity and to be resistant to radiation damage [35, 42]. The *I-V* and *C-V* characteristics of the diodes fabricated on Fe and Cd-doped Si diodes have never been reported before to our knowledge. This is why the research is being carried out.

1.3 Novelty statement

There have been no studies that have looked at the effects of Fe- and Cd-doping on three different Si concentration types (*n*-, *p*- and *i*-type). The comparison of the three concentration types will reveal the effects of metals on the electrical properties of devices fabricated on the materials.

This study describes how metal-doping alters the charge conduction mechanisms of the Si diode. Though the effects of metals such as Au and Pt on the electrical properties of diodes have been reported, charge distribution mechanisms have never been used to explain a change in diode behaviour caused by metals.

The effects of Fe- and Cd dopants on the *I-V* and *C-V* characteristics of the Si diode are investigated for the first time in this work. For a study on the fabrication of efficient Si-based radiation detectors using the defect-engineering method, these metals are expected to give possible alternative dopants to the relatively expensive ones, Au and Pt.

This work presents new results on the effects of proton-irradiation on the electrical properties of Fe and Cd-doped Si based diode. Exposing fabricated devices to incident particles is imperative for assessing their radiation sensing properties and radiation-hardness.

The effects of irradiation on the electrical properties of undoped and metal-doped Si-based diodes are presented. Even though the *I-V* and *C-V* properties of the irradiated diodes have been published, no correlation between diode behaviour and charge distribution mechanisms in the material has been explained. A study of charge distribution in the material is essential in understanding the effects of irradiation on Si-based devices.

1.4 Aim and objectives

The aim of this research is to determine the effects of metal-doping on the electrical properties of Si-based devices in order to improve the radiation hardness of Si. Doping crystalline Si of different concentration types (*n*-, *p*-, and i- types) with Fe and Cd is one of the specific goals. Material characterisation techniques such as *EDS*, *XRD*, and *RBS* is carried out to establish the presence and depth profiles of the dopants in the crystalline Si. Devices will be fabricated on unimplanted and metal-implanted Si material. The fabricated devices are characterised with *I-V* and *C-V* techniques to determine the effects of these metal dopants (Fe and Cd) on the electrical properties of the Si-based devices. Devices will be subjected to proton-irradiation before being re-characterised using the *I-V* technique to establish the radiation hardness of the fabricated devices.

1.5 Thesis outline

There are eight chapters in this thesis. Chapter 1 contains the thesis's introduction, as well as the motivation, novelty statement, aim, and objectives.

Chapter 2: It briefly covers the fundamental physics of semiconductors, such as the semiconductor theory, which covers the crystal structure, energy band, and the techniques involved in its production. This chapter covers current mechanisms and carrier recombination. The formation of metal-semiconductor contacts, such as, Schottky and Ohmic contacts, as well as their conduction mechanisms, are also covered in this chapter. Finally, the chapter presents semiconductor defects and how they affect the detector's performance.

Chapter 3: It focuses on the theory behind experimental techniques like *EDS*, *XRD*, and *RBS*, which are used to characterise materials. The experimental setup for device characterisation (*I-V* and *C-V*) techniques is also presented in this chapter.

Chapter 4: It focuses on the experimental details and the SRIM/TRIM simulations.

Chapter 5: This chapter discusses the results obtained based on material characterisation techniques.

Chapter 6: The *I*-*V* and *C*-*V* results acquired from device characterisation techniques are analysed in this chapter.

Chapter 7: The findings of the radiation-hardness test of Si-based devices due to Fe and Cd doping are presented in this chapter.

Chapter 8: The important discoveries and their implications for detector applications in general are summarized in this chapter. This chapter also included future projects.

References

[1] B. D. Milbrath, A. J. Peurrung, M. Bliss, and W. J. Weber, *J. Mater. Res.*, **23** (2008) 2561.

[2] J. C. McDonald, B. Coursey, and M. Carter, *Phys. Today*, **57** (2004) 42028.

[3] T. Gozani, *Nucl. Instr. Meth. Phys. Res. Sect. B Beam Interact. with Mater. Atoms*, **213** (2004) 460.

[4] C. Damerell, *Nucl. Instr. Meth. Phys. Res. Sect. A Accel. Spect., Detect. Assoc. Equip.*, **226** (1984) 26.

[5] F. S. Goulding and Y. Stone, Semiconductor radiation detectors, *Science*, **170** (1970) 280.

[6] M. Bruzzi, *IEEE Trans. Nucl. Sci.*, **48** (2001) 960.

[7] S. Kumar, B. A. Reshi, and R. Varma, *Results Phys.*, **11** (2018) 461.

[8] J. O. Lubenau and D. J. Strom, *Health Phys.*, **83** (2002) 155.

[9] F. Shimura, Semiconductor silicon crystal technology, *Academic Press Inc.*, California, 2012.

[10] B. K. Jones, J. Santana, and M. McPherson, *Nucl. Instr. Meth. Phys. Res. Sect. A Accel. Spect., Detect. Assoc. Equip.*, **395** (1997) 81.

[11] Y. Gurimskaya, P. D. de Almeida, M. F. Garcia, *et al.*, *Nucl. Instr. Meth. Phys. Res. Sect. A Accel. Spect., Detect. Assoc. Equip.*, **958** (2020) 162221.

[12] C. Leroy and P.G. Rancoita, *Reports Prog. Phys.*, **70** (2007) 493.

[13] S. N. Ahmed, Physics and engineering of radiation detection, *Academic Press In,* California, 2007.

[14] M. J. Weber, *J. of Lumines.*, **100** (2002) 35.

[15] R. Devanathan, L. R. Corrales, F. Gao, and W. J. Weber, *Nucl. Instr. Meth. Phys. Res. Sect. A Accel. Spect., Detect. Assoc. Equip.*, **565** (2006) 637.

[16] A. Perez-Andujar and L. Pibida, *Appl. Radiat. Isot.*, **60** ((2004)) 41.

[17] H. Kagan, *Nucl. Instr. Meth. Phys. Res. Sect. A Accel. Spect., Detect. Assoc. Equip.*, **541** (2005) 221.

[18] N. Kondrath and M. K. Kazimierczuk. *Intl. J. of Electron. and Telecommun.* **56** (2010) 231.

[19] A. Owens, A. Barnes, R. A. Farley, M. Germain, and P. J. Sellin, *Nucl. Instr. Meth. Phys. Res. Sect. A Accel. Spect., Detect. Assoc. Equip.*, **695** (2012) 303.

[20] A. Owens, *J. Synchrotron Radiat.*, **13** (2006) 143.

[21] M. Mansoor, I. Haneef, S. Akhtar, A. De Luca, A., and F. Udrea, *Sensors and Actuators A: Phys.*, **232** (2015) 63.

[22] M. A. Green, J. Zhao, A. Wang, P. J. Reece, and M. Gal, *Nature*, **412** (2001) 805.

[23] A. Owens and A. Peacock, *Nucl. Instr. Meth. Phys. Res. Sect. A Accel. Spect., Detect. Assoc. Equip.*, **534** (2004) 18.

[24] M. Moll, J. Adey, A. Al-Ajili, G. Alfieri, P. P. Allport, *et al.*, *Nucl. Instr. Meth. Phys. Res. Sect. A Accel. Spect., Detect. Assoc. Equip.*, **546** (2005) 99.

[25] S. Müller, H. von Wenckstern, D. Splith, F. Schmidt, and M. Grundmann, *Phys. status solidi*, **211** (2014) 34.

[26] G. Lindström, *Nucl. Instr. Meth. Phys. Res. Sect. A Accel. Spect., Detect. Assoc. Equip.*, **512** (2003) 30.

[27] L. Tao, H. M. Daghighian, and C. S. Levin, *Phys. Med. Biol.*, **61** (2016) 7600.

[28] J. P. Balbuena Valenzuela, Development of innovative silicon radiation detectors, *PhD Thesis*, Barcelona, Inst. Microelectron, Spain, 2012.

[29] R. L. Murray and K. E. Holbert, "Chapter 12 - Radiation detectors," *Nucl. Energy, 7th ed.,* 2015.

[30] M. Bruzzi, J. Adey, A. Al-Ajili, P. Alexandrov *et al.*, *Nucl. Instr. Meth. Phys. Res. Sect. A Accel. Spect., Detect. Assoc. Equip.*, **541** (2005) 189.

[31] P. G. Litovchenko, A. A. Groza, V. F. Lastovetsky *et al.*, *Nucl. Instr. Meth. Phys. Res. Sect. A Accel. Spect., Detect. Assoc. Equip.*, **568** (2006) 78.

[32] S. J. Moloi and M. McPherson, *Nucl. Instr. Meth. Phys. Res. Sect. A Accel. Spect., Detect. Assoc. Equip.*, **632** (2011) 59.

[33] M. Edwards, G. Hall, and S. Sotthibandhu, *Nucl. Instr. Meth. Phys. Res. Sect. A Accel. Spect., Detect. Assoc. Equip.*, **310** (1991) 283.

[34] M. McPherson, B. K. Jones, and T. Sloan, *Semicond. Sci. Technol.*, **12** (1997) 1187.

[35] G. Lindström, M. Ahmed, S. Albergo, *et al.*, *Nucl. Instr. Meth. Phys. Res. Sect. A Accel. Spect., Detect. Assoc. Equip.*, **466** (2001) 308.

[36] M. K. Parida, S. T. Sundari, V. Sathiamoorthy, and S. Sivakumar, *Nucl. Instr. Meth. Phys. Res. Sect. A Accel. Spect., Detect. Assoc. Equip.*, **905** (2018) 129.

[37] S. J. Moloi and M. McPherson, *Phys. B Condens. Matter*, **404** (2009) 2251.

[38] Y. K. Kwon, T. Ishikawa, and H. Kuwano, *J. Appl. Phys.*, **61** (1987) 1055.

[39] B. K. Jones, J. Santana, and M. McPherson, *Solid State Commun.*, **105** (1998) 547.

[40] R. L. Dixon and K. E. Ekstrand, *Radiat. Prot. Dosimetry*, **17** (1986) 527.

[41] M. McPherson, T. Sloan, and B. K. Jones, *J. Phys. D. Appl. Phys.*, **30** (1997) 3028.

[42] C. B. Collins and R. O. Carlson, *Phys. Rev.*, **108** (1957) 1409.

[43] R. M. Baiomy, Electrical Properties of Iron-doped Silicon at Different Stages of Precipitation, *PhD Thesis,* Universit¨at zu G¨ottingen, Germany, 2004.

[44] E. R. Weber, *Appl. Phys. A*, **30** (1983) 1.

[45] K. Graff and H. Pieper, *J. Electrochem. Soc.*, **128** (1981) 669.

[46] S. S. Dyunaidov, N. A. Urmanov, and M. V Gafurova, *Phys. Status Solidi. A, Appl. Res.*, **66** (1981) K79.

[47] M. Naito and T. Kamei, Silicon doped with cadmium to reduce lifetime, Google Patents, Aug. 15, 1978.

[48] Ş. Karataş and F. Yakuphanoğlu, *J. Alloys Compd.*, **537** (2012) 6.

[49] F. Yakuphanoglu, M. Caglar, Y. Caglar, and S. Ilican, *J. Alloys Compd* **506** (2010) 188.

[50] B. Deng and H. Kuwano, *Jpn. J. Appl. Phys.*, **34** (1995) 4587.

[51] B. K. Jones and M. McPherson, *Semicond. Sci. Technol.*, **14** (1999) 667.

Chapter 2

Theoretical overview

The basic theory of Si crystal structure, energy band, and growth techniques will be discussed in this chapter. Carrier transport in semiconductors will be discussed in this chapter. The metal-semiconductor (*m*-*s*) contacts, which include Schottky and ohmic contacts are discussed. The effects of radiation on Si detectors are also discussed in the chapter.

2.1 Silicon crystal structure

Si is an elemental semiconductor found as a major part of granite, sand, clay, and quartz that is produced by reacting carbon and SiO_2 at a temperature of ~ 2200 °C [1]. Si has a band gap of 1.12 eV at room temperature and its properties can be altered by doping it into *n*-type or *p*-type material [2]. As shown in Fig. 2.1, Si has a diamond structure which results from two penetrating face-centred cubic (FCC) lattices displaced by one-quarter of the distance along the diagonal of the cube. It can be regarded as an FCC lattice with a two-point basis [3].

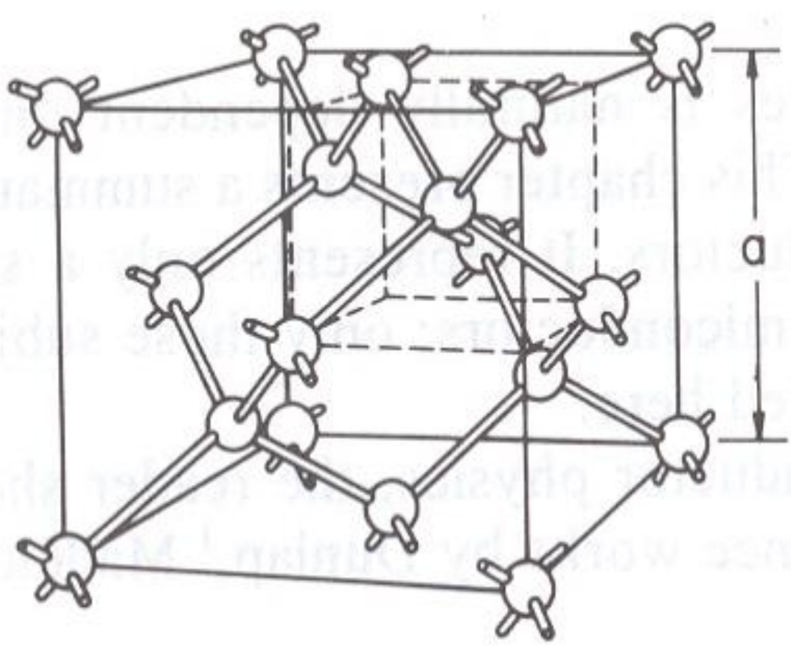

Fig. 2.1: *Crystal structure of Si [4].*

2.2 Band gap of silicon

Semiconductors have a forbidden region in which allowed states cannot exist known as the band gap (E_g). E_g separates the two bands where electron and holes are naturally positioned: the conduction bands above the E_g and the valence bands below the E_g. Fig. 2.2 shows the relationship between energy and momentum (*E*-*k*) for Si. This relationship between momentum and energy can be estimated close to the band minimum/maximum [5] and is given as

$$E(k) = \frac{p^2}{2m^*} \tag{2.1}$$

where p is the momentum and m^* is the effective mass. For Si, the conduction band minimum occurs around [100], where $p \neq 0$ but the valence band maximum occurs at $p = 0$. This indicates that a change in energy and momentum is required for a successful transition of an electron from the valence band to the conduction band in Si. The hole and electron mobilities of bulk-grown Si at room temperature are 450 and 1500 cm^2/Vs, respectively.

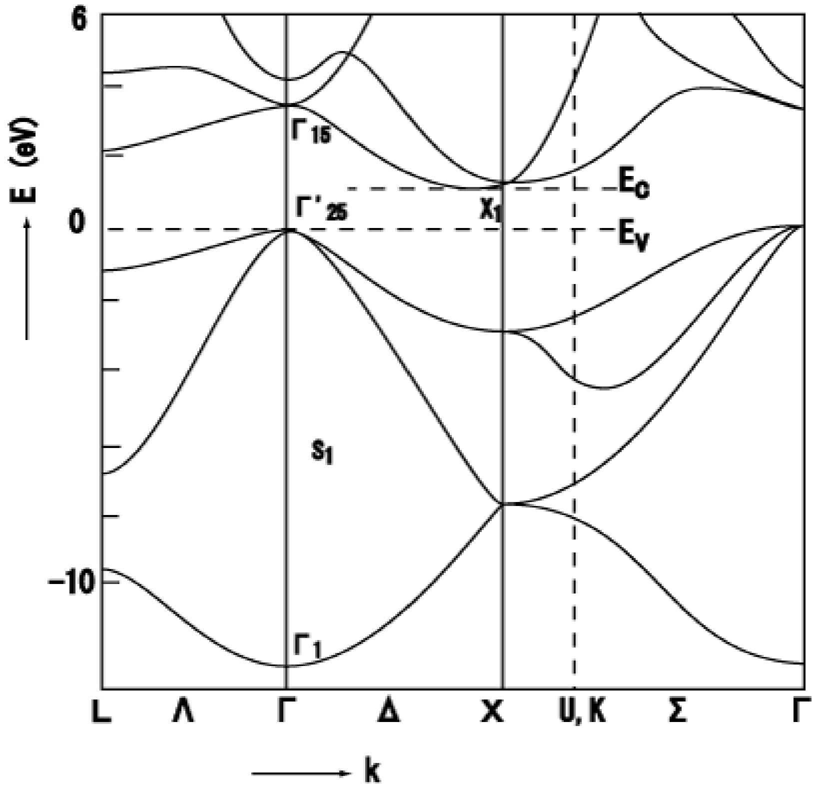

Fig. 2.2: *Band structure of Si at T = 300 K. The upper edge of the valence band is at 0 eV. The energetic difference between the lower edge of the conduction band (at X) is separated by 1.12 eV from the upper edge of the valence band [5].*

2.3 Synthesis of silicon

Czochralski and Float zone methods are employed to produce Si [2]. The Czochralski method is mostly used in the production of highly integrated low power devices, while the Float zone is used for the production of high power devices [6]. The Czochralski method gives better resistance of wafers to thermal stress, low cost, and high concentration of oxygen, while compromising the crystal quality of the material in terms of purity and resistivity [7]. However, when high resistivity and purity material is needed, the Float zone method is favourable but the low concentration of oxygen is a disadvantage because studies have shown that the radiation hardness of the Si detector can be improved when the concentration of oxygen is high [8-9].

2.3.1 Czochralski method

The Czochralski method is used to produce bulk single crystals of Si. The production process starts by putting the feed material into a cylindrically shaped crucible and melted by resistance or radio-frequency heaters. After the feed material is molten, a seed crystal of few diameters in mm is used to touch the molten Si and the ingot is pulled out by removing the seed slowly.

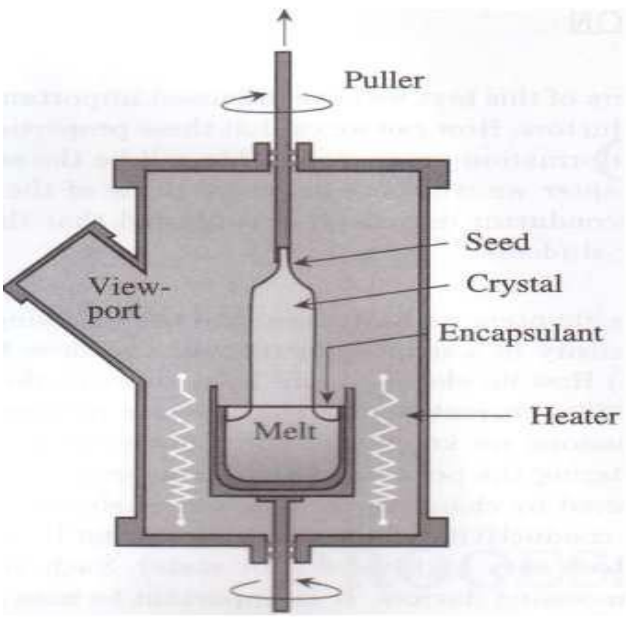

Fig. 2.3: *Schematic of Czochralski-Si crystal puller used for the growth of large crystals [6].*

In order to have a uniform material, the crucible is spun at a speed of about 2 to 50 rotations per minute (rpm). The temperature gradient is adjusted to allow the growth of the crystal on the surface of the seed. In this process, shown in Fig. 2.3, crystals with 0.5 m diameter can be produced. The interstitial oxygen is the most essential impurity, and its concentration rises at the end of the process [10]. The uniformity of the material is largely affected by the thermal gradient in the crucible melt [9], which reduces the crystal perfections. Therefore, due to the high concentration of impurities in the process of production, achieving high resistivity remains a challenge, hence making the Czochralski method not suitable for Si detector production.

2.3.2 Float zone method

Float zone method gives a high-purity alternative to crystals grown by the Czochralski process because the concentration of impurities is extremely low. In the Float zone method, the production takes place under vacuum or in an inert gaseous atmosphere. The process starts with a high-purity polycrystalline rod and a monocrystalline seed crystal that are held face-to-face in a vertical position and are rotated as shown in Fig 2.4. The monocrystalline seed crystal and high-purity polycrystalline rod are partially melted with a radio frequency field.

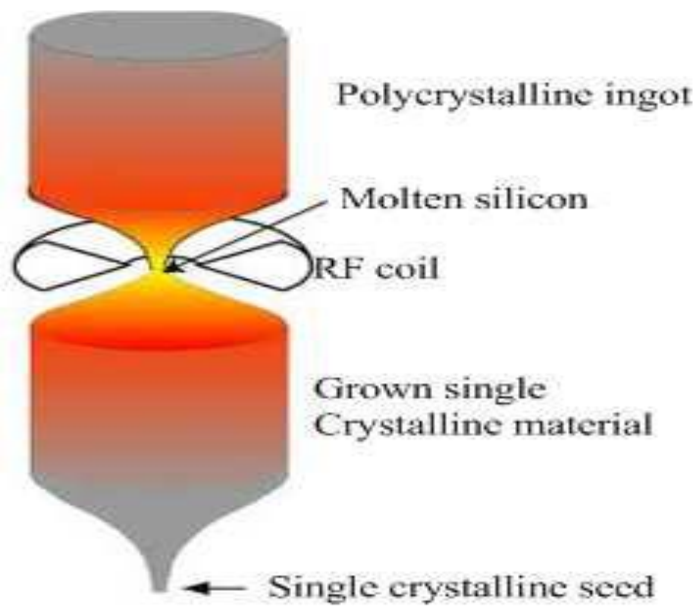

Fig. 2.4: *Schematic of a modern Float zone Si crystal puller used for the growth of large crystal [6].*

The monocrystalline seed is brought up from below to contact the drop of melt formed at the tip of the polycrystalline rod. A necking process is done to form a dislocation free crystal before the neck is allowed to increase in diameter to form a taper and reach the desired diameter for steady-state growth. As the molten zone is moved along the polysilicon rod, the molten Si solidifies into a single crystal and simultaneously, the material is purified [11].

2.4 Intrinsic and extrinsic silicon

Intrinsic Si is an undoped Si without any dopant. It is, however, impossible to have a completely pure semiconductor due to the impurities that are always available during the production process. In an intrinsic Si, the density of electrons in the conduction band is equal to that of holes in the valence band. The conductivity of intrinsic semiconductors depends on the temperature of the material. The Fermi level lies in the middle of the band gap for intrinsic semiconductor. The occupational probability for an energy level is given by the Fermi-Dirac function [12] as

$$F(E) = \frac{1}{1 + \exp\left(\frac{E - E_F}{kT}\right)} \tag{2.2}$$

where E_F is the Fermi energy, k and T are the Boltzmann constant and temperature, respectively.

The densities of free electrons (*n*) and holes (*p*) are given [12] as

$$n = N_C \exp\left(\frac{E_C - E_F}{kT}\right) \text{ and } p = N_V \exp\left(\frac{E_F - E_V}{kT}\right) \tag{2.3}$$

and

$$N_C = 2\left(\frac{2\pi m_e^* kT}{h^2}\right)^{\frac{3}{2}} \text{ and } N_V = 2\left(\frac{2\pi m_h^* kT}{h^2}\right)^{\frac{3}{2}} \tag{2.4}$$

where N_c is the effective density of states in the conduction band and N_v is the effective density of states in the valence band.

Extrinsic Si is formed by the deliberate introduction of specific impurities in the material. The process of adding impurities is known as doping and the impurities added are called dopants.

Doping with a trivalent element such as boron (B), aluminium (Al), and gallium (Ga) make a *p*-type Si. When a Si atom is replaced by an atom of a trivalent element, a hole is created due to the fewer electrons available to bond with Si electrons. This hole can be filled by an electron from a neighbouring atom resulting in a hole where the electron left, and this hole is free for conduction. However, doping with a pentavalent element such as arsenic (As), phosphorus (P), and antimony (Sb) known as donors will produce an *n*-type Si. When an atom of Si is replaced by an atom of a pentavalent element, there is an extra electron that is free after four electrons form a covalent bond with Si, the free electron is available for conduction.

The replacement of the Si atom by different atoms in the lattice comes with the creation of localised energy levels in the band gap. The energy levels can either be donor (E_{D}) or acceptor (E_{A}). E_{D} occurs when the level is formed close to the conduction band (for example, phosphorus $E_{\mathrm{C}} - E_{\mathrm{D}}$ = 0.045 eV) while E_{A} is when the level is formed close to valence band (for example, boron $E_{\mathrm{A}} - E_{\mathrm{V}}$ = 0.045 eV). At room temperature, these energy levels will almost be completely ionized, and the electrons will be able to move to the conduction band or from the valence band to the acceptor level leaving holes in the valence band. The position of Fermi level for *n* and *p*-type Si, respectively, is given [12] as

$$(E_{\mathrm{F}})_{\mathrm{n}} = E_{\mathrm{C}} - kT\ln\left(\frac{N_{\mathrm{C}}}{N_{\mathrm{D}}}\right) \text{ and } (E_{\mathrm{F}})_{\mathrm{p}} = E_{\mathrm{V}} + kT\ln\left(\frac{N_{V}}{N_{\mathrm{A}}}\right). \tag{2.5}$$

The concentration of electrons and holes for a doped semiconductor is given [4] as

$$n = n_{\mathrm{i}} \exp\left(\frac{E_{\mathrm{F}} - E_{\mathrm{i}}}{kT}\right) \text{ and } p = n_{\mathrm{i}} \exp\left(\frac{E_{\mathrm{i}} - E_{\mathrm{F}}}{kT}\right) \tag{2.6}$$

where n_{i} is the intrinsic carrier concentration. The Si energy band representation of extrinsic semiconductors is presented in Fig. 2.5 for *n*- and *p*-type semiconductors.

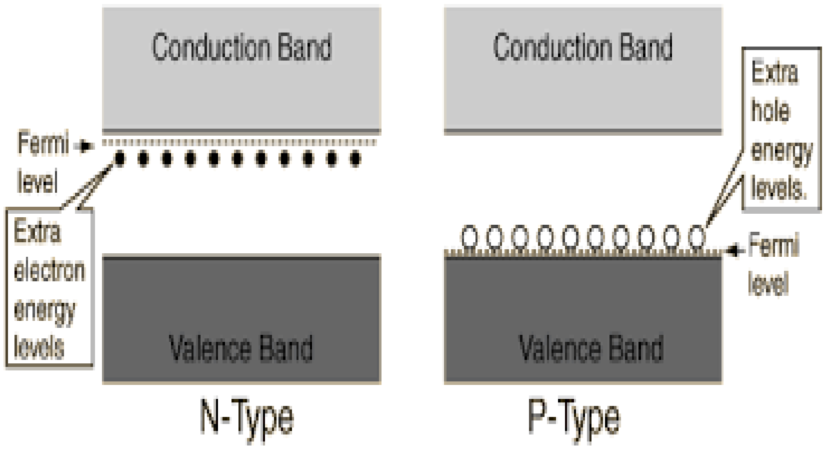

Fig. 2.5: *Schematic energy band representation of n-type and p-type Si [4].*

2.5 Metal-semiconductor (*m-s*) contacts

In the semiconductor industry, metal-semiconductor (*m-s*) contacts are of great interest due to their interesting properties and their enormous applications in electronic devices. The contacts can either be rectifying known as a Schottky contact or non-rectifying known as an ohmic contact.

2.5.1 Schottky contact

According to the Schottky-Mott model [14], the barrier height (ϕ_{Bn}) of an ideal Schottky contact between a metal and an *n*-type semiconductor without surface states is given [15] as

$$\phi_{\mathrm{Bn}} = \phi_{\mathrm{m}} - \chi \quad (2.7)$$

where ϕ_{m} is the metal work function and χ is the electron affinity of the semiconductor material.

Schottky-Mott theory assumes a uniformly doped *n*-type semiconductor and that $\phi_{\mathrm{m}} > \phi_{\mathrm{sc}}$, where ϕ_{sc} is the work function of the semiconductor material. The energy band diagram for an *m-s* contact on an *n*-type semiconductor before contact is formed is illustrated in Fig. 2.6 (a). It can be clearly seen that the energies of the semiconductor electrons are higher those of the metal electrons. When the metal is put in direct contact with a semiconductor, electrons move from the semiconductor to the metal due to the difference in the Fermi levels as a result of higher energies of the semiconductor electrons. The electron transfer will continue until equilibrium is attained, and Fermi levels of metal and semiconductor align. Relative to the Fermi level in the metal, the Fermi level in the semiconductor is lowered by an amount equal to the difference between the two work functions, leading to band bending. This difference between the work functions is the built-in-voltage (V_{bi}) and is given [15] as

$$V_{\mathrm{bi}} = (\phi_{\mathrm{m}} - \phi_{\mathrm{sc}}). \qquad (2.8)$$

An electric field is created due to the negative charge on the surface of the metal repelled by a positive charge of the same amount in the semiconductor. As a result of the relatively low dopant concentration, this positive charge is distributed throughout a barrier region close to the semiconductor surface, to a thickness W_{D} in the semiconductor, known as the depletion region width or SCR width. In the absence of biasing, there is no net movement of electrons over the barrier in either direction because electrons at the Fermi level from both the metal and semiconductor are at the same level as shown in Fig 2.6 (b).

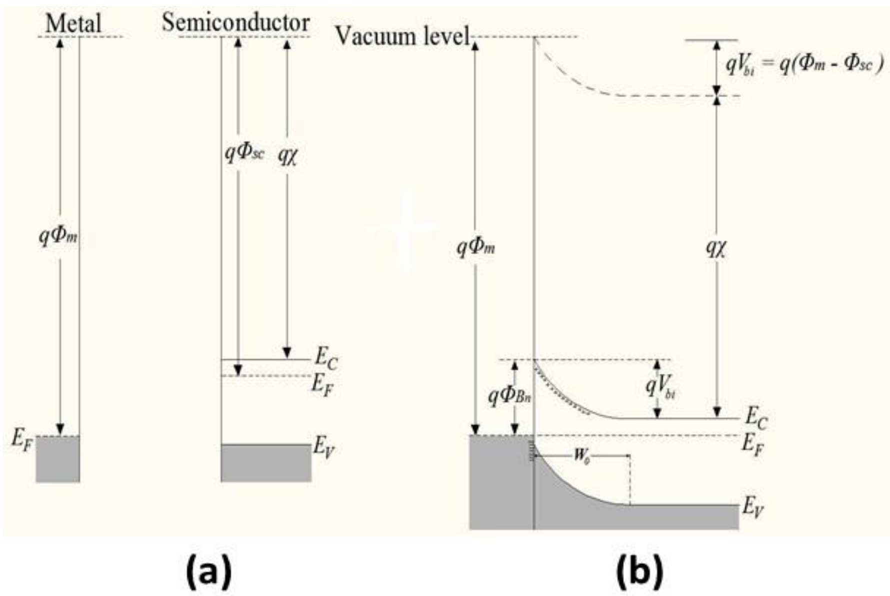

Fig. 2.6: *Schematic diagrams of energy band of a metal/n- semiconductor with* $\phi_m > \phi_{sc}$ *materials isolated from each other and (a) at equilibrium after metal and semiconductor are in contact (b)* [16].

Applying bias voltage in the junction will cause a non-equilibrium condition. For forward biasing condition, a negative potential V_{-} will be applied on the n-type semiconductor side, which will result in the reduction of the band bending. The negative potential V_{-} shortens the barrier for electrons moving from the semiconductor towards the metal making the movement of electrons from semiconductor to metal easier due to the reduction in the barrier. Hence, conductivity is allowed due to easy movement of electrons. For reverse biasing condition, a positive potential V_{+} will be applied to the n-type semiconductor which will increase the barrier. Applying V_{+} will lead to an increase in the depletion region width resulting in a decrease in the density of electrons moving from the semiconductor to the metal because of barrier increase. The barrier seen by electrons from the metal remains the same as the density of electrons crossing from the semiconductor to metal decreases, thereby limiting conductivity.

In case of p-type semiconductors, a barrier is formed between the metal and p-type semiconductors. When the metal and p-type semiconductor are brought into contact, electrons will flow from the metal into the semiconductor until Fermi levels aligns. The movement of electrons from the metal to the semiconductor leads to band bending as Fermi levels aligns. Each electron flowing into the semiconductor removes a hole from the valence band, leaving behind an ionized acceptors in the semiconductor, forming a depletion region in the semiconductor. Fig. 2.7 presents the energy band of a metal/p-semiconductor before and after contact is made. Since the current in p-type semiconductors is carried mainly by holes, the contact is therefore rectifying and in the absence of surface states the barrier height ϕ_{Bp} can be expressed as

$$\phi_{\mathrm{Bp}} = \frac{E_{\mathrm{C}} - E_{\mathrm{V}}}{q} + \chi - \phi_m \tag{2.9}$$

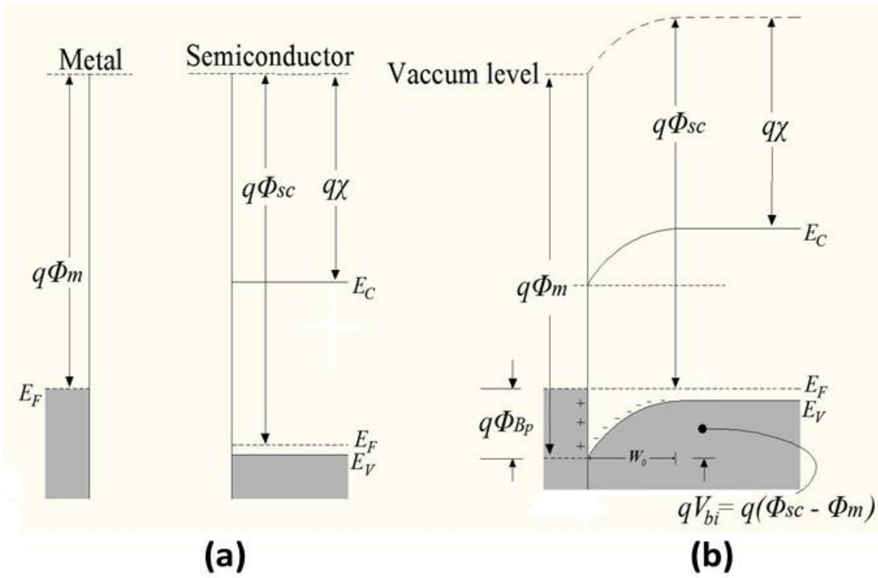

Fig. 2.7: *Schematic diagrams of energy band of a metal/p- semiconductor with* $\phi_{\mathrm{m}} < \phi_{\mathrm{sc}}$ *materials isolated from each other and (a) at equilibrium after metal and semiconductor are in contact (b)* [16].

2.5.2 Ohmic contact

An ohmic contact is an *m-s* contact with a negligible resistance, resulting in a flow of current in both forward and reverse bias. Ohmic contact can be achieved on *n*-type semiconductors with $\phi_{\mathrm{m}} < \phi_{\mathrm{sc}}$ and on *p*-type semiconductor with $\phi_{\mathrm{m}} > \phi_{\mathrm{sc}}$. The isolated semiconductor and metal are shown in Fig. 2.8 (a). After contact, the electrons move from the metal to the semiconductor until thermal equilibrium is attained and both Fermi levels become equal as shown in Fig. 2.8 (b). The movement of electrons will lead to a positive charge on the metal surface and the accumulation of electrons in a layer on the semiconductor side. Fig. 2.8 (c) shows a small barrier, resulting in low-resistance symmetrical contact to the semiconductor. The small barrier allows carriers to flow over the barrier in both directions with little resistance.

Another way to form ohmic contact is when the semiconductor is heavily doped and $\phi_{\mathrm{m}} > \phi_{\mathrm{sc}}$, as shown in Fig. 2.8 (d). When the doping density is increased, the depletion region reduces and thus enhances the tunnelling current through the barrier to form an ohmic-like contact. The required doping density for such contact is 10^{19} cm^{-3} or higher [4].

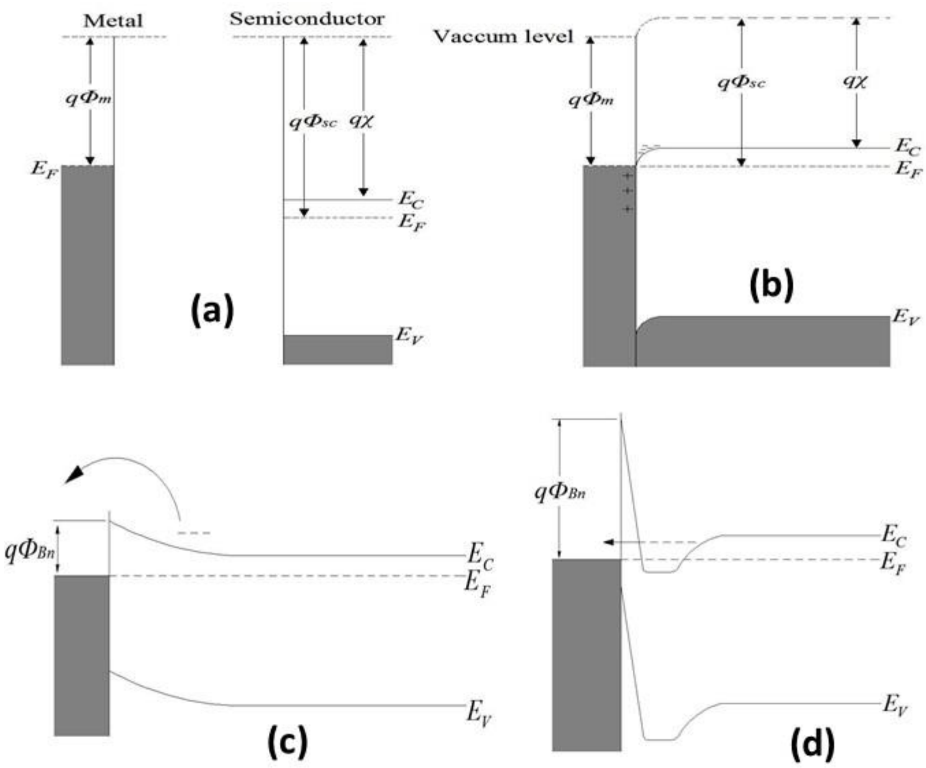

Fig. 2.8: *Schematic diagrams of the energy band of a metal/n-type semiconductor with* $\phi_m < \phi_{sc}$*. Materials isolated from each other (a) and at thermal equilibrium after contact (ideal ohmic contact formation). The ohmic contact formation by low barrier height (c) and high doping contacts (d) [17].*

2.6 Conduction mechanisms in Schottky contacts

The current across a junction barrier results from the movement of charge carriers from the semiconductor to the metal and vice-versa. As shown in Fig. 2.9, in forward bias, the measured current is due to, thermionic emission (TE) of electrons over the barrier (A), tunnelling through the barrier (B), recombination of carriers in the depletion region (C), and recombination of the carrier in the semiconductor's neutral part (D). In an ideal situation, a Schottky diode assumes purely TE current but the contribution of the other conduction mechanism results in a non-ideal behaviour, which is mostly the case in reality [18-19].

For moderately doped semiconductors, the dominant conduction mechanism is TE at room temperature. However, tunnelling dominates at low temperatures and with heavily doped semiconductors. In a given junction, it is possible for all four mechanisms to exist, but only one conduction mechanism dominates.

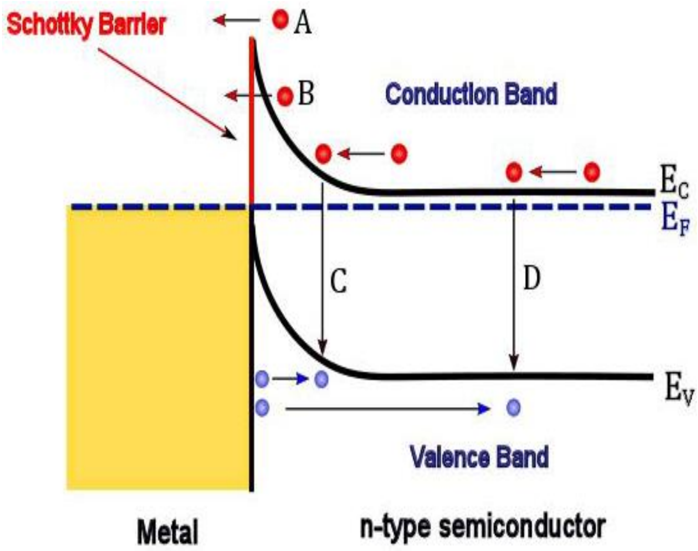

Fig. 2.9: *Four basic conduction mechanisms across Schottky-based diodes in forward bias; Thermionic emission (A), tunneling (B), the recombination of the carrier in the depletion region (C), hole injection from the metal (D) [20].*

2.6.1 Thermionic emission (TE) mechanism

Based on the TE theory, only charge carriers with energies greater than the potential barrier can surmount the junction barrier leading to the current generation. The ideal *I-V* characteristics of a Schottky diode is given [18-19] as

$$I = I_s \left[\exp\left(\frac{q(V - IR_s)}{kT} - 1\right)\right] \tag{2.10}$$

where I_s is the saturation current, q is the electronic charge, R_s is the series resistance, k is the Boltzmann constant, and T is the absolute temperature. I_s is given [18] as

$$I_s = AA^{**}T^2 \exp\left(\frac{-q\phi_B}{kT}\right) \tag{2.11}$$

where A is the active area of the diode, ϕ_B is the Schottky barrier height, and A^{**} is the Richardson constant.

2.6.2 Tunnelling mechanism

The tunnelling mechanism, also referred to as quantum mechanical tunnelling allows electrons with energies lower than the barrier height to pass through the barrier. Quantum tunnelling is mostly observed in heavily doped semiconductors because the Fermi level lies above the bottom of the conduction band, making the potential barrier extremely thin [20]. The tunnelling can occur in both forward and reverse bias directions as shown in Fig. 2.10. The forward bias current results from the tunnelling of electrons with energies at the Fermi level at low temperature, such mechanism is known as field emission (FE) [20]. When the temperature is raised, a notable number of electrons will gain more energies to move above the Fermi level, and the probability of tunnelling increases as the electrons are presented with a thinner barrier.

The tunnelling mechanism due to thermally excited electrons is known as thermionic field emission (TFE). Due to the rapid decrease in the density of electrons above the Fermi level and the decrease in the barrier thickness, the tunnelling probability increases with increasing temperature until a maximum value is reached at a certain energy level (E_{m}). Any further increase in temperature decreases TFE gradually until it becomes negligible where the TE dominates due to the increasing number of thermally excited electrons capable of crossing over the barrier [21]. With moderately doped semiconductors, quantum-mechanical tunnelling only occurs in reverse bias in the form of a TFE mechanism at the top of the barrier where the barrier width gets thinner and thinner with the applied voltage.

The tunnelling current (I_{TU}) is given [18] as

$$I_{\mathrm{TU}} = I_{\mathrm{TU(0)}}\left[\exp\left(\frac{qV - IR_{\mathrm{s}}}{E_0}\right) - 1\right] \tag{2.12}$$

where $I_{\mathrm{TU(0)}}$ is the tunnelling saturation current and E_0 is the tunnelling probability defined [18] as

$$E_0 = E_{00} \coth \frac{E_{00}}{kT} \tag{2.13}$$

where the characteristic tunnelling energy, E_{00}, is given in terms of the doping density (N_D), and the Si dielectric constant, ε_s, as

$$E_{00} = \left(\frac{qh}{4\pi}\right)\left(\frac{N_D}{m^* \varepsilon_s}\right) \tag{2.14}$$

where h is Planck's constant and ε_s is the semiconductor permittivity.

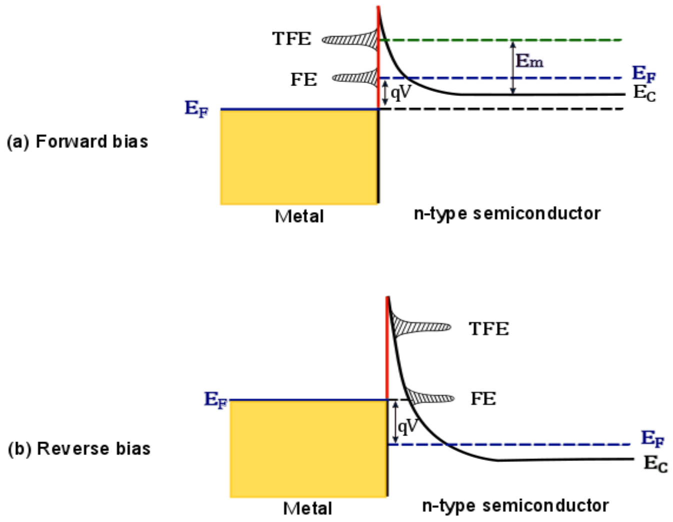

Fig. 2.10: *Schematic diagram of field emission FE and thermionic emission TFE tunnelling through a Schottky barrier based on heavily doped n- semiconductor. forward bias (a) and reverse bias (b) [21].*

2.6.3 Generation and recombination mechanism

The generation and recombination of an electron-hole (*e-h*) pair in the SCR can contribute to the Schottky diode's main current component. At thermal equilibrium, the rate at which *e-h* pairs are generated is equivalent to the rate at which they recombine. Thus, the net current becomes zero where the number of generated *e-h* pair is equal to n_i^2 . The rate of generation departs from n_i^2 when voltage is applied to the barrier. A net generation current or a net recombination current will be formed depending on the bias direction. If a reverse voltage is applied to the Schottky barrier (on the assumption of *n*-type semiconductor), the rate of *e-h* pair generation increases in the SCR. These pairs will be ejected out of the SCR under the effect of the electric field across the barrier producing the reverse current component. When a forward voltage is applied, the electrons will move out from the neutral bulk semiconductor to the SCR and holes will move out from the metal. Electrons will recombine with holes because of their accumulation in the SCR forming a forward recombination current component [20]. Localised centres such as deep trap centres also cause recombination as a result of their energies being close to the middle of the band gap (mid-gap) [20]. The generation-recombination current ((I_{gr}) in the SCR is given [22] as

$$I_{\mathrm{gr}} = I_{\mathrm{R(0)}} \left[\exp\left(\frac{qV - IR_{\mathrm{s}}}{\eta kT}\right) - 1\right]. \tag{2.15}$$

The recombination activity of generation-recombination conduction mechanism is observed in the forward bias and it is expressed [23] as

$$I_{\mathrm{R}} = I_{\mathrm{R(0)}} \exp\left(\frac{qV - IR_{\mathrm{s}}}{\eta kT}\right)\left[1 - \exp\left(\frac{-qV + IR_{\mathrm{s}}}{kT}\right)\right] \tag{2.16}$$

where $I_{\mathrm{R(0)}}$ can be explained in terms of the intrinsic carrier concertation, n_{i}, the recombination lifetime, τ_{r}, and the width of the depletion region W_{D} [24] as

$$I_{\mathrm{R(0)}} = \frac{qn_{\mathrm{i}}W_{\mathrm{D}}}{2\tau_{\mathrm{r}}} \tag{2.17}$$

2.7 Non-ideal characteristics of Schottky diodes

Experimentally, Schottky diode's *I-V* characteristics mostly deviate from the ideal case of the TE model in both (forward and reverse) conditions. To accommodate the non-ideal situation, a factor, η, known as ideality factor is introduced to the ideal Schottky diode equation given in eq. 2.18. For an ideal diode whose current is based purely on TE, the $\eta = 1$. On the other hand, many factors can lead to $\eta > 1$. These factors include the contribution of other current mechanisms such as tunnelling and generation-recombination to the diode's total current. Also, temperature at which the diode is operating, barrier height, and the image-force effect attributed to the bias-dependence are included in the factors [20-21].

$$I = I_s \left[\exp\left(\frac{q(V - IR_s)}{\eta kT} - 1\right)\right]. \quad (2.18)$$

The reverse bias trend also exhibits non-ideal behaviour, which occurs when the reverse current keeps increasing instead of saturating at I_s . This non-ideal behaviour in the reverse bias can be explained by the barrier lowering effect, which can either result from the image force effect or a thin interfacial layer between the metal and semiconductor [20]. The second effect is the tunnelling effect. At moderate reverse bias, the potential barrier becomes sufficiently thin so the electrons can tunnel into the semiconductor before reaching the top of the barrier. In addition, temperature also cause a non-ideal behaviour in reverse bias trend [20].

2.8 Defects in semiconductors

Irrespective of how perfect the production process of a material is, defects will always be present due to the method of production or the inherent precursors' properties. These defects affect the electrical properties of materials such as the resistivity of a semiconductor. The resistivity of a semiconductor relies largely on the impurities available in the semiconductor.

2.8.1 Point defects

Point defects are due to the presence of a vacancy (i.e., an atom is removed from its regular lattice site leaving an empty point on the lattice) or an interstitial (i.e., an atom is in a site different from the regular lattice site). An interstitial defect can either be an intrinsic or extrinsic defect. An intrinsic interstitial defect is when the interstitial atom and the lattice atom are of the same species. An extrinsic interstitial defect on the other hand, is when the interstitial atom and the lattice atom are of different species. The intrinsic and extrinsic defects are crucial in semiconductor crystals. The combination of several point defects like vacancy-impurity complexes, divacancies, and vacancy-donor is also usually classified as point defects. A situation where a vacancy is found close to an interstitial atom is referred to as Frenkel pair defects. Fig. 2.11 shows the interstitial atom, vacancy, substitutional atom, Frenkel-pair defects.

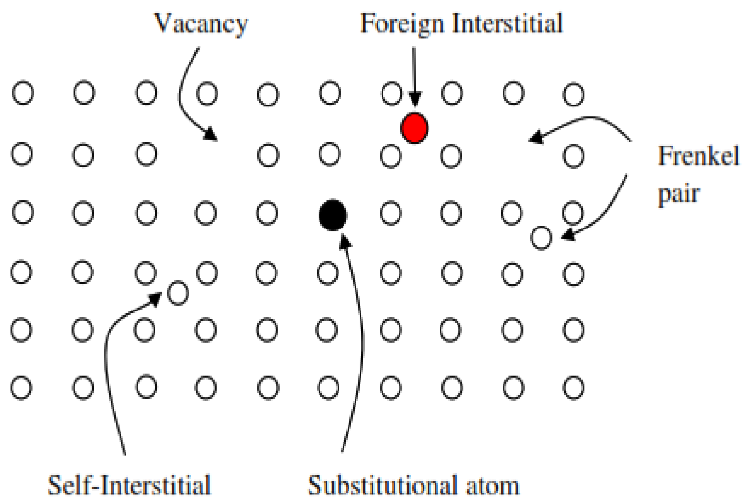

Fig. 2.11: *A diagram showing the vacancy, Frenkel-pair defects, the vacancy, self-interstitial, substitutional defects [25].*

2.8.1.1 Vacancy defect

When an atom is removed from its site in a regular lattice, it creates a void at the point where it is initially positioned known as a vacancy defect (V) [26]. For a vacancy to be formed, four bonds are broken in a diamond crystal structure to remove an atom from its original lattice site, as shown in Fig. 2.12 (a). The broken bonds are available to form new bonds depending on the charge state (i.e., the number of electrons occupying the dangling bonds) of the vacancy (Fig. 2.12 (b and c)). This results in a small inward and outward displacement of atoms in neighbouring sites, which either keeps the local symmetry (relaxation) or changes it (distortion). The amplitude of the displacements is a function of the charge state of the defect. Another geometric configuration for describing a vacancy is the split-vacancy. The split-vacancy occurs when an atom resides at the bond centre between the empty sites [27] as shown in Fig. 2.12 (d). The split-vacancy is often important primarily to help describe the transition state in vacancy migration [28].

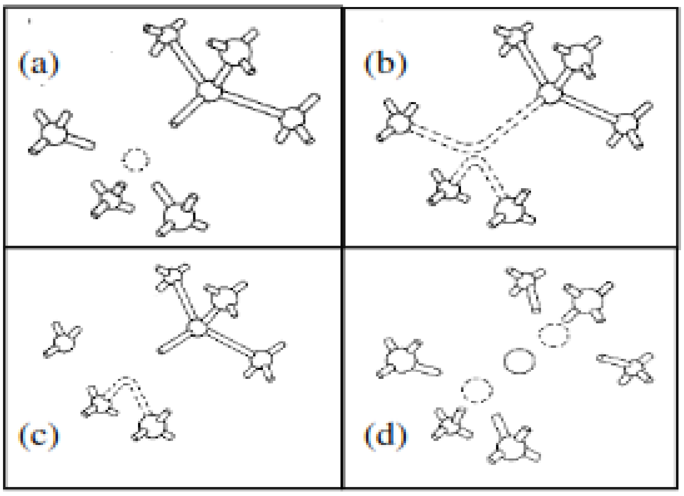

Fig. 2.12: *The vacancy configuration in the diamond lattice. Four bonds are broken to create vacancy (a). When there is one electron per dangling bond (i.e., for the neutral vacancy V^0), they form two new bonds leading to local distortion (b). When an electron is missing (i.e., for the positive vacancy V^+) one of these two bonds is weakened since it contains only one electron. The distortion is thus different from that in the case of V^0 (c). The 'split vacancy configuration (d) [20].*

2.8.1.2 Interstitial defect

Interstitial atoms occupy sites that are not a regular lattice sites causing an interstitial defect. It can either be self-interstitial (i.e., an atom of the same species), or interstitial impurity (i.e., an atom of different species). Generally, interstitials are of high-energy configurations. Also, interstitial defects introduce relaxation and distortion to the lattice that surrounds it. The type of configuration of the interstitial depends on its ability to make bonds with its neighbours and therefore can change with its charge state [25].

2.8.2 Surface defects

A potential source of surface defects is the finite nature of a crystal due to its dangling bonds [29]. As a result of the difference in configuration of these atoms compared to the ones inside the crystal, their contribution to the properties of a material is different. Scattering of electrons and phonons can take place at a crystal's surface [30]. The surface defects may be acceptors or donors resulting from dangling bonds at the surface of the semiconductor [31]. Furthermore, a contaminated surface can generate additional surface defects. The properties of the semiconductor could be modified when exposed to the atmosphere or other environments. This modification is capable of causing carrier trapping and band deformation [32]. The surface states created by surface defects may act as a trap, recombination centres, and scattering centres [32].

2.8.3 Shallow and deep defects

Point defects are electrically active and generate shallow or deep levels within the band gap of a semiconductor. Shallow levels are positioned near their related band edges (conduction band for donors and valence band for acceptors) i.e., about 0.1 eV from the band edge, thus these levels are thermally ionized at room temperature. Elements used as dopants in semiconductors usually generate these shallow levels that become ionized at room temperature and avail free carriers to form *p* or *n*-semiconductor. Electrically active levels with infinitesimal binding energy (typically 10^{-2} eV) are deemed shallow levels [33].

Deep defect levels are situated deeper in the band gap than the dopant levels and are found to bind the carriers much more strongly into highly compact, localized states. The deep levels are with higher ionization energies hereby contributing minimally to the free charge carrier. Traps, recombination centres, or generation centres are defects with deep levels in the band gap. Deep defect levels affect the properties of the semiconductors and therefore, those of the devices fabricated on them. Deep levels are beneficial in some applications, e.g., in fast switching devices, where they can be used as recombination centres that quickly remove minority carriers, thereby increasing the efficiency due to the device's switching speed [3-4]. However, they can also be detrimental in photovoltaic applications since they reduce the cell's efficiency by recombining *e*-*h*. Thus, the deep level study is highly imperative in the semiconductor device industry.

2.9 Radiation damage to detectors

The interaction of high-energy particles with the Si crystal creates point defects and clusters of defects, resulting in degradation of the detector performance. When a Si crystal is exposed to high-energy particle, the primary knock-on atom (PKA) is displaced from its lattice location by an impinging particle, resulting in a vacancy and Si interstitial. Both the interstitial and the vacancy can migrate through the lattice and combine with impurities of the Si bulk, thus forming point defects. The threshold energy for the primary recoil atom to be displaced is E_{d} = 25 eV [34-35]. The energy of the PKA can be substantially higher, and the recoil atom can lose energy through ionization and subsequent displacements as it travels through the Si bulk. While energy loss through ionization normally does not cause significant changes in the Si lattice, non-ionizing interactions prevail at the end of a heavy recoil range, resulting in clusters of defects. The energy threshold to produce cluster formation is ~5 keV [35].

The maximum energy, $E_{R,\max}$ that can be transferred by a particle of mass m_{p} and kinetic energy E_{P} to the recoil Si atom is calculated in the non-relativistic approach by elastic scattering given [34-35] as

$$E_{\mathrm{R,max}} = 4E_{\mathrm{P}}\frac{m_{\mathrm{p}}m_{\mathrm{si}}}{\left(m_{\mathrm{p}}+m_{\mathrm{si}}\right)^2}\ . \tag{2.19}$$

The degradation of the detector depends on the type and energy of the radiation incident on the semiconductor material. The radiation-induced damage can be bulk damage or surface damage.

A degradation in detector properties due to bulk damage includes a change in detector full depletion voltage as a result of a change in effective doping concentration caused by the radiation-induced defects. The full depletion voltage dictates detector operability; hence a high operating voltage will result in complete breakdown of the detector while an operating voltage lower than full depletion voltage will result to charge collection loss [36]. Another degradation in detector properties is an increase in the reverse leakage current, which is caused by the generation of charge carriers in the depleted region due to the radiation-induced defect levels [37]. It has been shown that the leakage current increases with irradiation fluence and they are independent of the substrate material [36]. The high leakage current increases the power consumption of the detector and also degrades the energy resolution thereby reducing the ability to distinguish between radiations with similar energies [38-39].

A conductivity-type inversion, a process where *n*-type changes to *p*-type Si and vice versa, as a result of the induced defects generating a high density of minority charge carriers opposite to the majority carrier in the material. For example, *n*-type Si becomes *p*-type, indicating a generation of a high density of holes in the material. The conductivity-type inversion produces a high electric field region when the bias voltage is applied [40]. The damage in the bulk of the material reduces carrier lifetime, hence reduces the time taken for carriers to remain excited before being recombined. A long carrier lifetime is required for carriers to have sufficient time in the excited state before recombination, hence increasing the diode's efficiency [41].

Surface damage occurs when the charges build-up either at the semiconductor detector surface or overlying electrically insulating layers. These layers consist of thermal oxides on Si and are responsible for heavy surface inversion or accumulation [42]. The energy absorbed by the electronic ionization in the insulating layers generates holes and electrons that diffuse or drift to the other locations where they are trapped. The trapped charge carries produce an unintended concentration of charge carries; consequently, parasitic fields are produced [40-41]. Furthermore, surface damage occurs when the ionizing radiation interacts with the detector, causing oxide damage due to the creation of positive oxide charges at the Si dioxide (SiO_2) - Si interface [42]. In the Schottky diodes, the interface states reduce the mobility of the charge carrier, consequently, reduce the resistivity of the detector [43].

References

[1] M. Kwon, K. Kim, J. Y. Kim, B. H., Park, I. K., Cho *et al.*, *Adv. Mater.*, **20** (2008) 1253.

[2] S. Pizzini, Advanced silicon materials for photovoltaic applications, *Wiley*, Newyork, 2012.

[3] C. Leroy and P. G. Rancoita, Silicon solid state devices and radiation detection, *World Scientific*, 2012.

[4] S. M. Sze, Physics of Semiconductor Devices, *Wileys*, New York, 1981.

[5] J.-M. Jancu, R. Scholz, F. Beltram, and F. Bassani, *Phys. Rev. B*, **57** (1998) 6493.

[6] W. Zulehner, *Mater. Sci. Eng. B*, **73** (2000) 7.

[7] J. Härkönen, E. Tuominen, E. Tuovinen *et al.*, *Nucl. Instr. Meth. Phys. Res. Sect. A Accel. Spect., Detect. Assoc. Equip.*, **514** (2003) 173.

[8] G. Lindström, M. Ahmed, S. Albergo, P. Allport *et al.*, *Nucl. Instr. Meth. Phys. Res. Sect. A Accel. Spect., Detect. Assoc. Equip.*, **466** (2001) 308.

[9] J. Härkönen, E. Tuovinen, P. Luukka, H. K. Nordlund, and E. Tuominen, *Nucl. Instr. Meth. Phys. Res. Sect. A Accel. Spect., Detect. Assoc. Equip.*, **579** (2007) 648.

[10] J. Singh, Semiconductor devices: basic principles, *Wileys*, New York, 2007.

[11] T. F. Ciszek and T. H. Wang, *J. Cryst. Growth*, **237** (2002) 1685.

[12] G. Lutz, Semiconductor radiation detectors, *Springer*, Heidelberg, 2007.

[13] R. J. Archer and M. M. Atalla, *Ann. N. Y. Acad. Sci.*, **101** (1963) 697.

[14] N. F. Mott, *Math. Proceed. of the Cambridge Phil. Society*, **34** (1938) 568.

[15] S. M. Sze, Y. Li, and K. N. Kwok, Physics of semiconductor devices, *Wiley*, New York, 2021.

[16] M. S. Tyagi, Introduction to semiconductor materials and devices, *Wiley*, New York, 2008.

[17] B.G. Streetman and S. Banerjee, Solid State Electronic Devices, *Prentice Hall*, Boston, 2016.

[18] B. L. Sharma, Metal-semiconductor Schottky barrier junctions and their applications, *Springer Science & Business Media*, New York, 2013.

[19] E. H. Rhoderick and R. H. Williams, Metal–Semiconductor Contacts, *Clarendon Press*, Oxford, 1988.

[20] F. Alshaeer, A study of current transport in Schottky diodes based on AlInSb/InSb-QW heterostructures. *PhD Thesis*, Cardiff University, United Kingdom, 2018.

[21] F. A. Padovani and R. Stratton, *Solid. State. Electron.*, **9** (1966) 695.

[22] S. M. Sze and K. K. Ng, Physics of semiconductor devices, *Wileys*, New Jersey, 2006.

[23] S. N. Mohammad and H. Morkoç, *Prog. quantum Electron.*, **20** (1996) 361.

[24] S. Amor, A. Ahaitouf, A. Ahaitouf, J. P. Salvestrini, and A. Ougazzaden, *IOP*

Conference Series: Mat. Sci.and Eng., **186** (2017) 12001.

[25] C. Nyanhere, Characterization of process and radiation induced defects in Si and Ge using conventional deep level transient spectroscopy (DLTS) and laplace-DLTS, *PhD Thesis, University of Pretoria,* South Africa, 2009.

[26] M. Lannoo, *Solid State Sci.*, **22** (1981) 216.

[27] A. Antonelli, E. Kaxiras, and D. J. Chadi, *Phys. Rev. Lett.,* **81** (1998) 2088.

[28] S. A. Centoni, B. Sadigh, G. H. Gilmer, T. J. Lenosky, T. D. de la Rubia, and C. B. Musgrave, *Phys. Rev. B,* **72** (2005) 195206.

[29] J. D. Patterson and B. C. Bailey, Solid-state physics: introduction to the theory, *Springer Science & Business Media,* 2007.

[30] S. G. Davison and S. T. R. Eslicka, Basic Theory of Surface States, *Clarendon Press,* Oxford, 1992.

[31] R. H. Williams, *Surf. Sci.*, **132** (122) 1983.

[32] K. W. Böer, Survey of Semiconductor Physics: Volume II Barriers, Junctions, Surfaces, and Devices, *Springer Science & Business Media,* 2012.

[33] L. V Keldysh, *Sov. Phys. JETP*, **18** (1964) 253.

[34] F. D. Auret and P. N. K. Deenapanray, *Crit. Rev. solid state Mater. Sci.*, **29** (2004) 1.

[35] V. A. J. Van Lint, *Nucl. Instr. Meth. Phys. Res. Sect. A Accel. Spect., Detect. Assoc. Equip.*, **253** (1987) 453.

[36] I. M. Afandiyeva, S. Demirezen, and Ş. Altındal, *J. Alloys Compd.*, **552** (2013) 423.

[37] G. Masetti, M. Severi, and S. Solmi, *IEEE Trans. Electron Devices,* **30** (1983) 764.

[38] G. Casse, P. P. Allport, and M. Hanlon, *IEEE Trans. Nucl. Sci.,* **47** (2000) 527.

[39] I. Hussain, M. Y. Soomro, N. Bano, O. Nur, and M. Willander, *J. Appl. Phys.*, **112** (2012) 64506.

[40] M. McPherson, *Nucl. Instr. Meth. Phys. Res. Sect. A Accel. Spect., Detect. Assoc. Equip.,* **488** (2002) 100.

[41] M. Rizzi, M. D'Aloia, and B. Castagnolo, *J. Appl. Sci.*, **10** (2010) 3141.

[42] C. Verona, G. Magrin, P. Solevi *et al.*, *J. Appl. Phys.*, **118** (2015) 184503.

[43] V. Mikhelashvili, R. Padmanabhan, and G. Eisenstein, *J. Appl. Phys.*, **122** (2017) 34503.

Chapter 3

Characterisation Techniques

Techniques that were used to characterise the samples are discussed in this chapter. The samples include undoped and metal-doped Si wafers. The metals, iron (Fe) and cadmium (Cd), were implanted into Si at an energy of 160 keV. Samples are also devices that were fabricated on undoped and metal-doped Si. The techniques are for material characterisation and device characterisation. Material characterisation is important to understand the materials used in the fabrication of devices while device characterisation will provide insight into how the implanted metals affect the behaviour of the fabricated devices.

3.1 Materials characterisation

Material characterisation techniques that were used to characterise Si material prior to the device fabrication are energy dispersive X-ray spectroscopy (*EDS*), X-ray diffraction (*XRD*), and Rutherford backscattering spectrometry (*RBS*). The techniques were used to investigate the change in elemental compositions, structural properties, and depth profile of the dopants in the Si material. Based on the data acquired, the presence of the implanted metals in Si can be established.

3.1.1 Energy dispersive X-ray spectroscopy (*EDS*)

Energy dispersive X-ray spectroscopy (*EDS*) is a potent analytical technique for determining a sample's chemical characterisation or elemental analysis. This technique is based on the examination of the interaction between an electron beam and the sample. The fact that each element has a unique atomic structure that allows for unique sets of peaks on its X-ray spectrum enables this technique to provide a qualitative analysis [1]. Furthermore, in stimulating the emission of characteristic X-rays from a sample, a beam of X-rays is focused on the sample of interest. As shown in Fig 3.1, the incident electron from the beam excites an electron in the inner shell, causing it to be ejected from the shell and leaving a hole where the electron was formerly positioned. The hole is subsequently filled with electrons from a higher-energy outer shell, and the energy difference between the outer shell and the inner energy shell may be emitted as an X-ray.

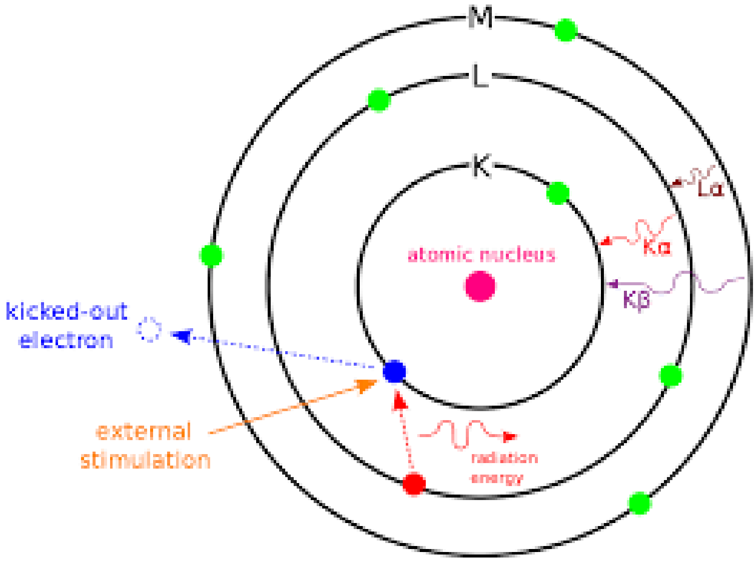

Fig. 3.1: *Schematic of X-ray emission from an atom.*

An energy-dispersive spectrometer determines the amount and energy of X-rays emitted by the sample. The elemental composition of the spectrum can be determined because the energy of the X-rays is a function of the energy difference between the two shells and the atomic structure of the element from which they were released. Elements present in concentrations of > 1% by mass are detectable, although mitigating factors such as spectral overlap can complicate such detection [2]. A schematic describing the *EDS* technique is presented in Fig. 3.2. The *EDS* spectra of the samples in this work were acquired using a JEOL JSM 7800F Field Emission Scanning Electron Microscope (FE-SEM) equipped with an *EDS* situated in the department of Physics, University of South Africa.

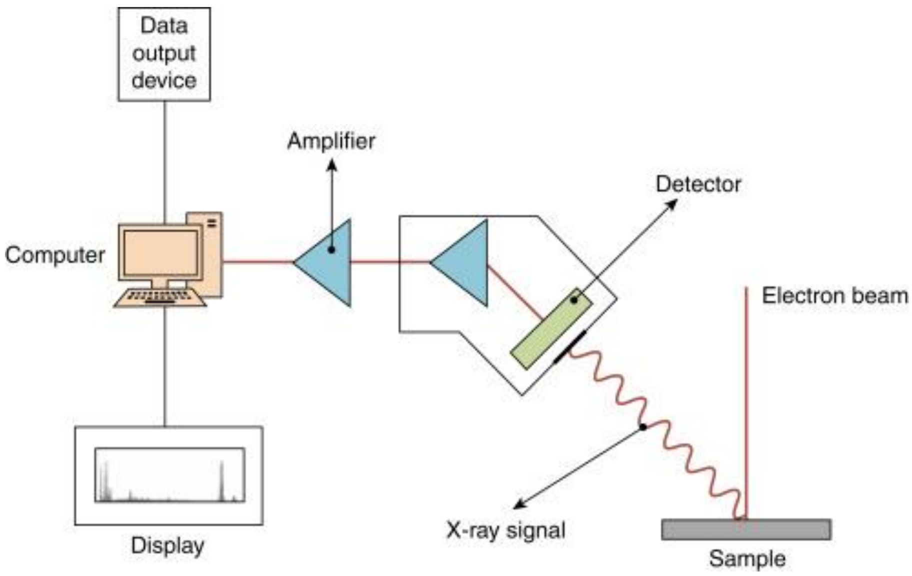

Fig. 3.2: *Schematic of Energy dispersive X-ray spectroscopy.*

3.1.2 X-ray diffraction (*XRD*)

X-ray diffraction (*XRD*) is a principal technique that gives essential information on the crystal structure, phases, and sizes of a given material. This technique relies on the constructive interference of monochromatic X-rays diffracted by a crystalline sample. These X-rays are produced in a cathode ray tube through a heated tungsten filament producing an electron (cathode) which is made to strike a target material usually made of copper (anode). The collisions increase radiation in terms of K_α and K_β Cu X-rays with a wavelength of 0.154 nm and 0.139 nm, respectively. The K_β ray is filtered out with the aid of nickel filament, which absorbs radiations with wavelengths less than 0.150 nm while the K_α rays are collimated and directed on the sample. As shown in Fig. 3.3, when the incident K_α X-rays interact with the sample, constructive interference is produced [3]. As a result, diffraction occurs when the wavelength of the X-rays is in the same order of magnitude as the atomic spacing in the material, and when the scattering centres are spatially distributed in a highly regular way [4]. The X-rays are reflected from a crystal only if the angle of the incident X-rays satisfies the Bragg equation given [5] as

$$n\lambda = 2d\sin\theta \quad (3.1)$$

where n is the reflection number, λ is the wavelength of X-ray used, d is the lattice distance, and θ is the diffracted angle.

The intensity of the X-ray is measured as a function of the diffraction angle, 2θ, and the orientation of the sample [6]. The intensity of the reflected X-rays is recorded, processed, and turned into a diffraction pattern as the sample and detector revolve. This diffraction pattern is used to determine the crystalline phase of the samples and to study their structural qualities. The X-ray diffractometer used in this study was a Rigaku SmartLab X-ray Diffractometer with Cu-Kα radiation (λ = 1.54 Å) located in the Physics Department at the University of South Africa.

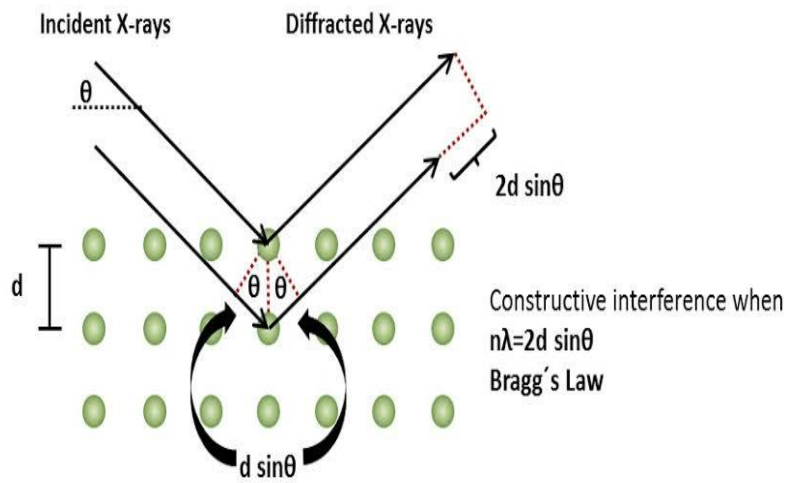

Fig. 3.3: *Schematic diagram showing the diffraction according to Bragg's law [5].*

3.1.3 Rutherford backscattering spectrometry (*RBS*)

Rutherford backscattering spectrometry (*RBS*) is an ion scattering technique used to study the elemental composition in a sample. During *RBS* analysis, high-energy (MeV) He^{2+} ions (i.e., α particles) are focused on the sample and the energies of the backscattered He^{2+} ions at a given angle are measured [7]. The *RBS* spectrum can be used to generate a quantitative compositional depth profile since the backscattering cross-section of each element is known [8]. In the case of elastic collision, the energy of the backscattered ions can be calculated using the conservation of energy and momentum given [9] as

$$E = E_0 K \tag{3.2}$$

where E is the energy of the backscattered particles, E_0 is the energy of the incident particles, and K is the kinematic factor, given [9] as

$$K = \left(\frac{(M_2^2 - M_1^2 \sin\theta)^{\frac{1}{2}} M_1 \cos\theta}{M_1 + M_2} \right)^2 \tag{3.3}$$

where M_1 and M_2 are the incident ion's and target atom's masses, respectively, and θ is the backscattering angle. It can be noticed from eq. (3.3) that K depends on the mass of the incident ion M_1, the mass of the target atom M_2, and the scattering angle θ.

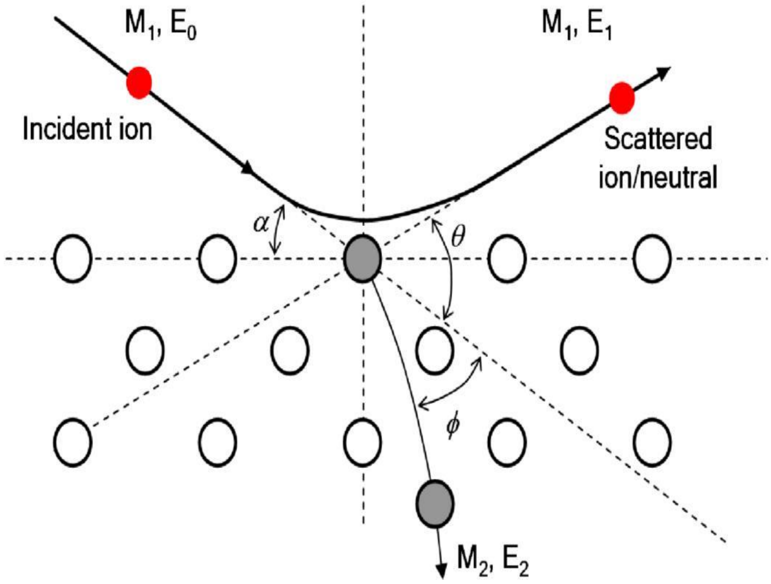

Fig. 3.4: *Schematic diagram of scattering trajectory of an incident ion [10].*

The schematic diagram of the scattering trajectory of an incident ion is presented in Fig. 3.4. The *RBS* detector in the microprobe chamber is positioned at an angle of 150º from the incident direction, and the beam struck the sample normally, i.e., α = 90º and θ = 150º. The output charge signal (which is proportional to the energy of the backscattered ions) is fed into the pre-amplifier, where it is integrated and converted into a voltage signal.

The amplifier and analogue to digital (ADC) are used to amplify the voltage signal before converting it (the amplified voltage signal) from analogue to digital. An *RBS* spectrum of counts (number of backscattered ions registered by the detectors) as a function of the channel number (energy of the detected backscattered ions) is displayed on the computer screen.

In this work, positively charged helium (He^{2+}) ions were used. The basic principle of this technique is that the helium ion source is used to generate negatively charged ions. When a high potential is applied across the accelerator tube, negatively charged ions are accelerated from the ground to the positively charged terminal using a 6 MeV tandem accelerator. Inside the accelerator, a striper gas removes electrons from incoming negatively charged ions and changes their charge state to positive. As they are repelled from the positive terminal voltage and returned to ground potential, the positively charged ions are propelled to higher energies. There are dipole magnets in front of the accelerator that deflect the beam across various beamlines.

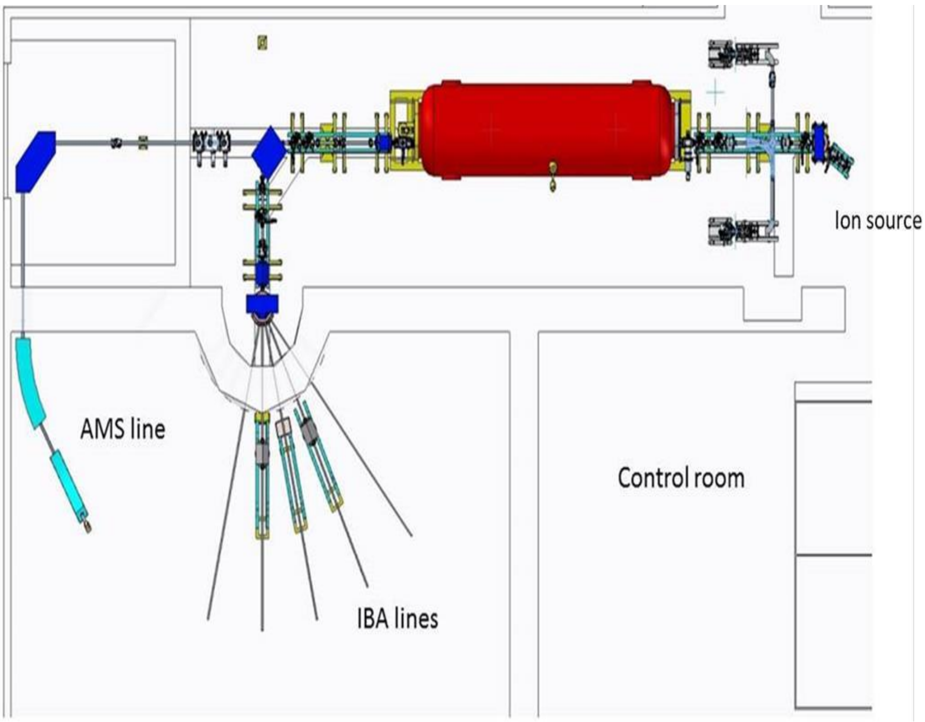

Fig. 3.5: *iThemba LABS, Gauteng Accelerator Vault floor plan [16].*

The beam was focused and directed on the sample located inside the scattering chamber using a combination of vertical and horizontal slits. When the beam (i.e., energy = 2 MeV) hits the target (unimplanted and implanted Si in this study), the incident particles get scattered from the scattering centres of the material and the target atoms get recoiled at an angle, θ, regarding the incident beam. The floor plan of the tandem accelerator, with Ion Beam Analysis (IBA) lines, is shown in Fig. 3.5.

3.2 Device characterisation.

The fabricated devices are Schottky diodes and are characterised by the current-voltage (*I*-*V*) and capacitance-voltage (*C*-*V*) techniques. These techniques provide information about the material's charge density and hence, the properties of the defects induced in the material.

3.2.1 Current-voltage (*I*-*V*)

The *I*-*V* technique is an important tool for investigating the electrical properties in terms of the electrical conductivity of a material and it provides information about the devices by measuring the current passing through the diode as the voltage is varied. The *I*-*V* plots give vital information about the operation of the diode. For example, the trend of the *I*-*V* curve provides information about the breakdown voltage, leakage current, and knee voltage. Breakdown voltage is used to determine the range of the diode's operating voltage [11]. Ideally, the reverse current is always low since it is due to minority carriers, but as reverse voltage increases, it gets to a point where the reverse current starts to increase rapidly. The voltage where the rapid increase in the reverse current occurs is known as the breakdown voltage and at this voltage, the diode is completely damaged [12-13].

The leakage current is another important information obtained from the *I*-*V* curve. The leakage current plays a major role in the sensitivity of the diode. A good diode is expected to have an extremely low leakage current and good sensitivity [14-15]. The knee voltage, also known as the switching-on voltage, is the voltage where the current starts to increase rapidly in forward bias as a result of the junction barrier being surmounted by the applied voltage [14]. The *I*-*V* curve in a semilogarithmic scale enables us to determine the range where the effect of the series resistance is negligible. The conduction mechanism of the diode is also established from the *I*-*V* curve in double logarithmic scale. In general, the *I*-*V* curve provides information about the quality of the diode.

Diode parameters such as ideality factor, saturation current, Schottky barrier height, parasitic resistance, and rectification ratio are also obtained using the *I*-*V* technique. The ideality factor measures the conformity of the diode to pure TE. A case where the ideality factor is greater than unity indicates non-ideal behaviour of the diode, suggesting additional current mechanisms other than TE are involved.

The saturation current is caused by the diffusion of minority carriers from the neutral regions to the depletion region. The variation of the saturation current provides information about the minority carriers density. The Schottky barrier height is the potential needed for an electron to move from a semiconductor bulk to a metal. This parameter confirms the existence of the metal-semiconductor configuration [16] and it can be used to study the properties of charge carriers as a result of the induced defects.

The parasitic resistance in terms of the shunt resistance and series resistance provides information about the diode resistance [17]. An increase in the resistivity of the diode would indicate a recombination or compensation of carriers, resulting in the properties of the induced defects. The rectification ratio provides information on the rectifying behaviour of a diode and its variation can be used to study the quality of the diode.

In an ideal situation, thermionic emission (TE) theory describes the diode current [21-22] as

$$I = I_{\mathrm{s}} \left[\exp\left(\frac{qV}{\eta kT} - 1\right)\right] \tag{3.4}$$

where η=1 and the effect of series resistance (R_{s}) is negligible, the forward *I*-*V* curve is expected to be linear throughout the voltage region. However, this is not the case because the linear trend disappears at high voltage region due to η always being greater than unity and R_s is always present at high voltage region. To account for these non-ideal situations (η>1 and presence of R_s), eq. (3.4) is modified into

$$I = I_s \left[\exp\left(\frac{q(V - IR_s)}{\eta kT} - 1\right)\right] \tag{3.5}$$

where,

$$I_s = AA^{**}T^2 \exp\left(\frac{-q\phi_B}{kT}\right). \tag{3.6}$$

In the above equations, A (=2.83× 10^{-3} cm^2) is the diode active area, A^{**} (= 112 and 32 A cm^{-2} K^{-2}) is the effective Richardson constant for *n* and *p*-type Si, respectively, *T* is the temperature in kelvin, k is the Boltzmann constant, q is the electronic charge, and ϕ_B is Schottky barrier height.

In extracting the diode parameters, Rhoderick assumed that for highly doped semiconductors, the *I*-*V* characteristics at $V > 3kT/q$ can be represented in a simplified form of eq. (6.1) and given [21] as

$$I = I_s \exp\left(\frac{qV}{\eta kT}\right). \tag{3.7}$$

Solving further by linearising will give

$$\ln(I) = \frac{qV}{\eta kT} + \ln I_s \tag{3.8}$$

indicating that a plot of $\ln(I)$-*V* will give a linear trend at the low voltage region where the effect of R_s is negligible. The diode parameters are extracted from the linear region using Rhoderick method [23]. The ideality factor, η, is obtained from the slope of the linear region as

$$\eta = \frac{q}{kT}\frac{\mathrm{d}V}{\mathrm{d}\ln(I)} \tag{3.9}$$

and the saturation current (I_s) is obtained from the y-axis intercept. The Schottky barrier height (ϕ_B) is evaluated [23-24] as

$$\phi_{\mathrm{B}} = \frac{kT}{q}\ln\left(\frac{AA^{**}T^{2}}{I_{\mathrm{s}}}\right). \tag{3.10}$$

The accuracy of the parameters derived using Rhoderick's method cannot be guaranteed because the parameters are extracted from the linear region where the effects of R_{s} are negligible. However, Cheung's method [25] is employed to account for the non-linear region where the effect of R_{s} is noticeable and is given [26] as

$$\frac{\mathrm{d}V}{\mathrm{d}\ln(I)} = \left(\frac{\eta kT}{q}\right) + IR_{\mathrm{s}} \tag{3.11}$$

$$H(I) = V - \left(\frac{\eta kT}{q}\right)\ln\left(\frac{I}{AA^{*}T^{2}}\right) \tag{3.12}$$

and $H(I)$ is given as

$$H(I) = \eta\phi_{\mathrm{B}} + IR_{\mathrm{s}}. \tag{3.13}$$

The value of R_{s} can be obtained from the slope of d*V*/dln(*I*)-*I* plot from eq. (3.11) and η can be calculated from the y-axis intercept. The value of η determined from eq. (3.11) was inserted in eq. (3.13) to obtain the plot of *H(I)-I* and y-axis intercept is used to calculate ϕ_{B}. The slope *H(I)-I* plot can be used for the second determination of R_{s}.

3.2.2 Capacitance-voltage (*C-V*)

The *C-V* technique is another useful tool to investigate the electrical properties of a semiconducting device and it measures the capacitance in the junction of a diode. The *SCR* acts like a capacitor. By varying the applied voltage to the junction, the *SCR* width also varies. The dependence of the *SCR* width upon the applied voltage provides information on the diode's characteristics such as doping profile, doping concentration, full depletion voltage, image force barrier lowering, and Schottky barrier height.

The doping profile provides information on the uniformity of the doping concentration and is determined by the linear regions identified in the C^{-2}-*V* plot. The doping profile can be used to study the properties of the induced defects as a single linear region would indicate a uniform doping profile in the material while multiple linear regions would indicate a non-uniform doping profile.

The doping density is the density of charge carriers responsible for the conductivity in the diode. An increase or decrease in the doping density would provide information on the properties of the induced defects. An increase in the doping density would indicate that the induced defects generate carriers while a decrease would suggest that they are responsible for recombination or compensation of charge carriers. The full depletion voltage (FDV) is the voltage needed to withdraw all charge carriers from the SCR. A variation in FDV would provide information on the properties of the induced defects. High FDV would indicate that a high density of carriers is available in the SCR while a low FDV would indicate that the density of carriers available in the SCR is low. FDV also provides information about the operating voltage of a diode.

The image force barrier lowering provides information about the image charges that accumulate on the metal electrode as charge carriers approach the metal-semiconductor interface. The potential associated with these image charges reduces the Schottky barrier height. Though the value of image force barrier lowering is small in comparison to the barrier height itself, it is still of interest because it is voltage dependent and cause the reverse current to be voltage dependent. This parameter has a direct impact on the Schottky barrier height and the reverse current, hence, useful in the study of the properties of the induced defects.

The electric field is formed as a result of the static charges formed at the boundary as charge carriers move from the semiconductor to the metal. The maximum electric field is at the metal-semiconductor interface [18]. In this electric field that opposes the movement of majority carriers and in the process, the SCR is formed. The SCR width can be used to study the properties of the induced defects. The variation of the width of the SCR indicates recombination or generation of charge carriers available in the SCR as a result of the induced defects.

During the capacitance measurement, for example, a Si diode, the diode is biased with a direct current (DC) voltage. An inductance, capacitance, and resistance (LCR) metre add an alternating current (AC) to the bias voltage. An equivalent circuit representing a reverse-biased diode is shown in Fig. 3.6. The diodes can be described by a capacitor *C* in parallel with a parallel resistor R_p that accounts for the leakage current [19]. In addition, there is a series resistor, R_s, which represents the resistance of the undepleted detector bulk.

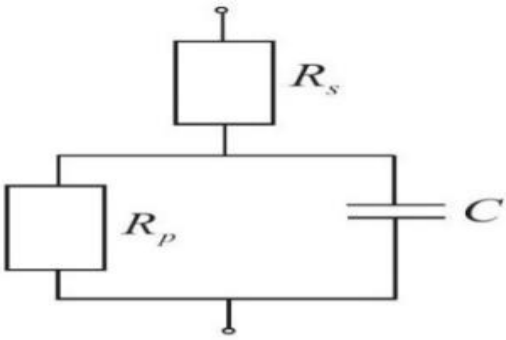

Fig. 3.6: *Equivalent circuit representing a reverse-biased detector [20].*

The capacitance, *C*, of a Schottky diode is a function of the doping concentration, $N_{D(A)}$ in the semiconductor material and is given [21, 26] as

$$C^{-2} = \frac{2(V_{bi} + V)}{q\varepsilon_s\varepsilon_o A^2 N_{D(A)}} \tag{3.14}$$

where V_{bi} is the built-in potential, ε_s is the dielectric constant of semiconductor material, and ε_o is the permittivity in a vacuum.

Ideally, the plot of C^{-2}-*V* should result in a linear graph provided the doping profile is uniform. The V_{bi} is calculated from the voltage-axis intercept while $N_{D(A)}$ is determined from the slope of the linear region of plot C^{-2}-*V*. However, in most cases, the doping profile is not uniform, resulting in two or more linear regions in C^{-2}-*V* plot. In this case, the parameters are calculated from the different linear regions observed. The relationship between the slope (m) and the doping concentration ($N_{\mathrm{D(A)}}$) is given [27] as

$$N_{\mathrm{D(A)}} = \frac{2}{mqA^2\varepsilon_{\mathrm{s}}\varepsilon_0}. \tag{3.15}$$

The Schottky barrier height (ϕ_{B}) is given [23, 28] as

$$\phi_{\mathrm{B}} = V_{\mathrm{bi}} + \frac{kT}{q}\ln\left(\frac{N_{\mathrm{C}}}{N_{\mathrm{D(A)}}}\right) \tag{3.16}$$

and the depletion region width, W_{D} is given [24, 29] as

$$W_{\mathrm{D}} = \sqrt{\frac{2\varepsilon_{\mathrm{o}}\varepsilon_{\mathrm{s}}V_{\mathrm{d}}}{qN_{\mathrm{D(A)}}}}. \tag{3.17}$$

References

[1] S. Ebnesajjad, Surface and material characterization techniques, Handbook of Adhesives and Surface Preparation, *William Andrew Publishing,* **1** (2011) 31.

[2] R. D. Holbrook, A. A. Galyean, J. M. Gorham, A. Herzing, and J. Pettibone, *Front. of Nanosci.,* **8** (2015) 47.

[3] G. Cao, Nanostructures and nanomaterials: synthesis, properties and applications, *Imperial college press*, London, 2004.

[4] B. D. Cullity, *Readings*, **MA** (1978) 102.

[5] P. M. Chaikin, T. C. Lubensky, and T. A. Witten, Principles of condensed matter physics, *Cambridge university press,* Cambridge, 1995.

[6] J. A. Pineault, A. M. Belassel, and and M. E. Brauss, *Failure Analysis and Prevention* **11** (2002) 484.

[7] C. J. Chirayil, J. Abraham, R. K. Mishra, S. C. George, and S. Thomas, *Therm. and Rheolog. Meas. Techn. for Nanomaterials Character.,* **1** (2017) 1.

[8] P. S. Kumar, K. G. Pavithra, and M. Naushad, *Nanomaterials for solar cell appl.,* **1** (2019) 97.

[9] H. R. Verma, Atomic and nuclear analytical methods, *Springer,* Heidelberg, 2007.

[10] A. W. Chao and K. H. Mess, Eds, Handbook of accelerator physics and engineering, *World scientific publishing,* Singapore, 2013.

[11] V. S. Waman, M. M. Kamble, M. R. Pramod *et al., J. Non. Cryst. Solids*, **357** (2011) 3616.

[12] R. L. Merlino, *Am. J. Phys.*, **75** (2007) 1078.

[13] B. K. Jones, J. Santana, and M. McPherson, *Solid State Commun.*, **105** (1998) 547.

[14] M. K. Parida, S. T. Sundari, V. Sathiamoorthy, and S. Sivakumar, *Nucl. Instr. Meth. Phys. Res. Sect. A Accel. Spect., Detect. Assoc. Equip.*, **905** (2018) 129.

[15] D. K. Schroder, Semiconductor material and device characterization, *3rd ed., Wileys,* New Jersey, 2015.

[16] S. M. Sze and K. N. Kwok, Solar cells, *Phys. Semicond. Devices, 2nd ed.,Wileys,* New Jersey , 1981.

[17] S. Alialy, H. Tecimer, H. Uslu, and Ş. Altındal, *J Nanomed. Nanotechol.*, **4** (2013) 1000167.

[18] M. A. Mastro, Power MOSFETs and diodes, *Gallium Oxide,* **1** (2019) 401.

[19] S. J. Moloi and M. McPherson, *Phys. B Condens. Matter,* **404** (2009) 2251.

[20] I. K. Kovács and G. Horvai, *Sensors Actuators B. Chem.,* **19** (1994) 315.

[21] S. M. Sze, Semiconductor devices: physics and technology, *Wiley,* NewYork, 2008.

[22] G. Lutz, Semiconductor radiation detectors, *Springer,* Heidelberg, 2007.

[23] E. H. Rhoderick and E. H. Rhoderick, Metal-semiconductor contacts, *Clarendon Press*, Oxford, 1978.

[24] S. M. Sze, Physics of Semiconductor Devices, *Wiley*, New York, 1981.

[25] S. K. Cheung and N. W. Cheung, *Appl. Phys. Lett.*, **49** (1986) 85.

[26] D. K. Schroder, Semiconductor material and device characterization, *Wiley,* NewYork, 2015.

[27] M. Msimanga and M. McPherson, *Mater. Sci. Eng. B*, **127** (2006) 47.

[28] C. Morosanu, C. Cesile, S. Korepanov, P. Fiorini, C. Bacci *et al.*, *J. Non. Cryst. Solids*, **164** (1993) 8.

[29] I. S. Yahia, H. Y. Zahran, F. H. Alamri, M. A. Manthrammel, S. AlFaify, and A. M. Ali, *Phys. B Condens. Matter,* **543** (2018) 46.

Chapter 4

Experimental details

This chapter describes the procedure followed to prepare and characterise the samples. The samples are Si wafers that were doped with iron (Fe) and cadmium (Cd) and the diodes that were fabricated on the undoped and metal-doped Si. Doping was achieved by implantation of Si using an Ion Implanter based at iThemba LABS, Gauteng. The characterisation techniques used were Energy dispersive X-ray spectroscopy, X-ray diffraction, and Rutherford backscattering spectrometry for material characterisation. For device characterisation, current-voltage and capacitance-voltage techniques were used. Samples in this work also involve diodes that were irradiated by 4 MeV protons to a fluence of 10^{16} ion/cm^2.

4.1 Material acquisition and preparation

The materials used in this work are commercial *n*-, *p*- and *i*- type Si wafers polished on one side and were acquired from Semiconductor Wafer Inc. The details of the wafers are presented in Table 4.1.

Table 4.1: Details of the Silicon wafers used in this work.

	***n*-type Si**	***p*-type Si**	***i*-type Si**
Dopant	Phosphorus (P)	Boron (B)	-
Orientation	<111>	<111>	<100>
Diameter	50.8 mm	50.8 mm	50.8 mm
Thickness	275 ± 25 µm	275 ± 25 µm	275 ± 25 µm
Resistivity	1-20 Ω-cm	1-20 Ω-cm	>=500 Ω-cm

Using a diamond tip cutter, the wafers were diced into 0.9 cm x 0.9 cm square pieces. The usual cleaning technique employing methanol, acetone, trichloroethane, and de-ionized water was utilised to remove any handling grease and residue [1]. The oxide layer was removed by soaking the Si wafers in a 20 % hydrofluoric (HF) solution and blow-drying them using nitrogen gas before mounting them in a high-vacuum chamber for ion implantation.

4.2 Stopping and range of ions in matter

The stopping and range of ions in matter (SRIM) program is used to calculate the stopping power and range of ions in matter [2-3]. When energetic ions penetrate a material, they lose their energies through electronic energy loss (an inelastic collision with electrons) and nuclear energy loss (an elastic collision with atomic nuclei) [4-5]. Prior to ion implantation, the effects of the implantation of Fe and Cd ions in Si (target material) at 160 keV were simulated using SRIM/TRIM-2013 [6] to estimate the ion range, penetration depth, nuclear, and atomic interactions. The results of the theoretical prediction are presented in Figs. 4.1 and 4.2, for Fe and Cd, respectively.

The simulation was done using 99,999 ions and is presented in Fig. 4.1 (a), showing the surrounding collision cascades, the displaced ions, and the path created by Fe in Si. Fe ions travel through a random path in Si, losing energy due to electronic and nuclear collisions. Fig. 4.1 (b and c) shows the penetration depth and ion range of Fe in Si, which are estimated to be 300 nm and 134.5 nm, respectively. As shown in Fig. 4.1 (d), the electronic energy loss and nuclear energy loss for Fe were estimated to be 7.15 keV/nm and 8.38 keV/nm, respectively, indicating that the nuclear part is the dominant mechanism of the energy loss per unit length in the Si crystal.

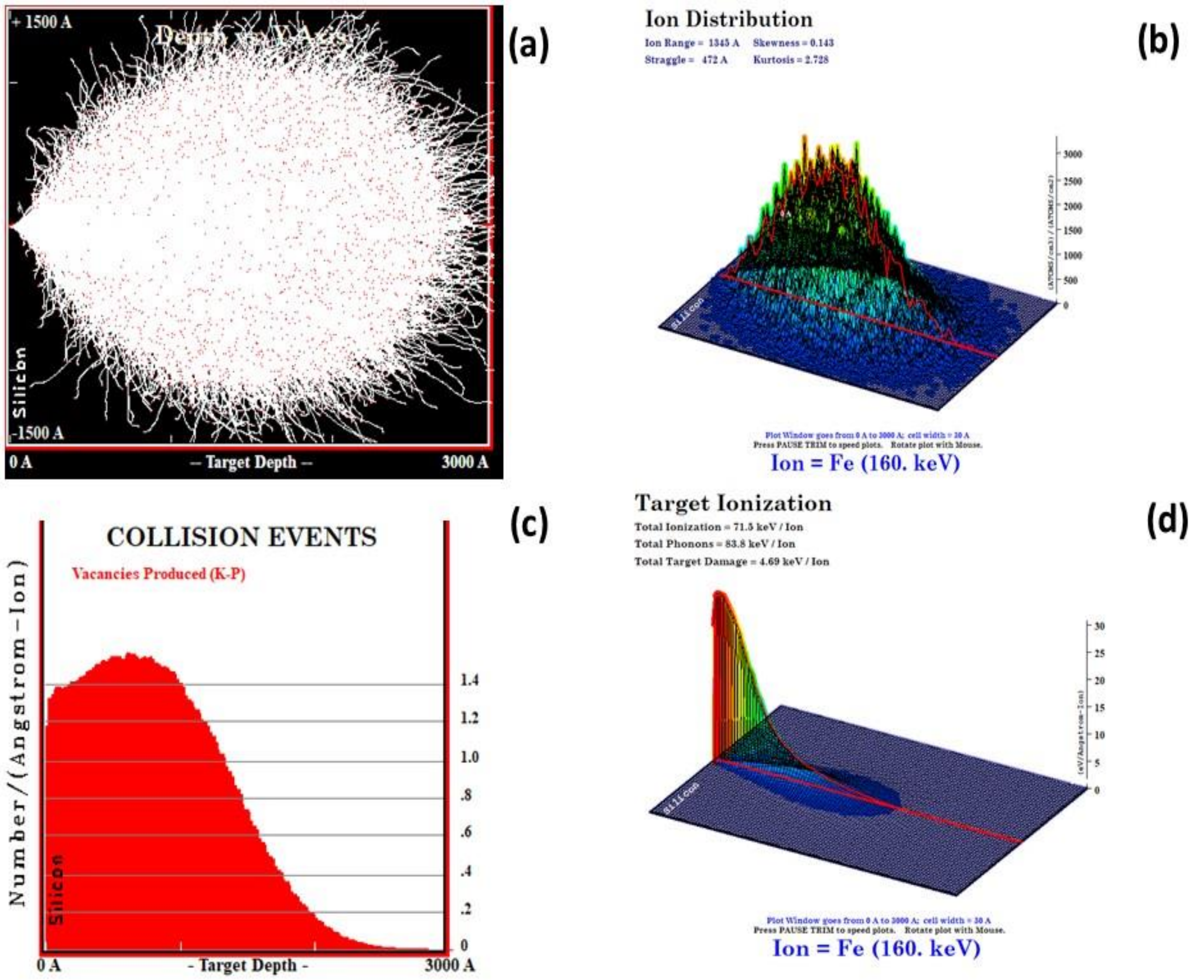

Fig. 4.1: *2-D TRIM and 3-D TRIM 2013 simulation showing, collision cascade within Si (a), ion range (b), collision events (c), and mode of energy loss (d) of Fe in Si at 160 keV.*

The results of the simulation for Cd in Si are presented in Fig 4.2. The collision cascades, displaced ions, and the path created by Cd ions are shown in Fig. 4.2 (a). As shown in Fig. 4.2 (b and c), the penetration depth and ion range of Cd in Si is about 170 nm and 83.3 nm, respectively. As shown in Fig 4.2 (d), the electronic energy loss and nuclear energy loss for Cd were estimated to be 5.94 keV/nm and 9.53 keV/nm, respectively, indicating that the nuclear part is the dominant mechanism of the energy loss per unit length in the Si crystal.

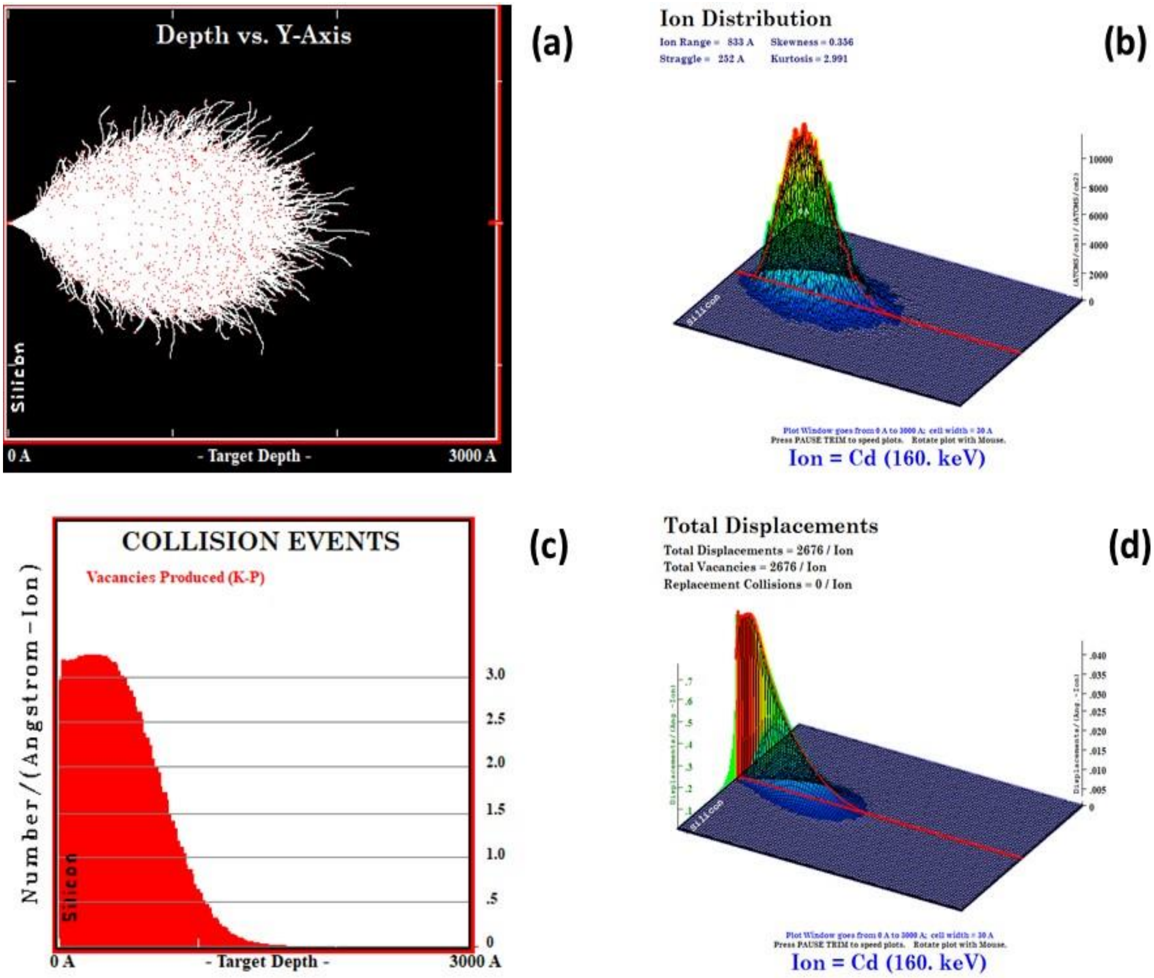

Fig. 4.2: *2-D TRIM and 3-D TRIM 2013 simulation showing, collision cascade within Si (a), ion range (b), collision events (c), and mode of energy loss (d) of Cd in Si at 160 keV.*

4.3 Ion implantation

After the simulation of the distribution of Fe and Cd in Si, the substrates were mounted in the chamber for Fe and Cd implantation. At an energy of 160 keV, Fe and Cd were implanted onto the polished side of the Si pieces using the Varian-Extrion model 200 – 20A2F ion implanter with an ES-30/25c processing station. Fluences 10^{15}, 10^{16}, and 10^{17} ion/cm^2 of Fe was implanted in *n*-Si. These fluences were chosen to achieve a reasonable degree of damage to the Si material. Different fluences were chosen for *n*-Si to establish and study a change in the electrical properties of the material-based diodes with Fe-doping concentration. Our system can achieve a maximum fluence of ~ 10^{17} ion/cm^2 for Fe-implantation. The highest fluence was chosen to cause the highest damage to the Si material [7].

The fluence of 10^{17} ion/cm^2 was chosen for *p* and *i*-Si to achieve the highest damage in the Si material. Fe was implanted in *p* and *i*-Si to the highest fluence only since the damage due to Fe implantation could be similar to that in the *n*-type. It has been reported that the damage by zinc (Zn) in *n*-Si was found to be similar to *p*-, and *i*-type Si [7].

Cd was implanted in *p* and *i*-Si with 160 keV to a fluence of 3.5×10^{15} ion/cm^2, the highest fluence that could be achieved by our facilities. The highest implantation energy (160 keV) was chosen to create the damage deep in the material. The ion implantation experiments were carried out at iThemba LABS, Gauteng.

Fig. 4.3 depicts the primary components and operating principles of the ion implanter. The ion source of the Varian-Extrion model 200 – 20A2F creates electrons thermionically by heating a tungsten filament with a high filament current. The generated electrons collide with the gas molecules, causing charge ionization and plasma formation within the ion source chamber. The electrostatic field set up between the source exit aperture and an extraction electrode extracts a beam of ions generated from a hot cathode arc discharge ion source. These ions are accelerated to an energy of 160 keV and admitted to a 90° dual focusing mass-analysing magnet in the high voltage terminal. The magnets are used to separate and choose the ions that will be implanted.

The separation is done based on the charge to mass ratio and only the desired ion species can pass through the resolving aperture diameter before proceeding to the acceleration tube. This process of selection and separation of the desired ion species is done by deflecting the beam into circular orbits. The amount of deflection depends on the charge to mass ratio of a particular ion. The lighter ions are deflected into orbits smaller than the heavier ions, and the deselected ions are gathered on the analyser chamber walls or on either side of the image plane's resolving aperture. The ion source, analyser magnets, and variable slit are contained in a high voltage terminal located inside a grounded enclosure, as shown in Fig 4.3, to ensure personal health safety.

The ion beam enters the linear acceleration tube after emerging from the resolving aperture to minimise the X-ray produced by back streaming of electrons and optimise beam focusing. The ion beam is accelerated in the acceleration beam with energy within the range of 25-160 keV provided by the field in the tube. The beam diverges as it passes through the acceleration region as a result of limited focus action, then the quadrupole lenses positioned at the entrance of the scanning box are used to focus the beam to 1 cm^2 in the target chamber. The scanning box contains a Y-scanner plate positioned vertically and an X-scanner plate positioned horizontally used to generate a uniform implant over a large area [9]. Finally, the sample is attached to the sample holder that is mounted on the target chamber and is kept at a pressure of about 5×10^{-6} Torr.

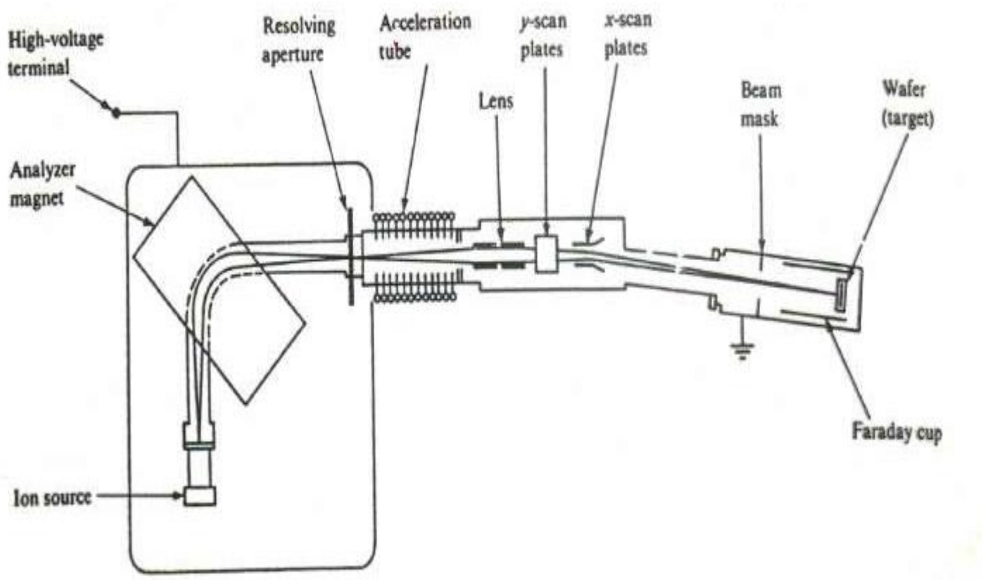

Fig. 4.3: *Schematic diagram for the Varian-Extrion 200 – 20A2F model ion implanter at iThemba LABS, Gauteng [8].*

4.4 Device fabrication

Prior to device fabrication, the Si substrates were cleaned again using the standard procedure described in Section 4.1. Immediately after the cleaning, the pieces were loaded into an evaporation chamber for making the contacts. In the case of *n*-type and *i*-type Si, Schottky contacts were achieved by evaporation and deposition of 100 nm gold (Au) through a mask of 0.6 mm diameter holes. Au was chosen because its work function (5.47 eV) is greater than that of Si (4.85 eV). The deposition was carried at 10^{-6} mbar at 1Å/s. The ohmic contact was realised by the evaporation and deposition of aluminium (Al) onto the back (unpolished) surface of the pieces. Al was chosen because its work function (4.06 eV) is lower than that of *n*-type Si.

Schottky contacts were achieved on *p*-type Si by the evaporation and deposition of 100 nm Al on the polished side through a mask of 0.6 mm diameter holes, and the ohmic contact was achieved by the evaporation and deposition of Au on the unpolished surface of the pieces. For Schottky contact, Al was chosen because its work function (4.06 eV) is lower than that of *p*-type Si (4.60 eV) while Au was chosen for ohmic contact because its work function (5.47 eV) is greater than that of *p*-type Si (4.60 eV). The finished devices each consist of 12 diodes on a piece with one common ohmic contact.

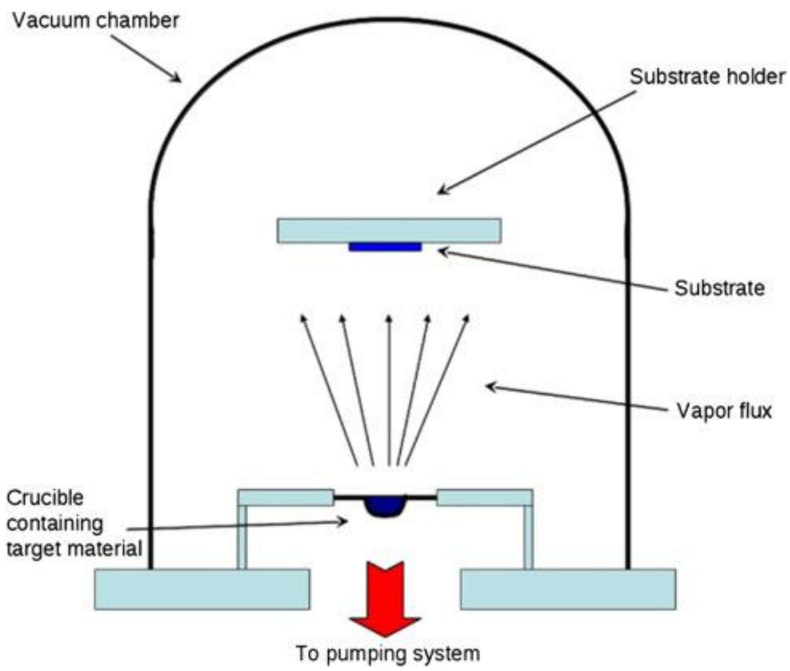

Fig. 4.4: *The thermal vacuum deposition system used to fabricate the diodes [10].*

The thermal vacuum deposition apparatus used to form the Schottky and ohmic contacts in this work is an Edwards AUTO 306 vacuum deposition shown in Fig 4.4. A typical sample showing a circular dot representing the Schottky contact on the top surface and a common ohmic contact on the back surface is shown in Fig. 4.5.

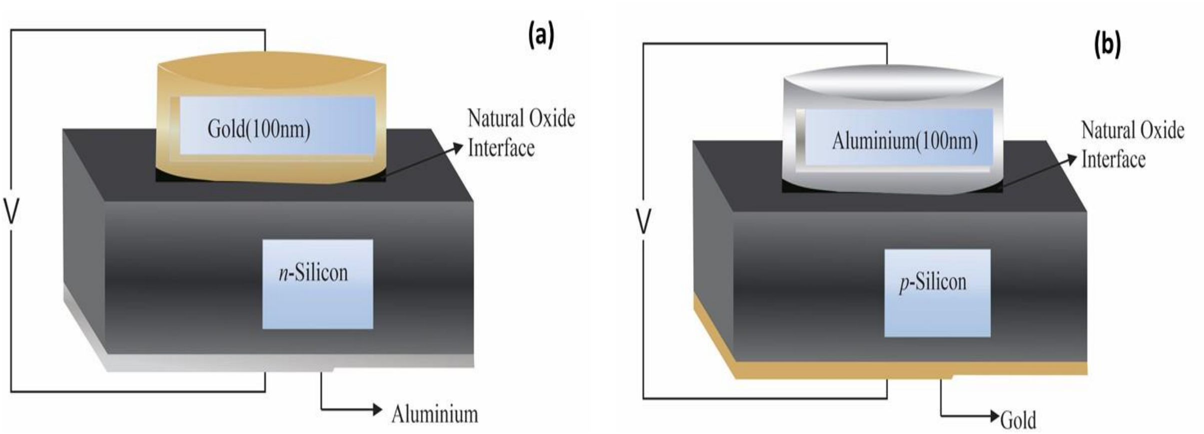

Fig. 4.5: *A typical sample showing circular Schottky contact on the top surface and ohmic contact on the back surface for n-Si (a) and p-Si (b) Schottky diodes.*

4.5 Device characterisation

In this work, *I-V* and *C-V* measurements were taken with the devices placed in the dark and at room temperature. Metres for current and capacitance measurements have been made in-house. The metres use the same hardware, and they focus on software to implement the functions. The probe station was connected to the metres read by the LabVIEW program specifically coded for these measurements. The contact between the device under test and the probe was determined accurately by enlarging the device under the microscope. During the measurements, the devices under test were placed in a test fixture to isolate the measurement system from outside electromagnetic fields and keep the probe station in a dark environment at room temperature.

The *I-V* measurements were taken over the range of -4 to 4 V. At voltages higher than ~ 0.7 V, the bias voltage has a lower contribution to the TE current [11]. At voltages above ± 1 V, the forward current saturates due to the effect of series resistance (R_s) [12], and the reverse current is less dependent on the applied voltage for the diodes fabricated on unimplanted Si material.

Throughout the experiments, the time between measurements was maintained at 1 s to allow the device to stabilise.

C-*V* measurements were taken over the range of 0 to -2 V at 5 kHz to study the junction properties of the fabricated devices. The acquired data was unstable at frequencies higher than 5 kHz and the measured capacitance was extremely low, close to the limit (pF) for our system. A measurement frequency of 5 kHz is the lowest that could be adopted for our diodes to minimise the effects of the *m*-*s* interface on the measured capacitance. Thus, charges at the interface cannot follow an a.c signal at the measurement frequencies of ≥5 kHz [12]. Based on our measurement setup, it was then safe to assume that the measured capacitance was mainly due to the SCR.

The diode parameters extracted from the *I*-*V* and *C*-*V* measurements are ideality factor, η, saturation currents, I_s, series resistance, R_s, shunt resistance, R_{sh}, doping density, N_D, built-in voltage, V_{bi}, Schottky barrier height, ϕ_B, and depletion region width W_D. These diode parameters are used to study the quality of the diode and a change in properties of the diode due to doping Si with metals.

4.6 Device irradiation

Schottky diodes fabricated on *p* and *n*-Si were irradiated with 4 MeV protons. The beam fluence was calculated prior to irradiation using the beam current (*I*), irradiated time (*t*), and beam spot area (*A*) on the target [13] as

$$\phi = \frac{Q}{qeA} = \frac{It}{qeA} \tag{4.1}$$

where Q is the charge quantity, *q* is the ionic charge, *e* is the electron charge (1.602×10^{-19} C), and *A* is the beam spot area, In order to achieve a fluence of 10^{16} ion/cm^2 with an average beam current of 2 nA for a beam spot area of 1.44 × 10^{-2} cm^2, an irradiation time of 4 hours is required.

The fabricated diodes were placed on a hexagonal carousal sample holder, then lowered into the microprobe chamber before exposure to proton irradiation using an ion implanter located at iThemba LABS in Gauteng, South Africa. In this study, the diodes were bombarded with 4 MeV protons for ~4 hours (to a fluence of 10^{16} ion/cm^2). This fluence was chosen for its ability to induce the most damage deep into the bulk. At the irradiation site, the ambient temperature was 300 K. The temperature of the samples may have increased throughout the irradiation procedure. For the duration of each irradiation, the beam current was monitored and recorded. This was important to keep the beam current constant so that the samples are of the same fluence. After irradiation, the diodes were characterised in the dark and at room temperature using *I-V* techniques.

References

[1] B. Bera, *Int. J. Appl. Nanotechnol.*, **5** (2019) 8.

[2] J. F. Ziegler, J. P. Biersack, and M. D. Ziegler, The stopping and range of ions in matter, *SRIM http//www. srim. org*, 2009.

[3] E. Friedland, S. Kalbitzer, M. Hayes, C. Klatt, G. Konac, and C. Langpape, *Nucl. Instr. Meth. Phys. Res. Sect. B Beam Interact. with Mater. Atoms,* **136** (1998) 147.

[4] B. Angadi, Y. S. Jung, W. K. Choi, R. Kumar, K. Jeong, *et al.*, *Appl. Phys. Lett.*, **88** (2006) 142502.

[5] S. Chattopadhyay, S. Dutta, D. Jana, D. Chattopadhyay, S. Sarkar *et al.*, *J. Appl. Phys.*, **107** (2010) 113516.

[6] J. F. Ziegler, M. D. Ziegler, and J. P. Biersack, *Nucl. Instr. Meth. Phys. Res. Sect. B Beam Interact. with Mater. Atoms*, **268** (2010) 1818.

[7] D. A. Oeba, Microcrystalline silicon devices for radiation sensing applications, *Ph.D Thesis, University of South Africa*, Johannesburg, 2021.

[8] T. E. Derry, E. K. Nshingabigwi, M. Levitt, J. Neethling, and S. R. Naidoo, *Nucl. Instr. Meth. Phys. Res. Sect. B Beam Interact. with Mater. Atoms*, **267** (2009) 2705.

[9] D. D. Cohen and E. K. Rose, *Nucl. Instr. Meth. Phys. Res. Sect. B Beam Interact. with Mater. Atoms,* **66** (1992) 158.

[10] A. Bashir, T.I. Awan, A. Tehseen, M. B. Tahir, and M. Ijaz, *Chem. of Nanomat.*, 1 (2000) 51.

[11] M. K. Parida, S. T. Sundari, V. Sathiamoorthy, and S. Sivakumar, *Nucl. Instr. Meth. Phys. Res. Sect. A Accel. Spect., Detect. Assoc. Equip.*, **905** (2018) 129.

[12] Ö. F. Yüksel, S. B. Ocak, and A. B. Selcuk, *Vacuum,* **82** (2008) 1183.

[13] J. O. Song, D. S. Leem, J. S. Kwak, O. H. Nam, Y. Park *et al.*, *Appl. Phys. Lett.,* **83** (2003) 4990.

Chapter 5

Material characterisation results

The material characterisation results for the samples used in this work are presented in this chapter. Materials are undoped and metal-doped Si. Metal doping was achieved by implantation of Fe and Cd with an energy of 160 keV to a fluence of 1.0×10^{17} and 3.5×10^{15} $\mathrm{ion/cm^2}$, respectively, the highest energy and fluence that could be achieved.

The material characterisations used in this work are energy-dispersive X-ray spectroscopy (*EDS*), X-ray diffraction (*XRD*), and Rutherford Backscattering Spectrometry (*RBS*) techniques. The techniques were used to study the elemental composition, structural, and depth analysis of the implanted metals in Si.

5.1 Energy Dispersive X-ray Spectroscopy (*EDS*)

In this work, *EDS* technique was used to investigate the elemental composition of the samples, hence the presence of the implanted metals in Si.

5.1.1 Undoped and Fe-doped Si

The *EDS* spectra of undoped and Si material doped by Fe to different fluences are presented in Fig. 5.1. The elemental composition of undoped Si presented in Fig. 5.1 (a) shows Si, oxygen (O) and carbon (C). The presence of O could be due to the low concentration of O involved in the Float zone method of producing Si [1]. The C observed in the spectra is due to the carbon tape used to stick the Si material on the sample holder.

The *EDS* spectra of Fe-doped *n*-Si to fluences 10^{15} and 10^{16} ion/cm^2 are presented in Figs. 5.1 (b) and (c). The absence of an Fe peak in the spectra suggests that the concentration of Fe at this fluence could be too low, hence, below the system's detection limit. However, Fe was detected in the spectrum of *n*-Si doped with Fe to a fluence of 10^{17} ion/cm^2 as shown in Fig. 5.1 (d), confirming that at the highest fluence (10^{17} ion/cm^2), the concentration of Fe is sufficient to be detected by the system. Although Fe was not detected with this method for the fluences of 10^{15} and 10^{16} ion/cm^2, the *XRD* technique confirmed (shown later) the presence of Fe in Si at all fluences. Thus, *EDS* techniques only confirm the presence of Fe in the Si material for the highest Fe fluence in Si.

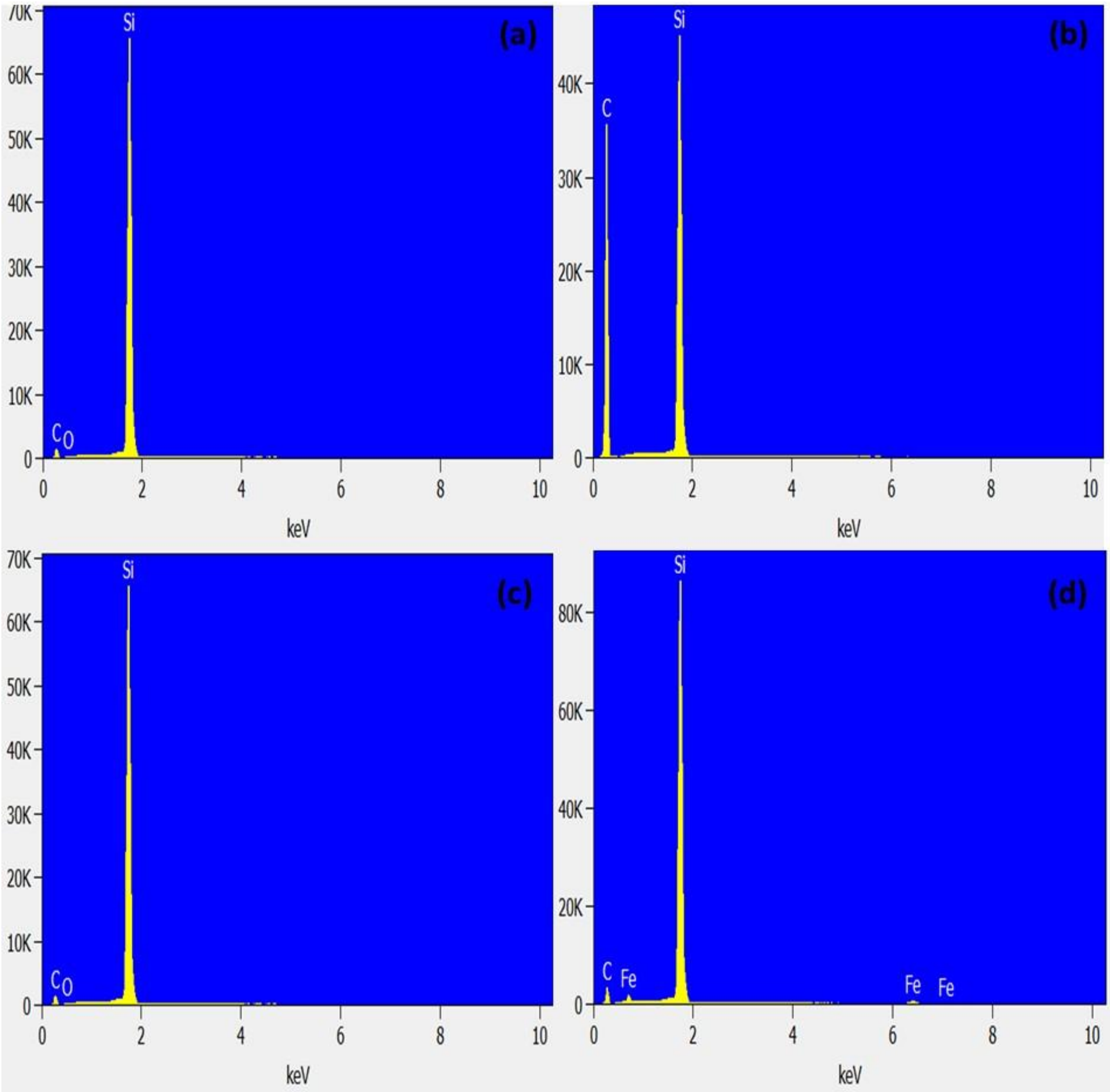

Fig. 5.1: *EDS spectra of undoped Si (a), Fe-doped Si material to the fluence of 10^{15} (b), 10^{16} (c), and 10^{17} (d) ion/cm^2.*

5.1.2 Undoped and Cd-doped Si

The *EDS* spectra of undoped and Cd-doped Si material are presented in Fig. 5.2. The elemental composition of the sample includes Si, Cd, C, and O. The peak of Cd is low, and this could be due to the low fluence (3.5×10^{15} ion/cm^2) of Cd ions implanted in Si. However, Cd was detected at low fluence, unlike Fe because the atomic mass of Cd is greater than that of Fe thereby limiting the depth of Cd in Si. This is shown in the SRIM/TRIM simulation as Fe ions penetrate deeper into the Si material than Cd ions. Hence, Cd ions are close to the surface of the material and will be easily detected since *EDS* is good for surface and near-surface analysis [2].

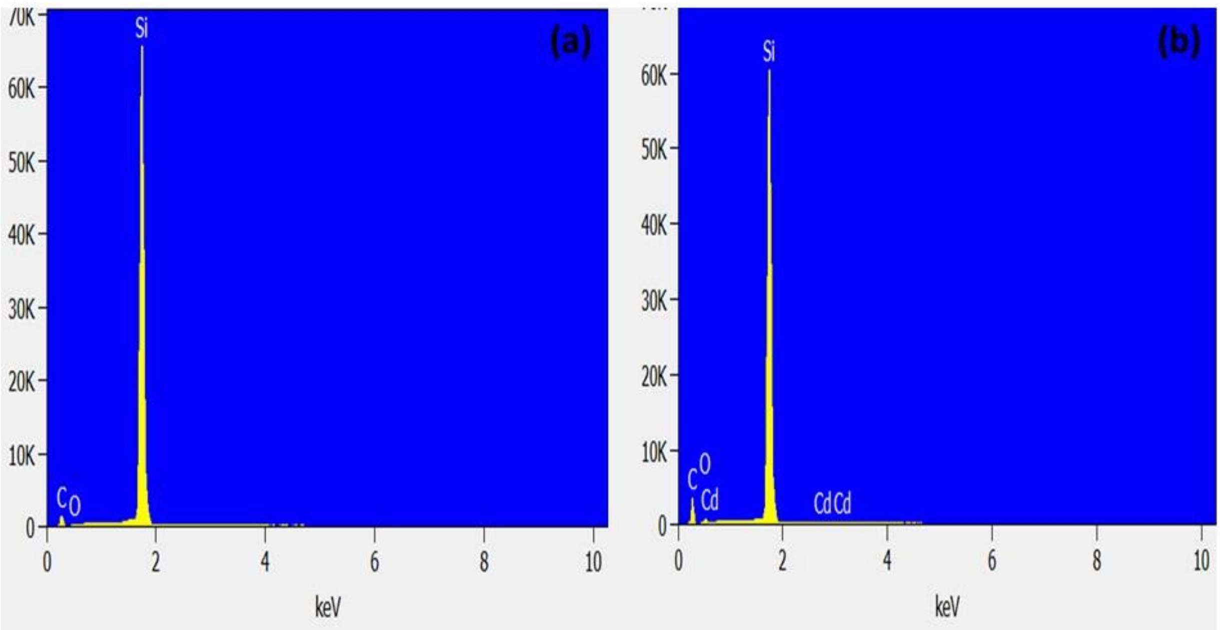

Fig. 5.2: *EDS spectra of undoped Si (a) and Cd-doped (b) Si material.*

5.2 X-ray diffraction (*XRD*)

The structural properties of the samples are investigated with *XRD* techniques. The measurements were taken at 2θ angles ranging from 5° to 90°. The obtained phases were identified and analysed using PANalytic (V 3.0e) X'pert Highscore software [3-4].

5.2.1 Undoped and Fe-doped Si.

The *XRD* patterns observed on the undoped and Fe-doped Si material are presented in Fig. 5.3 and the prominent peaks are for Si and SiO_2. The small peaks observed at angles of 26°, 28°, 60° are attributed to SiO_2 and at 85° is attributed to O_2. The presence of SiO_2 and O_2 shows that the oxide layer has been formed on the surface of the Si. The *XRD* patterns observed on undoped and Si doped by Fe to different fluences of 10^{15},10^{16}, and 10^{17} ion/cm^2 are also presented in Fig. 5.3.

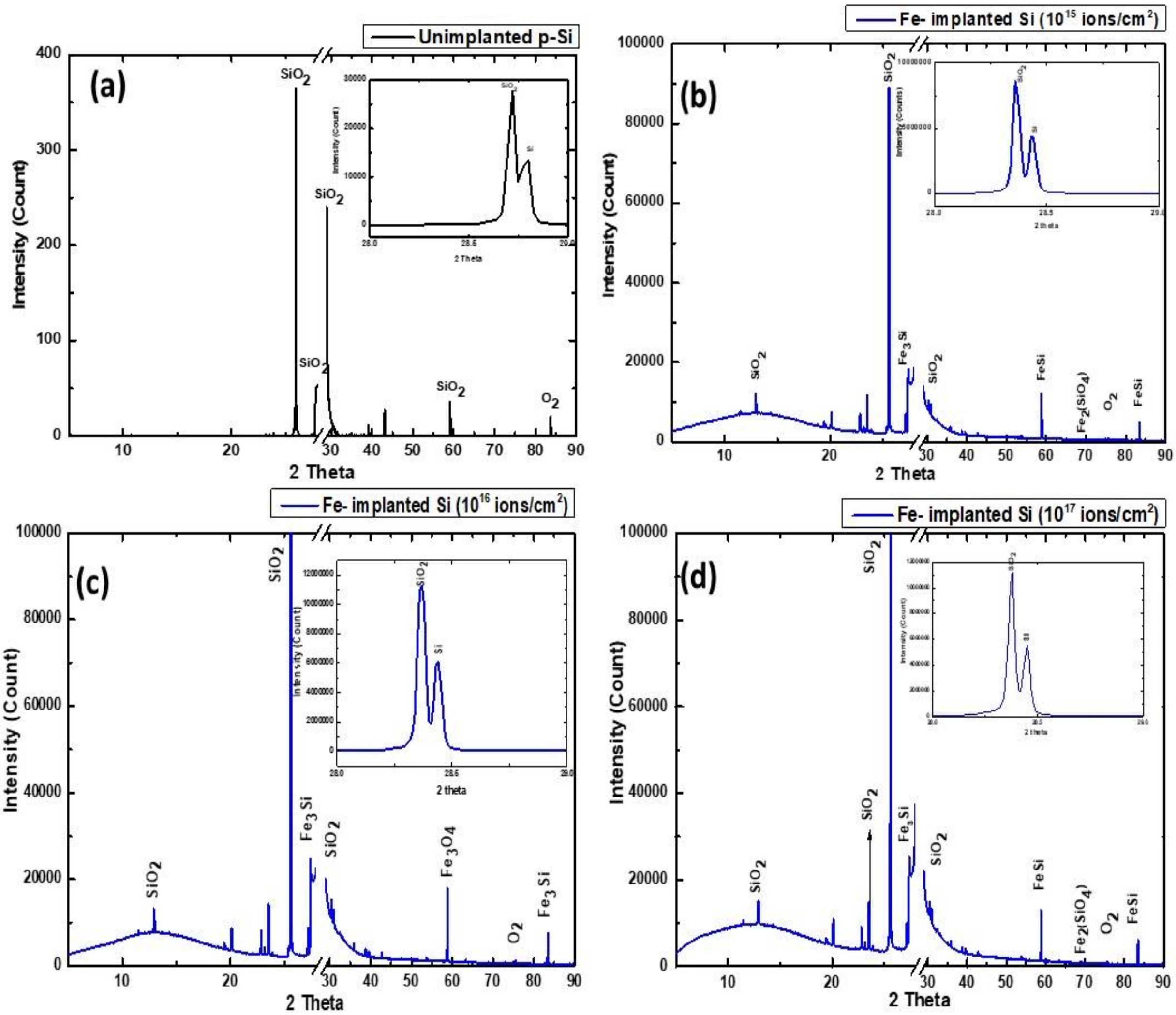

Fig. 5.3: *XRD pattern of undoped (a), Fe-doped Si material to the fluence of 10^{15} (b), 10^{16} (c), and 10^{17} (d) ion/cm^2.*

The observed *XRD* patterns for all the fluences looked similar with Si and SiO_2 having the prominent peaks. The smaller peaks observed are Fe_3Si, FeSi, $Fe_3(SiO_4)$, Fe_3O_4, and SiO_2, indicating that Fe has been incorporated with Si and O into the crystal of Si. A broad peak is also observed at low 2 theta (1° to 20°) on the Fe-doped Si. This broad peak is associated with SiO_2, further confirming that the surface of Si was oxidised. Despite the presence of the oxide layer, the crystal quality of the material remained intact as the observed Si peak remained sharp even after Fe-doping. Table 5.1 displays the crystallographic data of the phases. The *XRD* results have shown the structural properties of the undoped and Fe-doped Si materials and they show that the samples still maintain the crystalline structure even after Fe-doping.

Table 5.1: Crystallographic data of phases present in the undoped and Fe-doped Si material.

Phase	Space group	a (Å)	b (Å)	c (Å)	Cell vol. (10^6 p.m^3.)	Ref. no.
Si (Cubic)	Fd-3m (227)	5.43	5.43	5.43	160.11	00-005-0565 [5]
SiO_2 (Hexagonal)	P3121	4.58	4.58	5.19	94.39	01-070-3315 [6]
SiO_2 (Tetragonal)	P42/mnm (136)	4.15	4.15	2.66	45.74	01-080-0374 [7]
SiO_2 (Monoclinic)	C2/m (12)	9.50	30.71	7.31	2132.64	01-089-7499 [8]
$Fe_2(SiO_4)$ (Monoclinic)	Fd-3m (225)	8.24	8.24	8.24	559.74	01-080-1625 [9]
Fe_3Si (Cubic)	Fm-3m (277)	5.67	5.67	5.67	182.28	03-065-0146 [10]
$Fe_{2.25}Si_{0.75}O_4$) (Cubic)	Fm-3m (277)	8.29	8.29	8.29	568.90	01-089-6229 [11]
Fe_3O_4 (Orthorhombic)	Pmc21 (26)	11.87	11.85	16.75	2356.13	01-076-0957 [12]
O_2 (Rhombohedral)	R-3m (166)	2.85	2.85	10.22	71.76	01-085-0424 [13]

5.2.2 Undoped and Cd-doped Si material.

The *XRD* patterns observed on the undoped and Cd-doped Si are presented in Fig. 5.4 and the prominent peaks are Si and SiO_2. The smaller peaks observed are $CdSiO_2$ and SiO_2. A broad peak is also observed at low 2 theta (1° to 20°) on the Cd-doped Si material. This broad peak is associated with SiO_2, further confirming that the surface of Si was oxidised. Despite the presence of the oxide layer, the crystal quality of the material remained intact as the observed Si peak remained sharp even after Cd-doping.

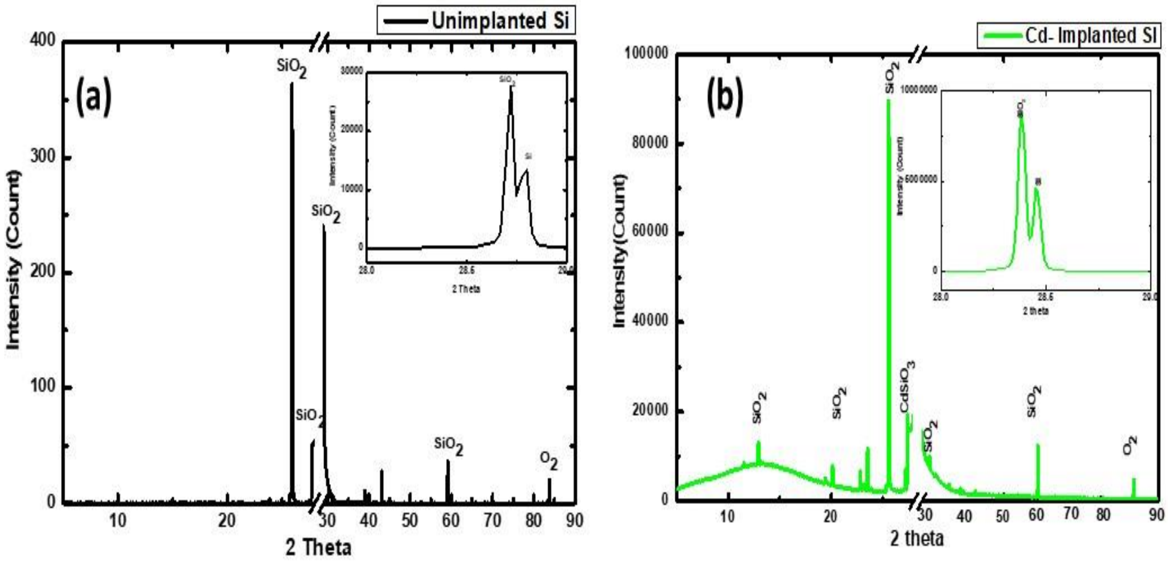

Fig. 5.4: *XRD pattern of undoped (a) and Cd-doped (b) Si material.*

The crystallographic data of the phases detected is given in Table 5.2. The presence of Cd is confirmed in Fig. 5.4 and Table 5.2 as a phase is identified to match with $CdSiO_2$, a compound having Cd as one of its elements. The *XRD* data has shown the structural properties of the undoped and Cd-doped Si materials. The samples still maintain their crystalline structure even after Cd-doping. Also, the presence of Cd is confirmed by these results.

Table 5.2: Crystallographic data of phases present in the Cd-implanted Si material.

Phase	Space group	a (Å)	b (Å)	c (Å)	Cell vol. (10^6 p.m^3.)	Ref. no.
Si (Cubic)	Fd-3m (227)	5.43	5.43	5.43	160.11	00-005-0565 [5]
SiO_2 (Hexagonal)	P3121	4.58	4.58	5.19	94.39	01-070-3315 [6]
O_2 (Rhombohedral)	R-3m (166)	2.85	2.85	10.22	71.76	01-085-0424 [13]
$CdSiO_2$ (Monoclinic)	P21/a (14)	15.10	3.63	6.945	379.65	00-035-0810 [14]

5.3 Rutherford backscattering spectrometry (*RBS*)

RBS technique was employed to determine the depth and thickness of the doped metals (Fe and Cd) in Si. The SIMNRA simulation software was used to compare the experimental and simulated results to determine the penetration depth and thickness of the implanted metals in Si [15]. A standard sample made of carbon as a substrate with nickel (Ni), Au, Al, and O as its constituents was used to perform calibration. For the standard sample, the energy of the scattered ions was calculated using known kinematic factors from SIMNRA [15].

Fig. 5.5 shows an experimental *RBS* spectrum for the Fe-doped Si. The experimental spectrum (red) is identical to the simulated spectrum (blue) in the figure for the Si peak. The peak of Si is well pronounced and broad, while the Fe peak is smaller. From fitting the experimental *RBS* spectrum, the thickness of Fe in Si was found to be $350 \times 10^{15} \mathrm{atoms/cm^2}$, which is ~ 70.32 nm. The thickness units were converted to nm by dividing the thickness by the target density of Si, which is given as $4.977 \times 10^{15}\ \mathrm{atoms/cm^3}$. As seen in the inset of Fig. 5.5, a small shift was observed in the simulated and experimental Fe peaks. Since the experimental result shifts towards low energy, it is assumed that the energies of the backscattered alpha particles are due to Fe on the surface. Therefore, as the incident ion beam penetrates Si, it loses some of its energy before colliding with Fe that is located some depth below the surface of Si. This shift, therefore, shows that Fe was implanted at some depth from the surface of the Si. The difference in characteristic energies was used to determine this depth [16].

The penetration depth was obtained through the evaluation of the stopping power, $S(E)$ and the differences in surface backscattering energy (E_{Surfaces}) and characteristic energy ($E_{\mathrm{Characteristic}}$). The penetration depth is given [17] as

$$\int_{E(\mathrm{Characteristic})}^{E(\mathrm{Surfaces})} dx = \Delta x = \int_{E(\mathrm{Characteristic})}^{E(\mathrm{Surfaces})} \frac{1}{S(E)}\, dE \tag{5.1}$$

which gives,

$$\Delta x = \frac{E_{\mathrm{Surfaces}} - E_{\mathrm{Characteristic}}}{S(E)} \tag{5.2}$$

The evaluated penetration depth of Fe in Si is 116.59 nm. The penetration depth (116.59 nm) obtained from *RBS* differs from 300 nm estimated using SRIM/TRIM simulation. The difference could be because in SRIM/TRIM calculations the crystal structure and direction are not considered [18]. The influence of neighbouring atoms and recombination of interstitial atoms with the vacancies are also not considered in the calculations [18]. During the SRIM/TRIM calculation, the dynamic composition changes of the material are not considered [19].

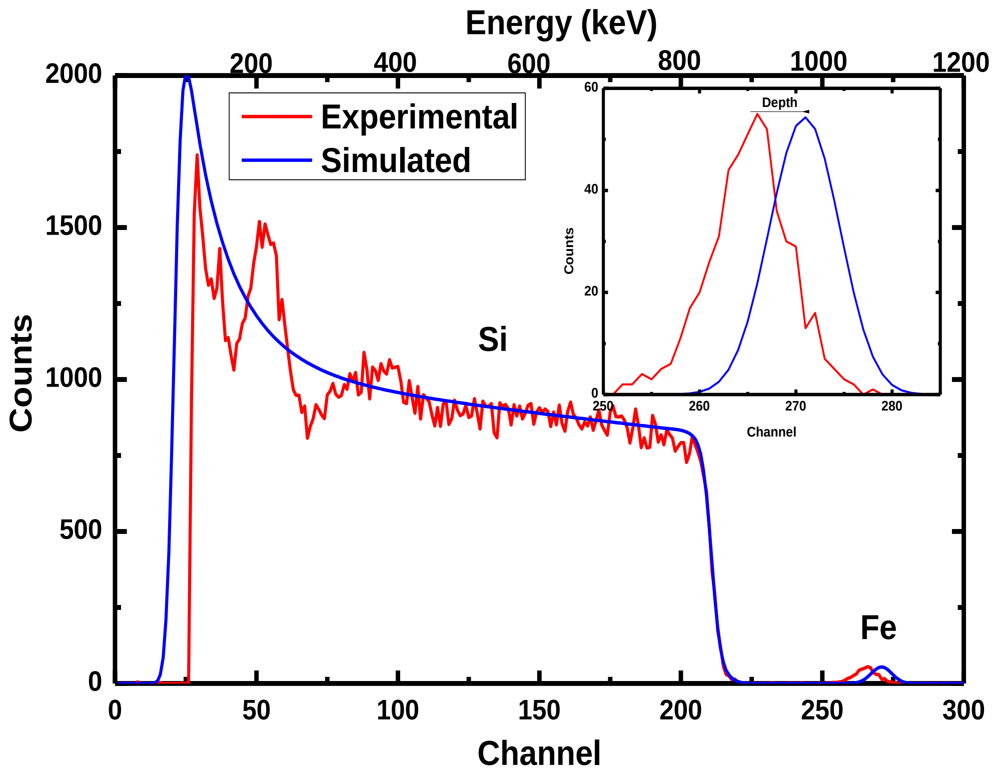

Fig. 5.5: *RBS full spectrum of Fe-doped Si sample. Inset: Expanded view of the Fe characteristic RBS peak.*

Figure 5.6 shows the experimental *RBS* simulated spectra for a Cd-doped Si. As observed in the figure, the experimental spectrum (red) is successfully fitted on the simulated spectrum (blue). From fitting the experimental *RBS* spectrum, the thickness of Cd in Si was found to be $515 \times 10^{15} \text{atoms/cm}^2$, which is ~ 103.48 nm.

In evaluating the penetration depth for the Cd-implanted Si, (Fig. 5.6), it was observed that the simulated and experimental peaks for Cd-implanted Si were the same, thereby making it difficult to analyse the penetration depth of Cd in Si.

The results from material characterisation confirmed the presence of Fe and Cd in the doped Si samples.

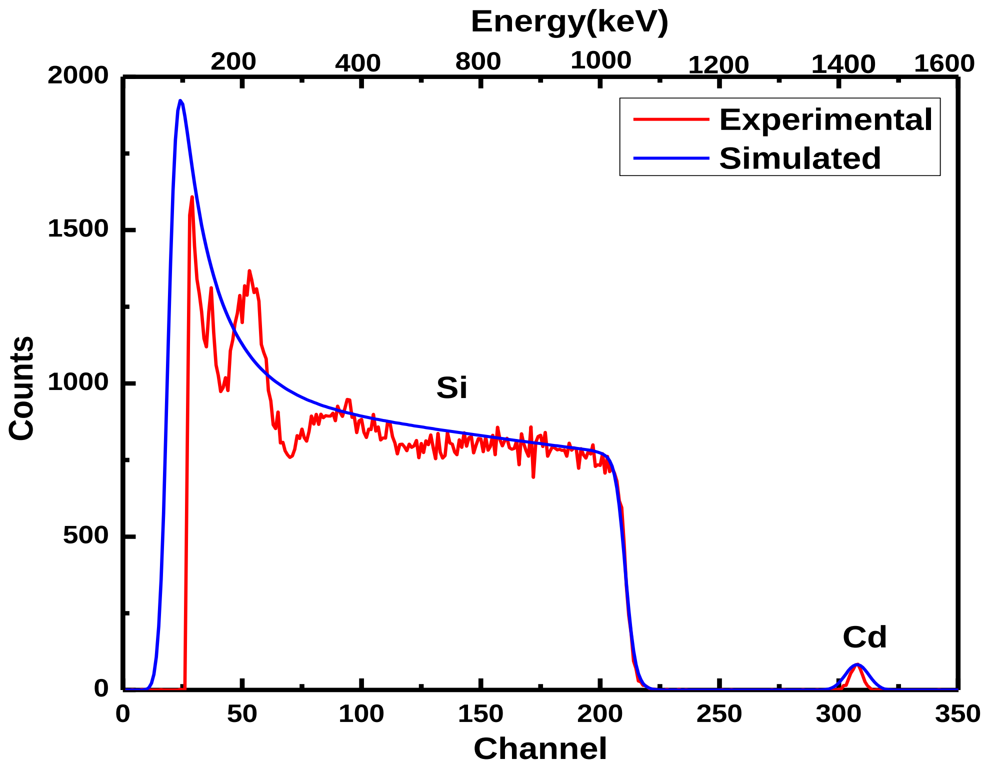

Fig. 5.6: *RBS full spectrum of Cd-doped Si sample.*

References

[1] H. J. Rost, R. Menzel, A. Luedge, and H. Riemann, 2012. *J. of crystal growth*, **360** (2012) 43.

[2] S. Yesilkir-Baydar, O. N. Oztel, R. Cakir-Koc, and A. Candayan, *Nanobiomat. Sci., Develop.and Evaluation*, **1** *(*2017) 211.

[3] L. dos Santos-Gómez, J. M. Porras-Vázquez, E. R. Losilla, and D. Marrero-López, *RSC Adv.*, **5** (2015) 107889.

[4] W. S. Yum, Y. Jeong, S. Yoon, D. Jeon, Y. Jun, and J. E. Oh, *Cem. Concr. Compos.*, **84** (2017) 111.

[5] R. Jenkins, T. G. Fawcett, D. K. Smith, J. W. Visser, M. C. Morris, and L. K. Frevel, *Powder Diffr.*, **1** (1986) 51.

[6] J. Kim-Zajonz, S. Werner, and H. Schulz, *Zeitschrift für Krist. Mater.*, **214** (1999) 324.

[7] M. Sugiyama, S. Endo, and K. Koto, *Mineral. J.*, **13** (1987) 455.

[8] P. A. Barrett, M. J. Díaz-Cabañas, and M. A. Camblor, *Chem. Mater.*, **11** (1999) 2919.

[9] J. Ding, D. Li, and P. Fu, *Powder Diffr.*, **5** (1990) 221.

[10] K. Sugiyama, N. Kaji, and K. Hiraga, *J. Alloys Compd.*, **368** (2004) 251.

[11] T. Yamanaka, H. Tobe, T. Shimazu, A. Nakatsuka, Y. Dobuchi, *et al.*, *Washingt. DC Am. Geophys. Union Geophys. Monogr. Ser.*, **101** (1998) 451.

[12] M. Iizumi, T. F. Koetzle, G. Shirane, S. Chikazumi, M. Matsui, and S. Todo, *Acta Crystallogr. Sect. B Struct. Crystallogr. Cryst. Chem.*, **38** (1982) 2121.

[13] D. Schiferl, D. T. Cromer, and R. L. Mills, *Acta Crystallogr. Sect. B Struct. Crystallogr. Cryst. Chem.*, **37** (1981) 1329.

[14] L. S. D. Glasser and F. P. Glasser, *Inorg. Chem.*, **3** (1964) 1228.

[15] M. Mayer, *SIMNRA user's guide*. *Max-Planck-Institut für Plasmaphysik Garching, Germany.* 1997.

[16] S. Khamlich, M. Msimanga, C. A. Pineda-Vargas, Z. Y. Nuru, R. McCrindle, and M. Maaza, *Mater. Charact.*, **70** (2012) 42.

[17] K. Wittmaack, *J. Appl. Phys.*, **96** (2004) 2632.

[18] J. F. Ziegler and J. P. Biersack, The stopping and range of ions in matter, *Treatise on heavy-ion science*, *Springer*, 1985.

[19] K. Nordlund, *J. Nucl. Mater.*, **520** (2019) 273.

Chapter 6

Device characterisation results

The findings of current-voltage (*I-V*) and capacitance-voltage (*C-V*) measurements on the fabricated devices are presented in this chapter. The devices are Schottky diodes fabricated on undoped and metal-doped Si. The measurements were taken to determine the quality of the fabricated diodes as well as to extract diode parameters. Changes in *I-V* and *C-V* trends as well as changes in diode parameters due to metal doping are presented in this chapter.

6.1 Current-voltage results

I-V characteristics were carried out on four diodes fabricated on each material (undoped and doped Si). The acquired data was presented on different scales to study the quality and conduction mechanisms of the fabricated diodes. Diode parameters such as the ideality factor (η), the saturation current (I_s), the Schottky barrier height (ϕ_B), the parasitic resistance, and the rectification ratio were also extracted from the data.

The diodes fabricated on the same material showed a similar trend, indicating that they were the same diodes fabricated on the same material. However, in some circumstances (See appendix A), the measured currents and evaluated parameters differ slightly, possibly due to the inhomogeneous metal deposition during Schottky contact formation or non-uniform distribution of dopants during the implantation process.

6.1.1 Fe-doped Si diodes

6.1.1.1 *n*-Silicon diodes

Fig. 6.1 shows the *I-V* characteristics of diodes fabricated on undoped and *n*-Si doped by Fe diodes in a linear scale. In this scale, the quality of the fabricated diodes is investigated. The reverse current of the undoped *n*-Si diode is independent of voltage as shown in Fig. 6.1 (a), since the reverse current is due to minority carriers (holes) in *n*-Si. In forward bias, the current remains independent of voltage until ~ 0.3 V because the electrons have not gained enough energy to surmount the junction barrier. At ~ 0.31 V, the current starts to increase rapidly, indicating that the junction barrier has been surmounted as charge carriers diffuse through the SCR. Thus, the high charge carrier density is withdrawn to the opposite electrodes to contribute to the measured current. The trend observed in Fig 6.1 (a) is a typical *I-V* behaviour of a semiconductor diode [1-3], indicating that the diodes were well fabricated using Au for Schottky contact. This is expected since the work function of Au (5.47 eV) is greater than that of *n*-Si (4.85 eV). For the fabrication of Schottky diodes on *n*-Si, the metal work function should be higher than that of Si [4].

The reverse current of the diode fabricated on *n*-Si doped by Fe to a fluence of 10^{15} ion/cm^2 presented in Fig 6.1 (b) remains independent of voltage in this scale. In forward bias, the current remains independent of voltage till ~ 0.7 V, then increases gently with voltage. Unlike in the case of the undoped *n*-Si diode, the energy needed to overcome the junction barrier has increased and the forward current has reduced suggesting that Fe-induced defects generated at this fluence recombine with majority carriers to increase the resistivity of the material.

Fig. 6.1 (c) presents the *I-V* characteristics of the diode fabricated on *n*-Si doped by Fe to a fluence of 10^{16} ion/cm^2. At low voltages (0-0.64 V), the reverse current is independent of the applied voltage. At a reverse voltage greater than ~ 0.65 V, the current increases rapidly with voltage. Unlike in the case of the undoped *n*-Si diode in Fig. 6.1 (a), the reverse current for this diode has increased at high voltages, indicating that minority carriers have been generated after doping with Fe to the fluence of 10^{16} ion/cm^2. The forward current is independent of voltage till ~ 0.46 V, then starts increasing rapidly with voltage. In comparison with the undoped *n*-Si diode, the forward current has decreased significantly, showing that majority carriers have recombined with the produced minority carriers to decrease the density of the charge carriers through SCR. This decrease in carrier density indicates an increase in the resistivity of the material following Fe-doping to the fluence of 10^{16} ion/cm^2.

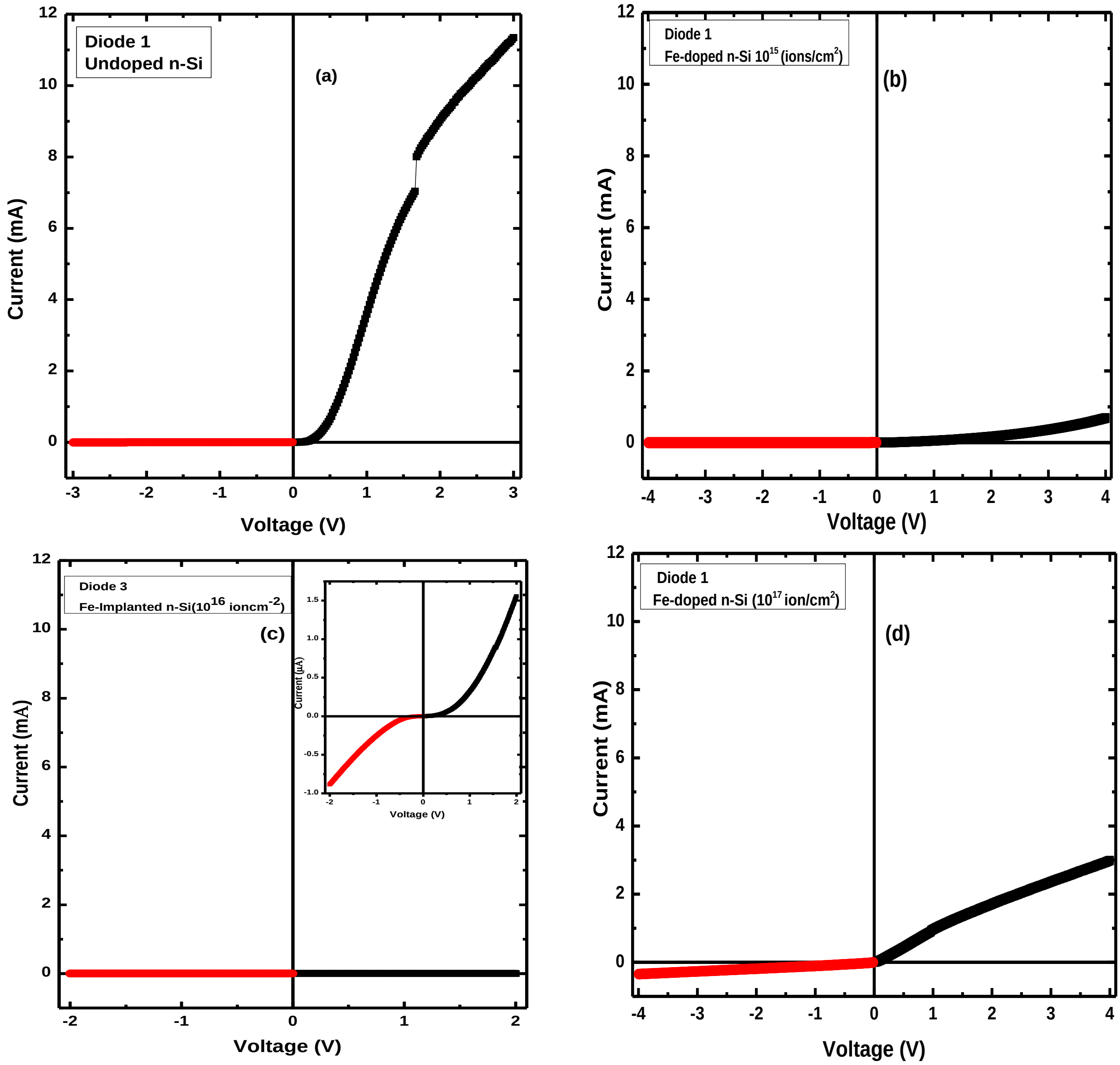

Fig. 6.1: *I-V characteristics of the diodes fabricated on undoped and Fe-doped n-Si in a linear-linear scale. Inset of Fig. 6.1(c) shows the rescaled I-V characteristics of Fe-doped n-Si to the fluence of* 10^{16} *ion/cm*^{2}.

As seen in Fig 6.1 (d), the diode fabricated on *n*-Si doped by Fe to a fluence of 10^{17} ion/cm^2 shows the reverse current varying linearly with voltage for the whole voltage range in the linear-linear scale. The forward current increases linearly with voltage and it has decreased, implying that Fe-induced defects at this fluence are responsible for recombination of the majority carriers, resulting in an increase in the resistivity of Si.

The ln(*I*)-*V* characteristics of the diodes fabricated on undoped and *n*-Si doped by Fe to different fluences are presented in Fig. 6.2 to further investigate a change in *I*-*V* characteristics of the diodes with the doped Fe fluences. The analysis is presented in this scale to determine the diode quality, the region to evaluate the parameters and the region where the effect of R_s is present. The variation of leakage current and the breakdown voltage is evaluated on the reverse bias characteristics [3]. However, in the forward bias, the linear region is used to evaluate the diode parameters such as η, I_s, and ϕ_B [5]. The parameters are evaluated in the region where the effects of R_s is negligible.

At low voltages (0-0.1 V), the reverse current of undoped *n*-Si increased linearly with voltage. The increase in reverse current results from minority carriers resulting from thermal generation of the minority carriers. At voltages above $-$ 0.1 V, the reverse current increased slightly with voltage, then starts to saturate. The gradual increase of reverse current results from the low injection rate of minority carriers (holes) in *n*-Si. In the forward bias, the current exhibits a linear trend in the low voltage region (0-0.4 V). However, the linear trend flattens at voltages higher than 0.4 V as a result of the effect of R_s at high voltages [6].

The diode fabricated on *n*-Si doped with Fe to the fluence of 10^{15} ion/cm^2 shows that the reverse current is almost the same as the reverse current of the undoped *n*-Si diode, indicating that the effect of Fe-doping to the fluence of 10^{15} ion/cm^2 on the reverse current is negligible. On the other hand, the forward current has reduced by a factor of 47 at 2 V, indicating that the majority carrier (electrons) recombination rate is high, leading to a low charge carrier density through the SCR after doping at this fluence, 10^{15} ion/cm^2.

The reverse and forward current for Fe-doped *n*-Si diodes to the fluence of 10^{16} ion/cm^2 is lower than that of undoped diode by a factor of 2.5 and 10^4, respectively, at 2 V. The decrease in the reverse and forward current implies recombination of both minority and majority carriers as a result of the defects induced by Fe implanted at this fluence, 10^{16} ion/cm^2.

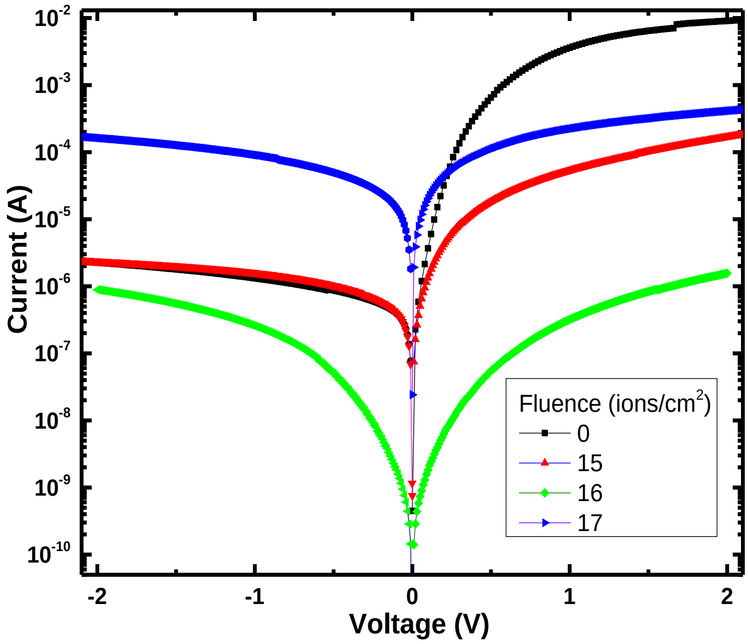

Fig. 6.2: *Forward and reverse bias ln(I)-V characteristics of diodes fabricated on undoped and Fe-doped n-Si.*

The reverse current of the diode fabricated on *n*-Si doped by Fe to the fluence of 10^{17} ion/cm^2 is higher than that of the undoped *n*-Si by a factor of 10^2 while the forward current is reduced by a factor of 21 at 2 V. An increase in leakage current at higher voltage indicates that Fe-doping at this fluence is responsible for generating minority carriers in *n*-Si. It is possible that the generated minority carriers recombined with the majority carriers, decreasing the density of free charge carriers, hence the observed decrease in forward current. The forward current trends of the doped diodes are lower than that of the undoped diode, indicating that the resistivity increases after Fe doping.

Diode parameters such as η, I_s, and ϕ_B were evaluated from the linear ln*(I)-V* regions in Fig 6.2 for all diodes. The values of R_s were calculated using Cheung's method [7] as described in

Chapter 3, equations (3.11) and (3.13). As shown in Fig. 6.3, the plots of dV/dln(I) and *H(I)-I* are linear for the whole voltage ranges. Diode parameters are extracted from the linear region of the plots. The parameters evaluated from Figs. 6.2 and 6.3 are presented in Table 6.1 and are the average of the values obtained from the four diodes fabricated on each material (See Appendix A).

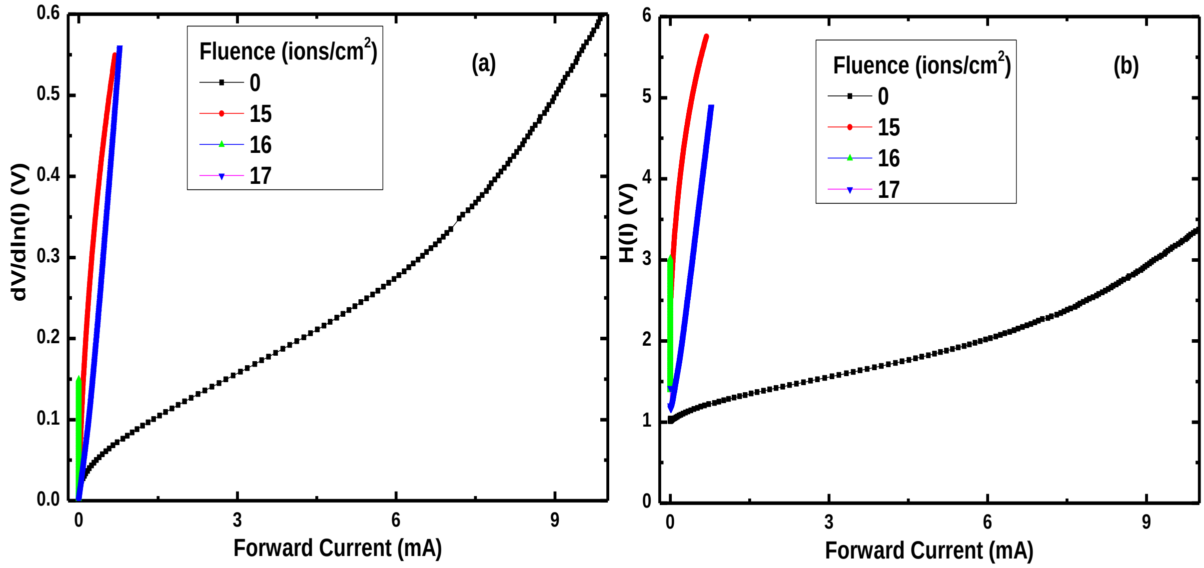

Fig. 6.3: *dV/dln(I)-I(a) and H(I)-I (b) characteristics of the diodes fabricated on undoped and Fe-doped n-Si.*

The parasitic resistance is defined in terms of the shunt resistance (R_{sh}) and R_s and obtained from the plot of junction resistance $\left(R_j = \frac{\partial V}{\partial I}\right)$ against voltage. The maximum value of R_j at a sufficiently high reverse voltage corresponds to R_{sh} while the minimum value of R_j in forward bias corresponds to R_s [8–10]. The R_j-V plots for the diodes fabricated on undoped and Fe-doped *n*-Si are presented in Fig. 6.4. R_j of the undoped *n*-Si diode is independent of reverse voltage, indicating that SCR extends into the bulk and material resistivity is constant. The saturation of R_j is expected since the bulk of the material is relatively defect-free. The R_j of undoped *n*-Si based diode decreases as forward voltage increases due to the high density of free charge carriers through the SCR.

In reverse bias, R_j trend of the diode fabricated on *n*-Si doped by Fe to a fluence of 10^{15} ion/cm^2 is similar to that of the undoped *n*-Si diode, indicating that the defects induced by Fe doped at this fluence do not affect the minority carriers. This could be because the defect induced at this fluence is insufficient to affect the minority carriers. In forward bias, however, the R_j trend of 10^{15} ion/cm^2 is higher than that of the undoped *n*-Si diode, indicating that the defect induced at this fluence recombines with majority carriers, hence reducing the density of charge carrier density through SCR.

The R_j trend for the diode fabricated on *n*-Si doped by Fe to a fluence of 10^{16} ion/cm^2 decreases with reverse voltage, indicating that a low charge injection rate through SCR after Fe-doping at this fluence. An absence of saturation of R_j-V plot for Fe-doping at this fluence in reverse bias shows that the density of defects associated with Fe-doping at this fluence decreases with the penetration depth of Fe in the bulk of Si. A tendency for the trend to saturate is observed at a higher reverse voltage, -1 V to show that the R_j at reverse voltage would not decrease indefinitely. At a certain reverse voltage greater than -2 V, R_j would attain a constant value that would be 4.43 MΩ. In forward bias, however the R_j trend of 10^{16} ion/cm^2 is higher than that of the undoped *n*-Si diode due to a further decrease in the densities of majority carriers as a result of charge recombination in the material. This recombination of the carriers results in an increase in the resistivity of Si.

The R_j trend in reverse bias for diodes fabricated on *n*-Si doped by Fe to a fluence of 10^{17} ion/cm^2 has decreased significantly, indicating a high charge carrier injection due to the high density of minority carriers introduced by the defects induced at this fluence. In forward, bias, however, the R_j trend of 10^{17} ion/cm^2 is higher than that of the undoped *n*-Si diode, indicating that the density of majority carriers has reduced due to the recombination of majority carriers by defects induced by Fe doping at this fluence.

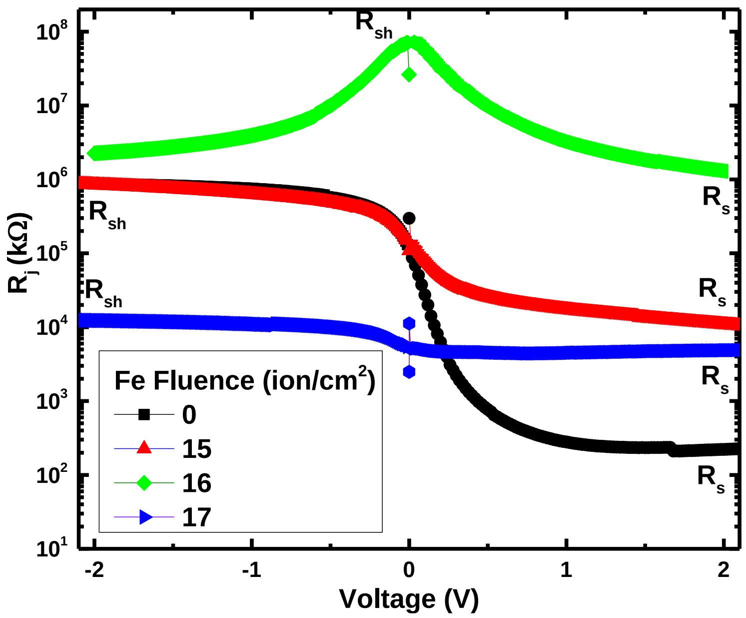

Fig. 6.4: *Diode resistances for undoped and Fe-doped n-Si.*

The summary of diode parameters evaluated using different methods, ln*(I)-V*, Cheung's, and R_j-*V* plots for the diodes fabricated on undoped and *n*-Si doped by Fe to different fluences are presented in Table 6.1.

Table 6.1: Device parameters evaluated using different methods for diodes fabricated on undoped and *n*-Si doped by Fe to the fluences of 10^{15}, 10^{16}, and 10^{17} ion/cm^2.

	ln(*I*)-*V*			**d*V*/dln(*I*)-*I***		***H*(*I*)-*I***		***R*j- *V***	
Fluence (Fe/cm^2)	η	I_s (nA)	ϕ_B(eV)	R_s (kΩ)	η	R_s (kΩ)	ϕ_B (eV)	R_{sh} (MΩ)	R_s (kΩ)
0	1.27 ± 0.10	29.33 ± 9.20	0.72 ± 0.01	0.27 ± 0.28	2.28 ± 0.57	0.74 ± 0.57	0.74 ± 0.02	4.43 ± 2.01	1.06 ± 0.86
10^{15}	2.98 ± 0.48	0.65 ± 0.32	0.64 ± 0.01	0.39 ± 0.15	3.55± 1.40	2.40 ± 1.11	0.73 ± 0.02	1.07 ± 0.15	3.05 ± 1.55
10^{16}	2.32 ± 0.25	77.75 ± 17.51	0.73 ± 0.02	5.13± 2.82	1.71± 0.21	24.55± 14.97	0.93± 0.05	31.26 ± 28.53	75.28 ± 24.36
10^{17}	3.64 ± 1.18	5.87 ± 3.26	0.58 ± 0.02	4.69± 3.01	4.02 ± 1.06	2.83 ± 1.60	0.40 ± 0.02	12.44 ± 0.75	2.43 ± 1.35

The η evaluated for undoped *n*-Si diode from ln(*I*)-*V* (1.27) and d*V*/dln(*I*)-*I* (2.28) methods is different due to the different voltage regions used to extract the parameters [11-12]. However, the value evaluated from ln(*I*)-*V* (1.27) is higher than 1.20 reported on Pd/*n*-Si [13] and lower than 4.39 reported on Cu/*n*-Si [14]. The η value obtained from dV/dln(I)-I (2.28) is higher than 1.55 reported on Pd/*n*-Si [13] and lower than 3.69 reported on Cu/*n*-Si structure [12]. Although the η evaluated for undoped *n*-Si diode in this work indicate that the diodes are non-ideal, it is within the range of those reported in the literature [11-13], confirming that the diodes were well fabricated. Furthermore, the high value of η reveals that, in addition to TE, other conduction mechanisms, such as tunnelling, contribute to the diode's forward current [14]. This tunnelling conduction mechanism is probably due to SiO_2 layer formed between Au and Si, resulting in a recombination of charge carriers through the interface states [15]. After Fe-doping, an increase in the η value is observed at all fluences, indicating an additional diode conduction mechanism. The increase in η observed after Fe-doping was also reported on Nb-doped [13] and Au doped *n*-Si diode [3].

The I_s evaluated for undoped *n*-Si diode, 29.33 nA, is higher than 4.3 nA reported on Pd/*n*-Si [13] and lower than and 8400 nA reported on Au/*n*-Si diode [16]. The I_s evaluated for undoped diode is within the range of those reported in literature [13, 16], indicating that the diodes were well fabricated using Au for Schottky contacts. The I_s value has increased after Fe-doping to the fluences of 10^{15} ion/cm^2, confirming the introduction of minority carriers in Si at this fluence which contributes to the measured reverse current of the diode. However, the I_s decreased after Fe-doping to the fluence of 10^{16} ion/cm^2, confirming the recombination of charge carriers reducing the density of minority carriers contributing to the reverse current. At the highest fluence, 10^{17} ion/cm^2, the I_s increases, confirming the introduction of minority carriers in Si at this fluence which contributes to the measured reverse current. An increase in I_s was also reported by [3, 13] and was said to be due to the minority carriers introduced by the doping metals in Si.

The ϕ_B evaluated for undoped *n*-Si diode using ln(*I*)-*V* and d*V*/dln(*I*)-*I* methods are different, 0.72 and 0.74 eV, respectively, due to the regions considered in extracting the parameters. The evaluated values of ϕ_B for undoped *n*-Si diode (0.72 and 0.74 eV), are close to 0.73 eV reported on Au/*n*-Si [8] and lower than 0.80 eV reported on Au/*n*-Si diodes [17], showing that our value is within the range of those reported in the literature [8, 17].

The variations of η and ϕ_B obtained from the ln*(I)-V* and Cheung's method with Fe fluence are presented in Figs. 6.5. A rapid increase (decrease) in η (ϕ_B) is observed at low fluence, indicating that the effect of the damage in the material by Fe is more at low fluence. As the fluence increases, the material becomes resistant to the damage resulting in a gentle increase in the η with fluence. This indicates that all Frenkel pairs created have been occupied by displaced atoms and impurities such that no more damage can occur in the material [18-19].

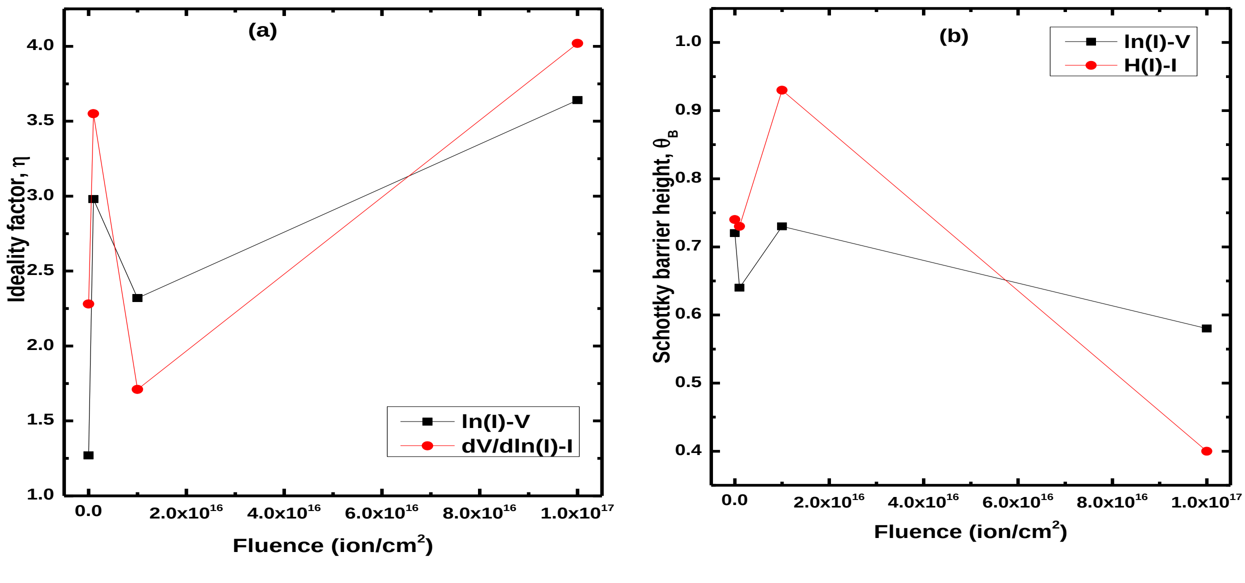

Fig. 6.5: *Ideality factor (a) and Schottky barrier height (b)evaluated from ln(I)-V and Cheung's plot as a function of Fe fluence.*

The η obtained from the Cheung's method shown in Fig. 6.5 (a) is expected to increase after Fe-doping at all fluences, but it is observed that diode fabricated on *n*-Si doped by Fe to the fluence of 10^{16} ion/cm^2 is lower than the value obtained on undoped *n*-Si diode. This discrepancy probably indicates that the parameter is less dependent on the defects induced in the material hence less pronounced when the diode conduction mechanism is completely dominated by charge carrier distribution in the bulk.

The R_{sh} evaluated for undoped *n*-Si diode is 4.43 MΩ, a value within the range of 1 to 100000 MΩ, reported in literature [8, 17], confirming that the diodes were well fabricated. R_{sh} slightly reduced after Fe-doping to the fluence 10^{15} ion/cm^2, indicating that at this fluence, the rate of generation of minority carriers is low. On the other hand, R_{sh} increased after Fe-doping to the fluence of 10^{16} ion/cm^2, indicating a low density of charge carriers due to recombination. The R_{sh} decreased drastically after Fe-doping to the fluence 10^{17} ion/cm^2, indicating a high generation of minority carriers at this fluence.

The R_s evaluated from different methods differs due to an increase in current rate due to space charge injection in an electric insulating layer at high voltage [20]. This indicates that an insulating layer has formed at the *m*-*s* interface. A thin layer of oxygen is present on the surface, even after chemical treatment of the wafer [21]. Thus, the formed interface layer could be SiO_2. However, R_{s} increased after Fe-doping for all fluences, indicating that at all fluences, Fe generates defects that recombine with majority carriers to increase the resistivity of the material.

The *I*-*V* characteristics of the diodes are presented in a double logarithmic scale in Fig. 6.6 to study the conduction mechanisms of the fabricated diodes. The forward current trend of the undoped *n*-Si diode (Fig. 6.6 (a)) shows three different linear regions, region i (0-0.06 V), region ii (0.06-1.11 V), and region iii (1.11-3 V), with slopes of 1.34, 2.91, and 0.94, respectively. These regions exhibit power-law behaviour, $I \propto V^m$, where *m* is the slope [22]. The slope of ~ 1.34 indicates that the current is directly proportional to the applied voltage at low voltage range for undoped *n*-Si diode. The dominant mechanism in this region is ohmic because the slope is close to unity and the ohmic behaviour is due to the domination of the thermally generated current over the injected free carrier generated current in the SCR [23-24]. The second region has a slope ~ 2.91, greater than 2, suggesting that a trapped-charge-limited current (TCLC) mechanism dominates at this region [23-24]. The diode conduction in this case could be governed by the space charge limited current (SCLC) with exponentially distributed surface states. In the third region, the slope 0.94 is close to unity, suggesting that the dominant mechanism is ohmic. Also, the slope has reduced because of the presence of R_s at high voltages.

Fig. 6.6 (b) shows the double logarithmic *I–V* plot of diodes fabricated on Fe-doped *n*-Si to the fluence of 10^{15} ion/cm^2. A linear region with a slope of 1.43 was identified on the entire voltage region. This slope is close to unity, indicating that the dominant current mechanism is ohmic throughout the voltage region. The reverse current trend remained unchanged, suggesting that Fe-doping at this fluence has a negligible effect on the reverse current. This could be showing that the induced defects at this fluence have negligible effects on the minority carriers. Furthermore, the gap between the reverse and forward trends has reduced especially at low voltage regions, showing a tendency of the diode exhibiting an ohmic *I-V* behaviour. This trend were also reported on Au doped *n*-Si diodes [16] and neutron-irradiated Si *p-i-n* diodes [25] and were attributed to generation-recombination (*g-r*) centres. The ohmic trend suggest that at the fluence of 10^{15} ion/cm^2, Fe generates *g-r* centres in Si. The *g-r* centres are defect levels positioned at the centre of the band gap. These defects interact equally with both the valence and conduction bands [26-27]. In this case, the Fermi energy is pinned at the intrinsic position, and it has been shown that it is unaffected by incident particles at this position [28]. This type of data analysis, double logarithmic *I-V* plot is also used to explain the ohmic behaviour of the diodes, hence the generation and recombination of the charge carriers.

The trends of diodes fabricated on *n*-Si doped by Fe to the fluence of 10^{16} ion/cm^2 is presented in Fig. 6.6 (c). Two regions were identified with slopes of 1.12 and 2.21 for region i (0-0.11 V) and region ii (0.12-2 V), respectively. A slope of 1.12 for region i is close to unity, indicating that the dominant current mechanism is ohmic in the voltage region, while a slope of 2.20 for region ii suggests that the region is dominated by SCLC. According to SCLC mechanism, the density of the injected free carriers is much greater than the density of the thermally generated free carriers [23-24]. At 0-1 V, both reverse and forward currents are the same, indicating that the rate of charge carrier generation (g) is equal to the rate of charge recombination (r) at this voltage. Hence, $g = r$ if charge distribution in the material is dominated by defect levels at the centre of the Si band gap [29]. However, the forward current is slightly higher than the reverse current at voltages higher than 1.1 V, indicating that the density of Fe-induced g-r centres is not enough for the trend to be ohmic for the whole voltage range. Also, both trends are lower than the trends of undoped *n*-Si diode with the forward current reducing by a factor higher than that of the reverse current after Fe-doping at this fluence. This decrease in current trends indicates an increase in the resistivity of the material after doping.

The trends of the diodes fabricated on *n*-Si doped by Fe to the fluence of 10^{17} ion/cm^2 presented in Fig 6.6 (d). A linear region on the forward current trend is observed for the whole voltage region with a slope of unity, indicating that the dominant current mechanism is ohmic throughout the voltage region. The forward and reverse current trends are the same at low voltage range of 0-0.1 V, indicating that a charge distribution mechanism in the material is dominated by g-r centres at this voltage range. Since the density of defect levels at the centre of the band gap (g-r centres) increases with fluences [27, 30], it was expected that both trends would be the same for the whole voltage range for this diode. However, the trend observed is not the same for the whole voltage range as the forward current is higher than the reverse current after 0.1 V. This discrepancy could be due to holes dominating material conductivity at high voltage range as a result of conductivity-type inversion.

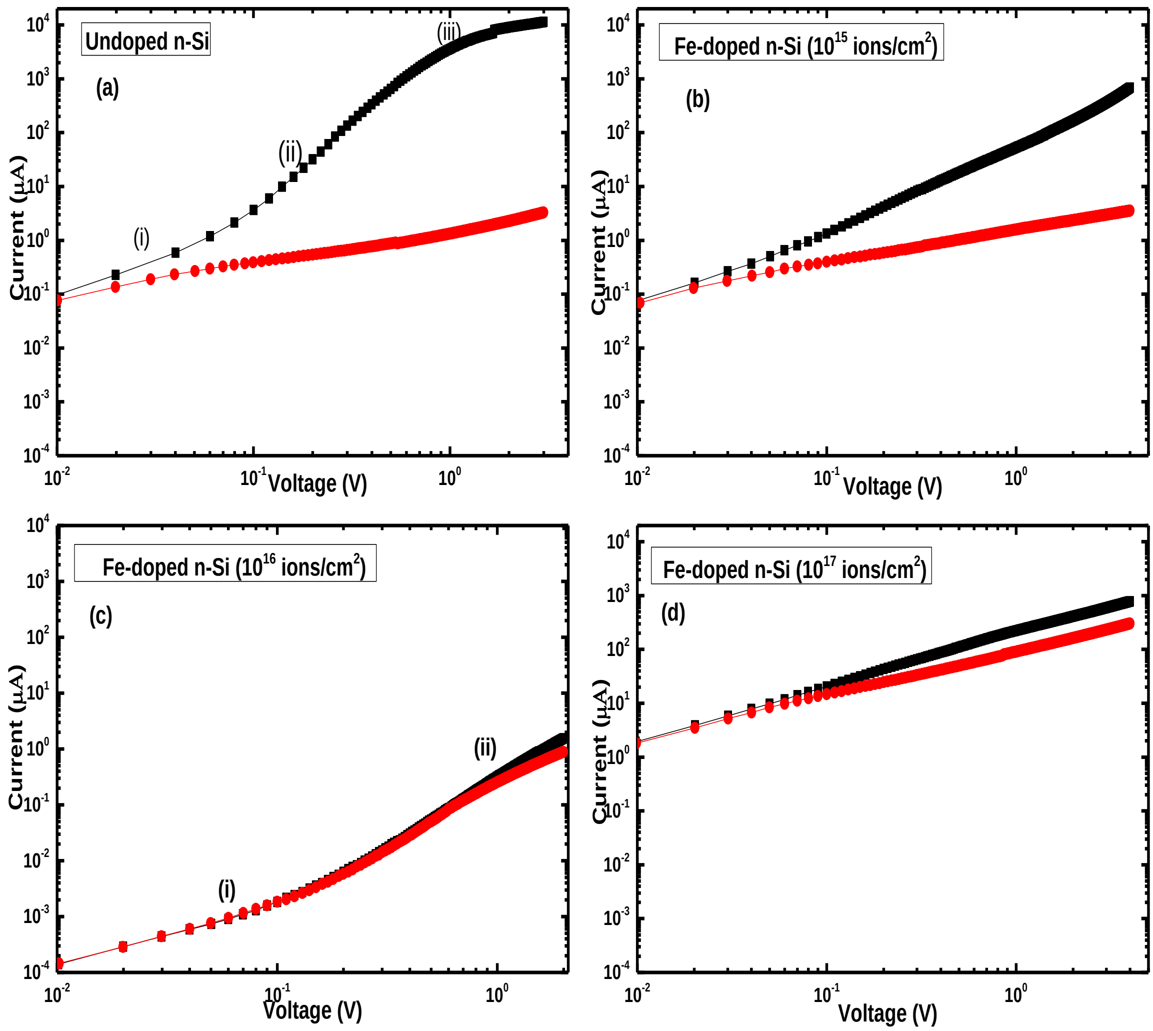

Fig. 6.6: *I-V characteristics of the diodes fabricated on undoped n-Si (a), Fe-doped n-Si at a fluences of 10^{15} (b), 10^{16} (c), and 10^{17}(d) ion/cm^2 in a double logarithmic scale.*

A change in rectifying behaviour of *n*-Si diode due to Fe-doping is investigated by rectification ratio (RR) evaluated from Fig. 6.6. RR is a ratio of the forward current to the reverse current at 4 V. As shown in Fig. 6.7 (a), the RR decreased from 3011.49 to 177.22 after Fe-doping to the fluence of 10^{15} ion/cm^2, then further decreased to 1.47 after Fe-doping to the fluence of 10^{16} ion/cm^2 before increasing gently to 3.38 at Fe-doping to the highest fluence (10^{17} ion/cm^2).

A decrease in RR was also reported on irradiated Si *p-i-n* diodes and it was explained in terms of an increase (decrease) in the density of minority (majority) charge carriers [31]. At the fluence, 10^{16} ion/cm^2, where the intensity of acceptor and donor levels are equal, the material exhibits intrinsic-like behaviour, and its resistivity(conductivity) is at maximum(minimum)

[29]. This work shows that when the resistivity of Si is at maximum, a device fabricated on the material is ohmic with a RR close to unity. With an increase in Fe-doping fluence, the RR increases gently with fluence. This increase indicates that the conductivity of the material is dominated by holes at high voltages, indicating a conductivity type inversion from *n*- to *p*-type.

The slope at which the RR changes before Fe-doping to the fluence of 10^{16} ion/cm^2 is higher than the slope after the fluence of 10^{16} ion/cm^2, though Fe is implanted at the same rate in Fig. 6.7 (a). A difference in slopes indicates that a charge carrier distribution mechanism is not due to only donor and acceptor levels but also *g-r* centres in Si. This involvement of *g-r* centres in the conduction mechanism was observed by ohmic behaviour exhibited by the Fe-doped Si diodes.

Fig. 6.7 (b) shows the variation of diode R_s from different methods with Fe fluence. A rapid increase in R_s trend is observed up to a fluence of 10^{16} ion/cm^2, the fluence at which conductivity-type inversion occurs and then decreases gently with an increase in Fe fluence. The high value of R_s observed at the fluence of 10^{16} ion/cm^2 could be attributed to the high density of *g-r* centres associated with this fluence. Also, the high R_s associated with this fluence indicates an increase in the resistivity of the Si material. At this fluence, 10^{16} ion/cm^2, where the intensity of the acceptor and donor levels is equal, the material exhibits intrinsic-like behaviour and its conductivity (resistivity) is at a minimum (maximum) [29].

The trend in Figs. 6.5, 6.6, and 6.7 confirms that the conductivity of *n*-Si has been inverted from *n*- to *p*-Si. The difference in slopes in Fig 6.7 (b) also indicates that the hole generation rate is higher before the conductivity-type inversion. A conductivity-type inversion was reported on the diodes that were irradiated by 1 MeV neutrons to the fluence of $1.0 \times 10^{14}\ \mathrm{n.cm^{-2}}$ [32]. This conductivity type-inversion of the material was also reported on the diodes that were fabricated on Pt-doped *n*-Si diode [33-34]. Thus, in Si, Fe exhibits properties similar to neutron-irradiation and Pt-doping.

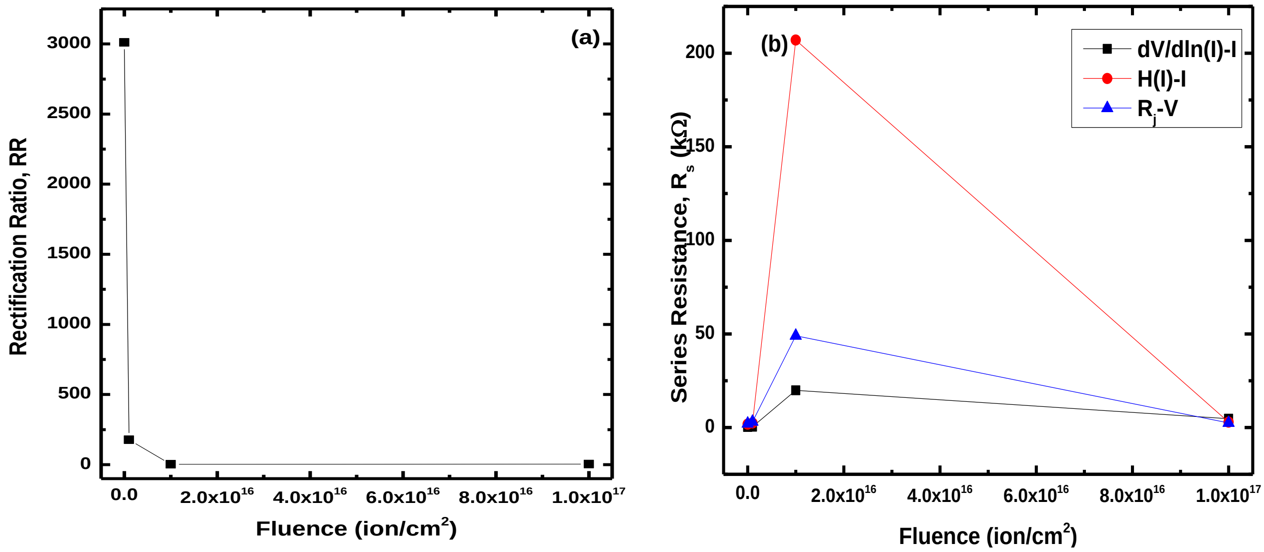

Fig. 6.7: *Rectification ratio (a) and series resistance from dV/dln(I)-I, H(I)-I, and R_j-V (b) versus fluence.*

6.1.1.2 *p*-Silicon diodes

The *p*-Si was doped by Fe to the fluence of 10^{17} ion/cm^2. The *I-V* characteristics of the diodes fabricated on undoped and Fe-doped *p*-Si were presented in a linear scale (not shown). The switching-on was only observed on the diode fabricated on undoped *p*-Si. Since there was no other scientific information about the scale, the plots were not presented.

The ln(*I*)-*V* characteristics of undoped and Fe-doped *p*-Si diode is presented in Fig. 6.8. A linear region is observed at low voltages but disappeared after 1 V and 0.4 V for undoped and Fe-doped *p*-Si diode, respectively. The absence of the linear region at high voltage is possibly due to the effect of R_s [6], interface states [35], and interfacial insulator layer [36]. The linear region in the forward characteristics of Fe-doped *p*-Si diode is smaller suggesting that the Fe-induced defects have affected the diode R_s.

The current trends in Fig. 6.8 increased after Fe-doping by a factor of 10^2 and 5 for reverse and forward current, respectively. The increase observed in the current trends indicates that Fe-induced defects generate both minority and majority carriers in the SCR thereby increasing the conductivity of the material.

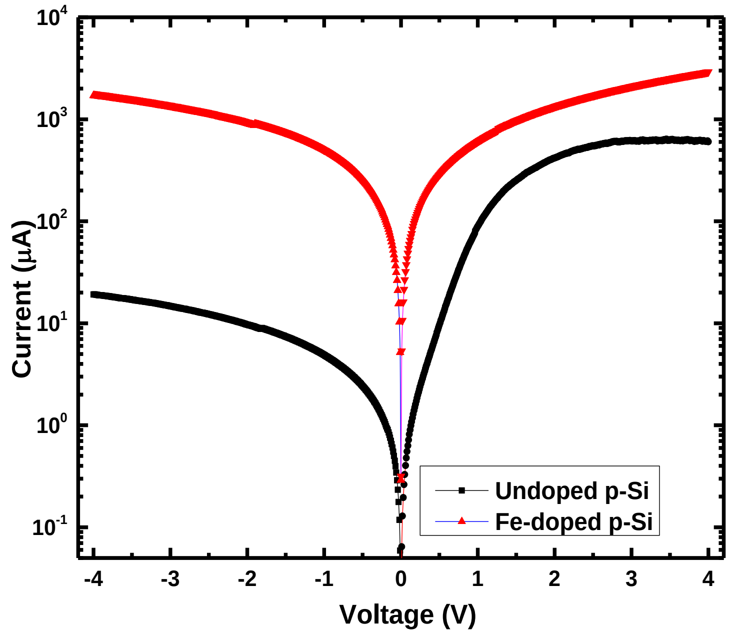

Fig. 6.8: *Forward and reverse bias ln(I)-V characteristics of diodes fabricated on undoped and Fe-doped p-Si.*

The values of R_s η, and ϕ_B were calculated using Cheung's method [5]. As shown in Fig. 6.10, plots of d*V*/dln(*I*)-*I* and *H(I)-I* are linear for the whole voltage range. The values of R_s, η, and ϕ_B are evaluated from the linear region in Fig. 6.9. The diode parameters evaluated from Figs. 6.8 and 6.9 are presented in Table 6.2.

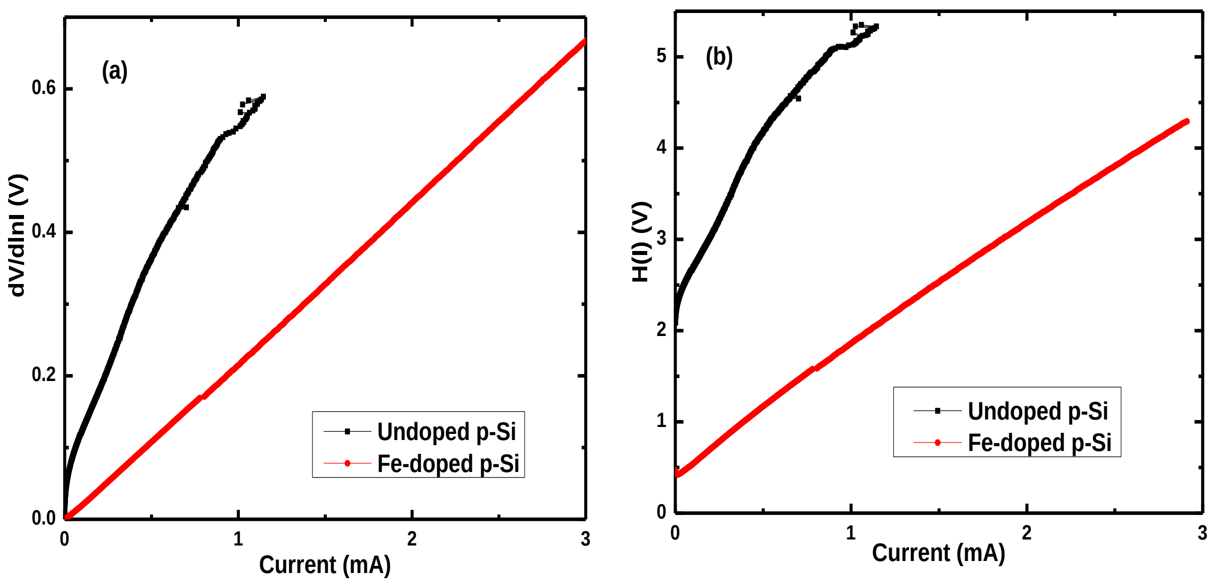

Fig. 6.9: *dV/dln(I)-I (a) and H(I)-I (b) characteristics of the diodes fabricated on undoped and Fe-doped p-Si.*

Fig. 6.10 shows the R_j-V plots for undoped and Fe-doped *p*-Si diodes. The R_j of undoped *p*-Si diode is independent of the reverse voltage, suggesting that the SCR extends into the bulk and the material resistivity remains constant. The saturation of R_j is expected since the bulk of the material is relatively defect-free. The R_j of undoped *p*-Si -based diode decreases with forward voltage as a result of the high density of free charge carriers through the SCR.

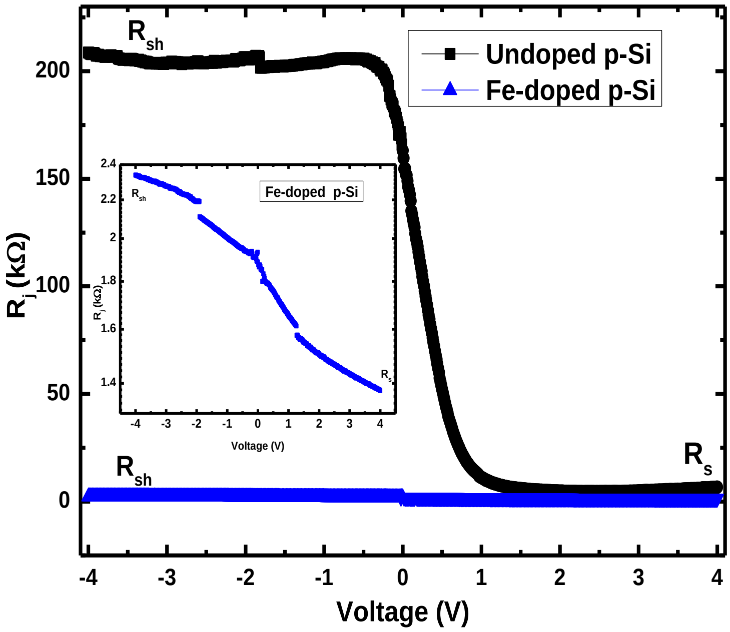

Fig. 6.10: *Diode resistances for undoped and Fe-doped p-Si. Inset: diode resistance for Fe-doped p-Si.*

The R_j of diode fabricated on Fe-doped *p*-Si is independent of reverse and forward voltages due to the high density of charge carriers introduced in the SCR by the Fe-induced defects. Also, the high density of charge carriers generated by Fe-induced defects is confirmed by the significant decrease in R_j in both reverse and forward bias. The inset of Fig 6.10 shows the R_j-V plot of the Fe-doped p-Si in a smaller scale. The R_s and R_{sh} of the fabricated diodes are calculated from the plot of R_j-V and are presented in Table 6.2.

The summary of diode parameters evaluated using different methods, ln*(I)*-*V*, Cheung's, and R_j-V plots for the undoped and Fe-doped *p*-Si diodes are presented in Table 6.2.

Table 6.2: Device parameters evaluated using different methods for diodes fabricated on undoped and Fe-doped *p*-Si.

	ln(*I*)-*V*			d*V*/dln(*I*)-*I*		*H(I)-I*		R_j-*V*	
Diodes	η	I_s (nA)	ϕ_B(eV)	R_s (kΩ)	η	R_s (kΩ)	ϕ_B(eV)	R_{sh} (kΩ)	R_s (kΩ)
Undoped *p*-Si	2.35 ± 0.48	72.52 ± 38.73	0.66 ± 0.02	0.76 ± 0.33	2.79 ± 0.41	5.16 ± 2.76	0.77 ± 0.02	209.79 ± 4.17	5.70 ± 2.64
Fe-doped *p*-Si	2.65 ± 0.25	6940 ± 1580.0	0.55 ± 0.01	0.26 ± 0.04	0.69 ± 0.22	1.52 ± 0.32	0.77 ± 0.03	2.63 ± 0.45	1.59 ± 0.33

The η evaluated from ln*(I)-V* (2.35) and d*V*/dln*(I)-I* (2.79) for an undoped *p*-Si diode are higher than unity, showing a non-ideal behaviour of the diodes. The disparity in values of 0.44 could be attributed to the different voltage regions used in the methods. Based on the Al/SnO_2/*p*-Si structure [11], a value of 2.0 was reported, which is similar to the one evaluated in our study. The η for the undoped *p*-Si diode agrees with metal-insulator-semiconductor configuration rather than an ideal Schottky diode, indicating the presence of an insulating layer in the diode structure [37-39].

The η evaluated from ln*(I)-V* increased after Fe-doping, indicating an additional conduction mechanism. The η from Cheung's method is 0.69, a value close to unity, indicating the only conduction mechanism is TE though the *I*–*V* trends indicate that other diode conduction mechanisms are involved. The η close to unity evaluated for this diode probably indicates that the parameter is less dependent on the defects induced in the material hence less pronounced when the diode conduction mechanism is completely dominated by charge carrier distribution in the bulk.

The I_s evaluated on undoped *p*-Si is 72.52 nA, higher than 1.23 nA reported on Al/methyl violet/*p*-Si [40] and lower than 87100 nA reported on undoped *p*-Si diode [41] respectively, indicating that it is within the range of those presented in literature [40, 41]. An increase in

I_s from 72.52 to 6940 nA is observed after Fe-doping. An increase in I_s is attributed to the increase in the density of minority carriers due to the Fe-induced defect levels in Si.

The ϕ_B evaluated using ln*(I)-V* and H*(I)-I* methods for undoped *p*-Si diodes are 0.66 and 0.77 eV, respectively. The ϕ_B evaluated using *H(I)-I* method is higher than ϕ_B evaluated using ln*(I)-V*, possibly due to different voltage regions considered when extracting the parameters. This difference has been observed before [40]. The value of ϕ_B (0.66) evaluated from ln*(I)-V* is close to 0.68 eV reported on polypyrrole/*p*-Si/Al [42] and the value of ϕ_B (0.77) evaluated from *H(I)-I* is close to 0.80 eV reported on Sn/MB/*p*-Si [43], confirming the formation of the metal-semiconductor interface during the diode fabrication process. The values of ϕ_B evaluated using different methods were found to decrease after Fe-doping. The decrease in ϕ_B can be tied to an increase in I_s as shown in Fig. 6.9 and Table 6.2, respectively.

The parasitic resistance (R_{sh} and R_s) for the undoped *p*-Si diodes are 209.79 and 5.70 kΩ, respectively. The high(low) values for R_{sh} (R_s) of the undoped *p*-Si diode evaluated from the R_j-*V* plot confirms the good rectification behaviour of the diode [9]. R_{sh} and R_s for the Fe-doped *p*-Si diode is 2.63 and 1.52 kΩ, respectively. The drastic decrease in the value of R_{sh} and R_s after Fe-doping is because of the high density of minority and majority carriers generated by the Fe-induced defects. In addition, the significant decrease in the values of R_s and R_{sh} indicates an increase(decrease) in the material conductivity(resistivity) due to the generation of charge carriers by Fe-induced defects in *p*-Si.

Fig. 6.11 (a) shows three linear regions with different slopes on the forward current trend of the undoped *p*-Si. The slopes of these regions are 1.06, 2.58, and 0.64, respectively. The slope of the first region, 1.06 is close to unity, indicating that the dominating mechanism in this region is ohmic. The slope of the second region is 2.58, a slope greater than 2, showing that the

TCLC dominates in the region. The slope of the third region (0.64) is less than unity, indicating the current is less dependent on voltage, possibly because of R_s present at high voltages.

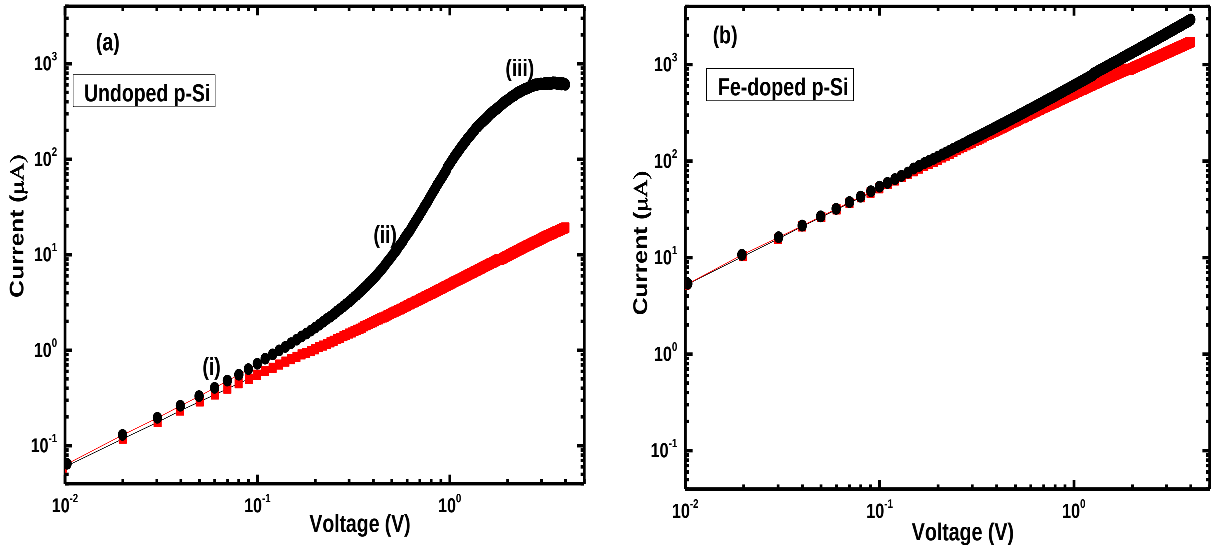

Fig. 6.11: *I-V characteristics of the diodes fabricated on undoped (a) and Fe-doped (b) p-Si in a double logarithmic scale.*

The double logarithmic *I-V* trend of Fe-doped *p*-Si diode is shown in Fig. 6.11 (b). The forward current increases linearly for the whole voltage region with a slope of unity, indicating an ohmic conduction mechanism dominates at the entire voltage region. Furthermore, the reverse and forward current trends are the same for almost all through the voltage region, indicating that the diode behaviour in general is ohmic. The ohmic behaviour indicates that density of Fe-induced *g-r* centres is very high. Diodes that show a high ohmic region have been found to be resistant to radiation damage and were described in terms of a high concentration of defect levels positioned at the centre of the Si band gap [26, 28].

A change in rectifying behaviour of a diode due to Fe-doping is investigated by the RR evaluated from both diodes. The RR is found to be reduced from 33.61 to 1.65 after Fe-doping. It can be seen from Fig. 6.11 that both carrier densities have increased with the rate of increase in density of minority carrier being higher.

6.1.1.3 *i*-Silicon diodes

The ln(*I*)-*V* plots of undoped and Fe-doped *i*-Si diode are presented in Fig. 6.12 to further investigate a change in *I*-*V* characteristics of the diodes with Fe-doping. A linear region is observed at the low voltages but disappeared after 0.63 and 0.37 V in undoped and Fe-doped *i*-Si diode, respectively. The absence of the linear region at high voltage observed in both diodes is reported to be due to the effect of R_s [6], interface states [36] and interfacial insulator layer [37]. The linear region in the forward characteristics of Fe-doped *i*-Si diode is smaller suggesting that the Fe-induced defects affect the diode R_s.

The reverse current trend increased by a factor of ~10^4 while the forward current trend reduced slightly at the low voltage region (0-2 V) but remained the same at a voltage higher than 2 V after Fe-doping. The rapid increase in reverse current suggests that Fe generates high density of minority carriers in *i*-Si while the slight reduction in forward current confirms the recombination of majority carriers in *i*-Si by Fe-induced defects.

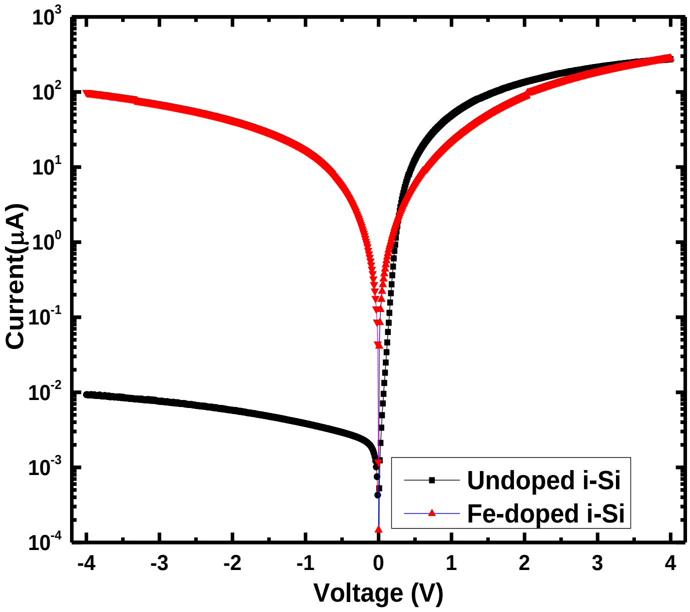

Fig. 6.12: *Forward and reverse bias ln(I)-V characteristics of diodes fabricated on undoped and Fe-doped i-Si.*

The values of R_s, η, and ϕ_B were calculated from the plots of d*V*/dln(*I*) and *H(I)-I* presented in Fig. 6.13. The values of R_s, η, and ϕ_B are evaluated from the linear region in Fig. 6.13. The diode parameters evaluated from Figs. 6.12 and 6.13 are presented in Table 6.3.

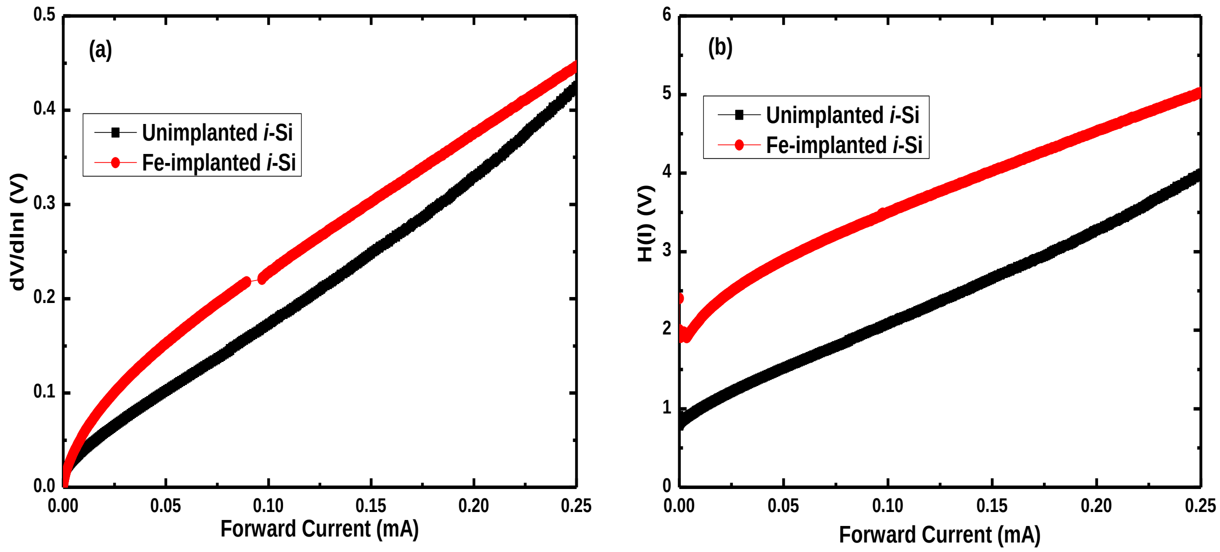

Fig. 6.13: *dV/dln(I)-I (a) and H(I)-I (b) characteristics of the diodes on undoped and Fe-doped i-Si.*

Fig. 6.14 presents R_j-*V* plot for the undoped and Fe-doped *i*-Si diodes. R_j of the undoped *i*-Si diode is independent of the reverse voltage, indicating that SCR extends into the bulk and the material resistivity is constant. The saturation of R_j is expected since the bulk of the material is relatively defect-free. On the forward bias, as expected R_j decreases due to high density of free charge carriers through SCR.

The R_j of the Fe-doped *i*-Si diode decreased gently with reverse voltage, indicating a low charge injection rate in SCR. An absence of saturation of R_j after Fe-doping in reverse bias shows that the density of defects associated to Fe-doping decreases with penetration depth of Fe in the bulk of Si. A tendency of the trend to saturate is observed at higher reverse voltage, from −1 V to show that the R_j at reverse voltage would not decrease indefinitely. At a certain reverse voltage greater than − 4 V. The R_s and R_{sh} obtained from R_j-*V* plot is presented in Table 6.3.

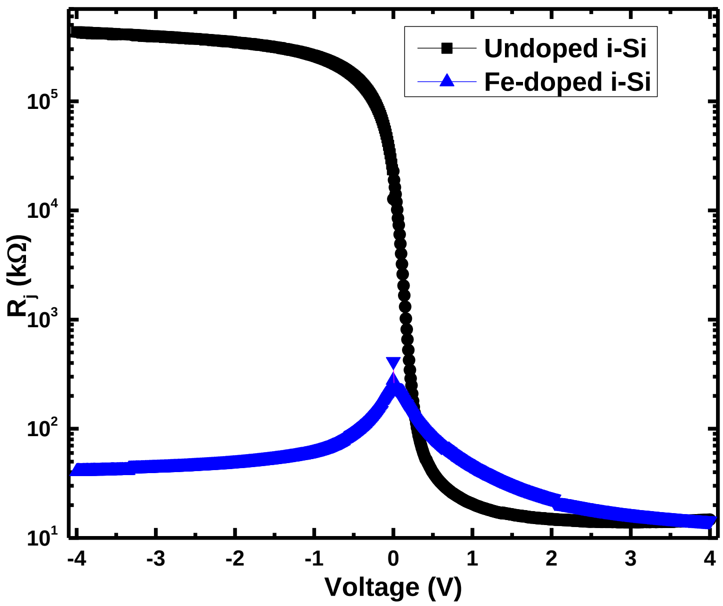

Fig. 6.14: *Diode resistances for diodes fabricated on undoped and Fe-doped i-Si.*

The summary of diode parameters evaluated from different methods, ln*(I)*-*V*, Cheung's, and R_j-*V* plots for the undoped and Fe-doped *i*-Si diodes are presented in Table 6.3.

Table 6.3: Device parameters evaluated using different methods for diodes fabricated on undoped and Fe-doped *i*-Si.

	ln(*I*)-*V*			d*V*/dln(*I*) - *I*		*H(I)* - *I*		R_j - *V*	
Diodes	η	I_s (nA)	$\phi_B(eV)$	R_s (kΩ)	η	R_s (k Ω)	ϕ_B(eV)	R_{sh} (MΩ)	R_s (k Ω)
Undoped *i*-Si	1.65 ± 0.19	2.78 ± 0.97	0.78 ± 0.02	4.15 ± 1.28	1.54 ± 0.08	32.41 ± 12.39	0.66 ± 0.10	93.26 ± 17.94	34.93 ± 8.11
Fe-doped *i*-Si	2.92± 1.00	270.0± 240.00	0.67 ± 0.04	1.05 ± 0.45	2.39 ± 0.99	7.25 ± 3.33	0.87 ± 0.05	207.17± 168.49	14.92 ± 1.18

The η evaluated for undoped *i*-Si diode from ln(*I*)-*V* and d*V*/dln(*I*)-*I* plots are 1.65 and 1.54, respectively. These values are close to each other with a difference of 0.11 which could be due to the different voltage regions considered when extracting the parameters [11]. A value of 1.55 close to our value was reported on Au/polyvinyl alcohol (Co, Zn-doped)/*n*-Si [44] and 2.31 greater than our value was reported on Au/Bi-doped PVA/*n*-Si [8]. Though η evaluated in this work is more than unity, indicating a non-ideal diode behaviour. However, the value still falls within the range of those reported in literature [11-13], indicating that our diodes were well fabricated. The evaluated η for Fe-doped *n*-Si diode using ln(*I*)-*V* and d*V*/dln(*I*)-*I* methods was found to increase. An increase was in η has been reported before and was attributed to other diode conduction mechanisms than TE [3, 13].

The I_s evaluated for undoped *i*-Si diode is 2.78 nA, a value higher than 0.18 nA obtained on Au/*n*-Si [45] and close to 1.04 nA reported on Sn/*p*-Si Schottky diode [46], The I_s evaluated is within the range of those reported in literature [45-46], indicating that our diodes were well fabricated using Au as Schottky contact. The I_s evaluated on the Fe-doped *i*-Si diode increased in from 2.78 nA to 420 nA. An increase in I_s has been reported on niobium-doped Si diode and was said to be due to the niobium-induced defects that generates minority carriers in Si, resulting to an increase in I_s [3, 13].

The ϕ_B evaluated for undoped *i*-Si diode using ln*(I)-V* and *H(I)-I* methods are 0.78 eV and 0.66 eV, respectively. The difference in the values is possibly due to different voltage regions considered when extracting the parameters [12]. The ϕ_B evaluated from ln*(I)-V* for undoped *i*-Si diode (0.78 eV) is lower than 0.87 eV reported on Au/*n*-Si [44], and greater than 0.75 eV reported on Sn/*p*-Si Schottky diode [46]. Our value is within the range of those reported in literature, confirming the formation of the metal-semiconductor interface during the diode fabrication process. The ϕ_B evaluated using different methods are found to decrease after Fe-doping, indicating that Fe-induced defects generate minority carriers in Si which in turn increases the I_s. The decrease in ϕ_B after Fe-doping also agrees with the result obtained by Thebe *et al* on niobium doped Si diode [3, 13].

The low(high) values for R_s (R_{sh}) on the undoped *i*-Si diode evaluated from the $R_j - V$ plot confirms the good rectification behaviour of the diode [9]. The significant decrease in the values of R_{sh} after Fe-doping is as a result of the high density of minority carriers generated by the Fe in Si. The R_s evaluated using different methods are different. However, all methods showed a decrease in R_S after Fe-doping, indicating recombination of some majority carriers by the generated minority carriers.

The double logarithmic *I-V* plot of the undoped *i*-Si diode presented in Fig. 6.15 (a) shows three different linear regions on the forward current trend, representing different current transport mechanisms. The first region (0-0.07 V) with a slope, 1.48, close to unity indicates that the dominant mechanism is ohmic in this region. The second region (0.08-0.54 V) with a slope of 3.95, this slope is greater than 2, indicating that the region is dominated by TCLC. The slope of the last region (1.27) has reduced due to the presence of R_S at high voltages.

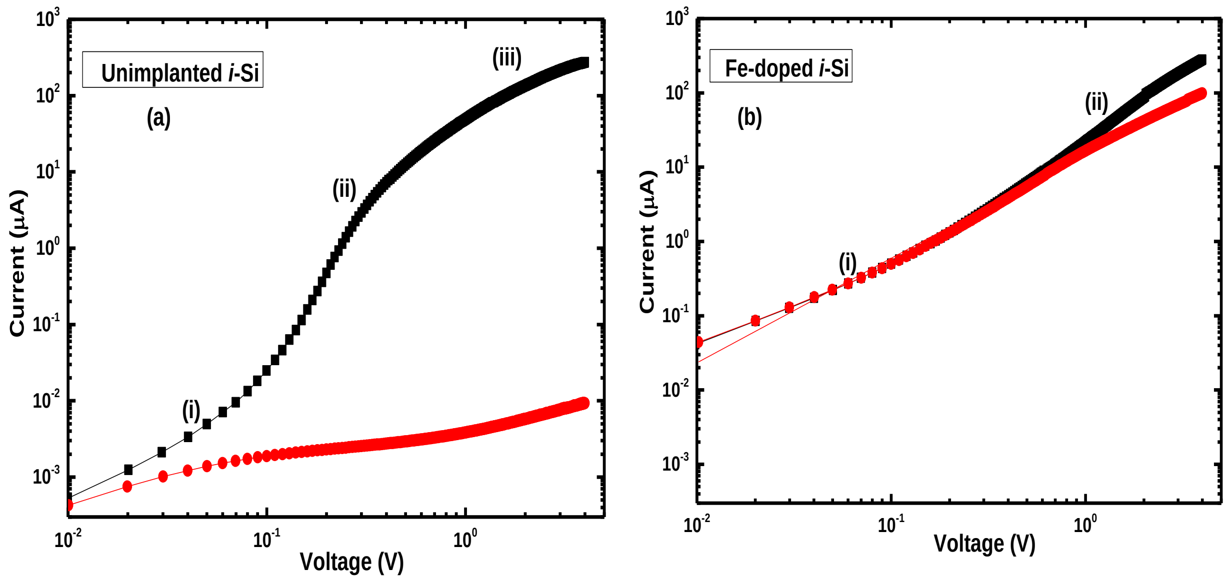

Fig. 6.15: *I-V characteristics of the diodes fabricated on undoped (a) and Fe-doped (b) i-Si in a double logarithmic scale.*

The double logarithmic *I-V* plot of the Fe-doped *i*-Si diode presented in Fig. 6.15 (b) shows two linear regions with the slope, 1.41 for the first region (0-0.19 V) close to unity, indicating that the dominant mechanism in the region is ohmic. The second region (0.2-4 V) has a slope of 1.88, a slope close to 2, indicating that SCLC is dominant in the region. The diode is ohmic as reverse and forward current is the same for almost all through the voltage range as seen in Fig. 6.15 (b), indicating that the Fe-induced defects are responsible for the generation of *g-r* centres resulting to an increase in the ohmic region of the diode. It is to be noted that the density of *g-r* centres is not high enough to make both reverse and forward trend equal for the whole voltage range. The RR is found to decrease from 33470 to 2.59 after Fe-doping. The decrease was also observed on diodes fabricated on Fe-doped *n* and *p*-type Si material, indicating that the effect of Fe-doping on *i*-Si is similar to that of *n* and *p*- Si.

6.1.2. Cd-doped Si diodes

6.1.2.1 *p*-Si diodes

The ln(*I*)-*V* plots of the undoped and Cd-doped *p*-Si diodes are shown in Fig. 6.16. A linear increase of current in this scale is observed at low voltage regions, 0-1 V and 0-0.55 V for undoped and Cd-doped *p*-Si diode, respectively. The linear region disappeared at high voltages possibly due to the effect of R_s [6], interface states [36], and interfacial insulator layer [37] for both diodes.

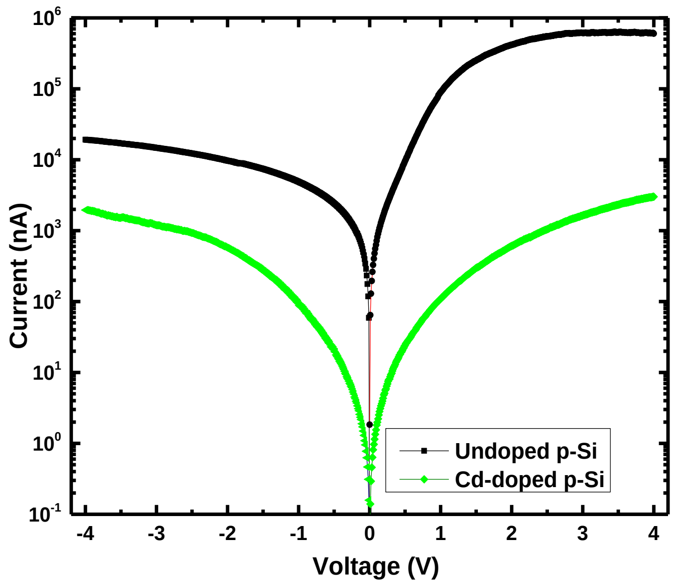

Fig. 6.16: *Forward and reverse bias ln(I)-V characteristics of diodes fabricated on undoped and Cd-doped p-Si.*

The current trends in Fig. 6.16 decreased by a factor of ~ 10^1 and 10^3 for reverse and forward trends, respectively, indicating a decrease (increase) in the conductivity (resistivity) after Cd-doping. An increase in the resistivity indicates that Cd-induced defects in Si act as recombination centres. Also, the decrease in reverse and forward current may suggest that Cd-induced defects are also responsible for the compensation of the majority carriers. In any case, then, the density of charge carriers in the SCR reduces, resulting in an increase in the resistivity of the material. An increase in the resistivity has been reported on the diodes that were fabricated on *p*-Si doped with Au and Pt [41].

The R_s was calculated from the graphs of d*V*/dln(*I)* and *H(I)-I* presented in Fig. 6.17, where R_s, η, and ϕ_B, are obtained from the plots. The values of R_s, η, and ϕ_{B} are evaluated from the linear region in Fig. 6.17. A drastic increase in d*V*/dln(*I)* and *H(I)-I* at high current observed in Fig. 6.17 is unusual and it may be attributed to the existence of high resistivity layer at the *m-s* interface. The inset of Figs. 6.17 (a) and (b) are the plot of d*V*/dln(*I)* and *H(I)-I* for Cd-doped *p-Si* diode. The diode parameters evaluated from Figs. 6.16 and 6.17 are presented in Table 6.4.

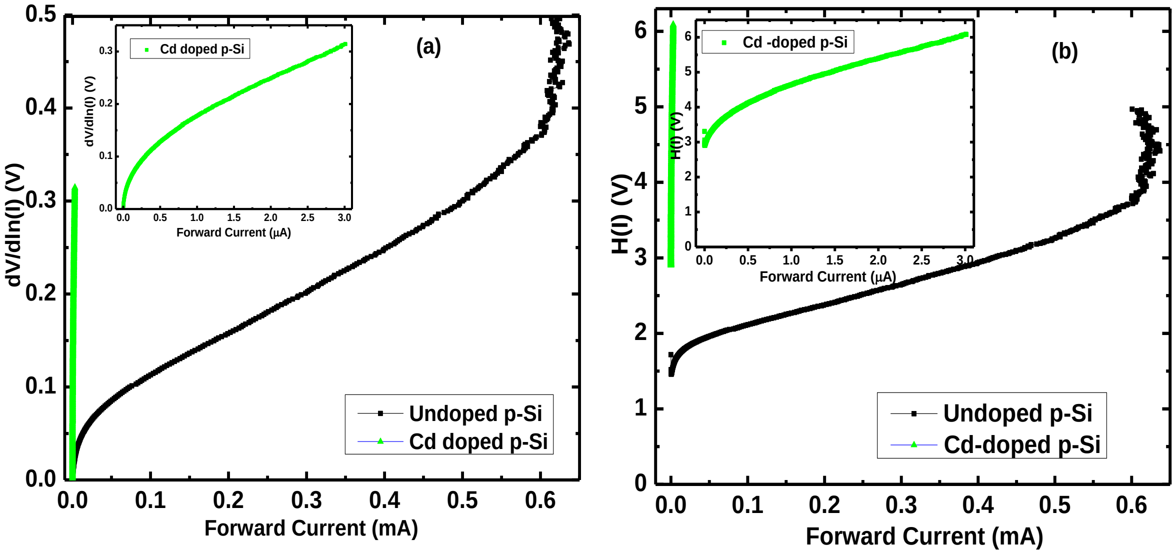

Fig. 6.17: *dV/dln(I)-I and H(I)-I plots on undoped p-Si (a) and Cd-doped p-Si diodes (b). Inset: plot of dV/dln(I) and H(I)-I for Cd-doped p-Si diode.*

Fig. 6.18 presents the R_{j}-*V* plot for the undoped and Cd-doped *p*-Si diodes. A gentle decrease in R_{j} with negative voltage on Cd-doped *p*-Si diode indicates a slow charge carrier injection rate in SCR. A tendency of the trend to saturate is observed at higher reverse voltage, -2 V. An absence of R_{j} saturation with the applied voltage in the trend of observed on Cd-doped *p*-Si diode indicates that the density of Cd-induced defects decreases with Cd penetration depth in the bulk. It is believed that the trends for the Cd-doped diode would not decrease indefinitely. It is expected that a certain voltage higher than -4 V, R_j would be ~ 0.21 MΩ and then remain independent of the voltage.

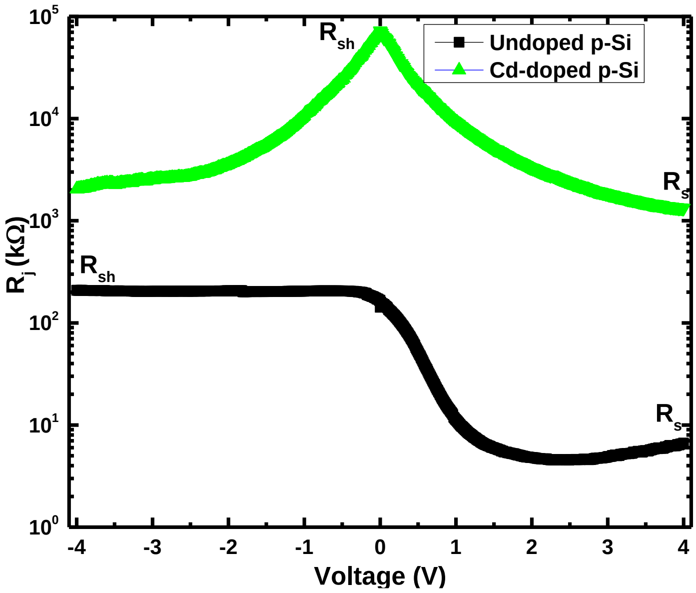

Fig. 6.18: *Diode resistances for undoped and Cd-doped p-Si diodes.*

The average of device parameters evaluated from different methods, ln*(I)-V*, d*V/*dln(*I)-I, H(I)-I,* and R_j-*V* plots for diodes fabricated on undoped and Cd-doped *p*-Si are given in Table 6.4.

Table 6.4: Device parameters evaluated using different methods for diodes fabricated on undoped and Cd-doped *p*-Si.

	ln(*I*)-*V*			d*V*/dln(*I*)-*I*		*H(I)-I*		R_j -*V*	
Diodes	η	I_s (nA)	ϕ_B (eV)	R_s (kΩ)	η	R_s (kΩ)	ϕ_B (eV)	R_{sh} (MΩ)	R_s (k Ω)
Undoped *p-Si*	2.35 ± 0.48	72.52 ± 38.73	0.66 ± 0.02	0.76 ± 0.33	2.79 ± 0.41	5.16 ± 2.76	0.77 ± 0.02	0.21 ± 0.004	5.70 ± 2.64
Cd-doped *p-Si*	3.31 ± 0.22	0.17 ± 0.14	0.83 ± 0.04	561.92 ± 254.15	4.27 ± 1.52	10.97 ± 4.72	0.88 ± 0.25	209.88 ± 100.65	14.07 ± 4.24

The η evaluated from the two methods increased after Cd-doping, indicating an additional conduction mechanism has been introduced. The I_s decreased after Cd-doping. A decrease in I_s is attributed to a reduction in charge carrier density as a result of Cd-induced defect levels in the Si band gap. These levels are responsible for recombination/compensation of charge carriers, resulting in an increase in the resistivity of the material after Cd-doping. The ϕ_B values evaluated using different methods are found to increase after Cd-doping. The R_s and R_{sh} increased after Cd-doping, confirming the increase in the resistivity due to recombination of charge carriers by Cd-induced defects in Si.

The double logarithmic *I-V* plot of the Cd-doped *p*-Si diode presented in Fig. 6.19 (b) shows two linear regions with the slope (1.21) for the first region (0-0.6 V) being close to unity, indicating that ohmic dominates at this region. The second linear region (0.61-4 V) with a slope of 2.27 indicates that SCLC dominates at this region. The slope at this region has decreased after Cd-doping, indicating that the density of carriers has reduced due to recombination of charge carriers as a result of Cd-induced defects. The trends have come close to each other and shifted downward for Fig. 6.19 (b), indicating the density of Cd-induced *g-r* centres have increased leading to an ohmic behaviour. The ohmic region has also increased, indicating that $g = r$ for almost all the voltage region in this diode. Diodes with ohmic behaviour have been found to be resistant to radiation damage and this is due to the high density of defect levels created in the centre of the band gap [26, 29]. Also, the downward shift of the trends confirmed the increase in resistivity of the material.

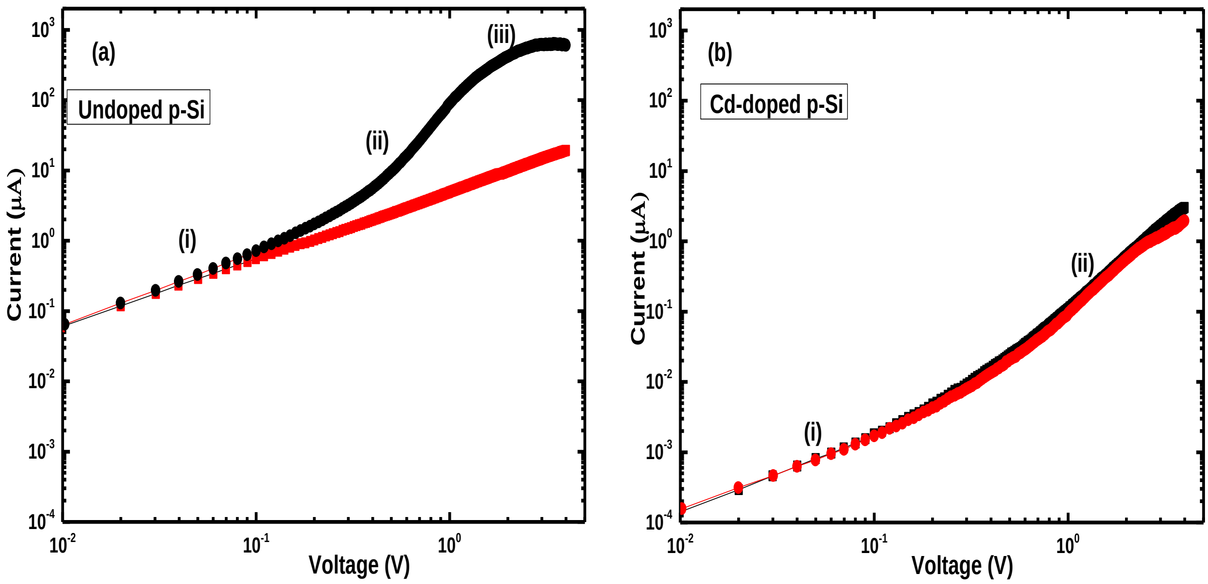

Fig. 6.19: *I-V characteristics of the diodes fabricated on undoped p-Si (a) and Cd-doped (b) p-Si in a double logarithmic scale.*

A change in rectifying behaviour of a diode due to Cd-doping is investigated by RR evaluated from both diodes. The RR is found to reduce from 33.74 to 1.55 after Cd-doping. The trends have reduced in the results shown in Fig. 6.19, suggesting that both carrier densities have decreased, with the rate of decrease in density of majority carrier being higher rate.

6.1.2.2 *i*-Si

The ln(*I*)-*V* characteristics of undoped and Cd-doped *i*-Si diode is presented in Fig. 6.20 to study the change in trend due to Cd-doping. A linear region is observed at the low voltages but disappeared after 0.51 and 0.23 V for undoped and Cd-doped *i*-Si diode, respectively. The linear region in the forward characteristics of Cd-doped *i*-Si diode is smaller, suggesting that the Cd-induced defects affect the diode R_s.

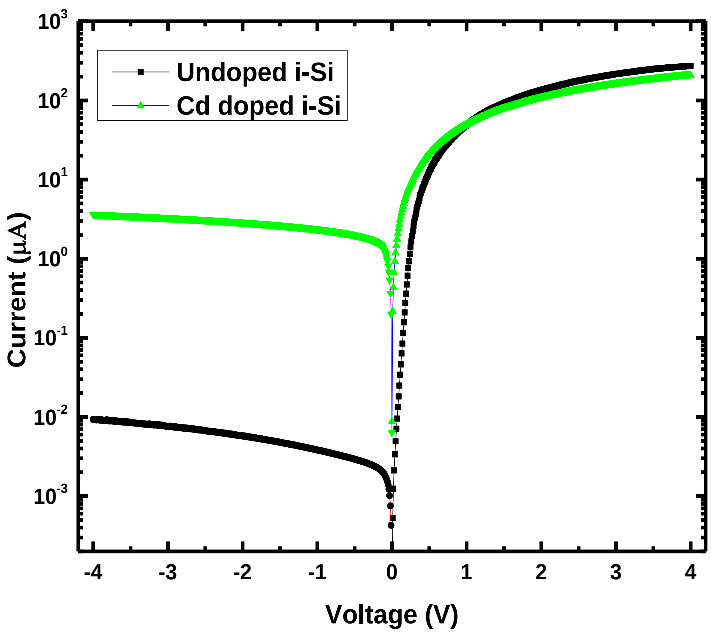

Fig. 6.20: *Forward and reverse bias ln(I)-V characteristics of diodes fabricated on undoped and Cd-doped i-Si.*

Fig. 6.20 shows that the reverse current increased by a factor of ~ 300 after Cd-doping, indicating a generation of minority carriers through Cd-induced defects. However, the forward current has reduced by a factor of ~ 4, indicating a recombination of majority carriers in the SCR. Figs. 6.21 (a) and (b) presents the plot of d*V*/dln(*I*) and *H(I)*-*I*, respectively. A linear region appears throughout the voltage region. The R_s, η and ϕ_B are evaluated from the linear region in Fig 6.21. The diode parameters evaluated from Figs. 6.20 and 6.21 are presented in Table 6.5.

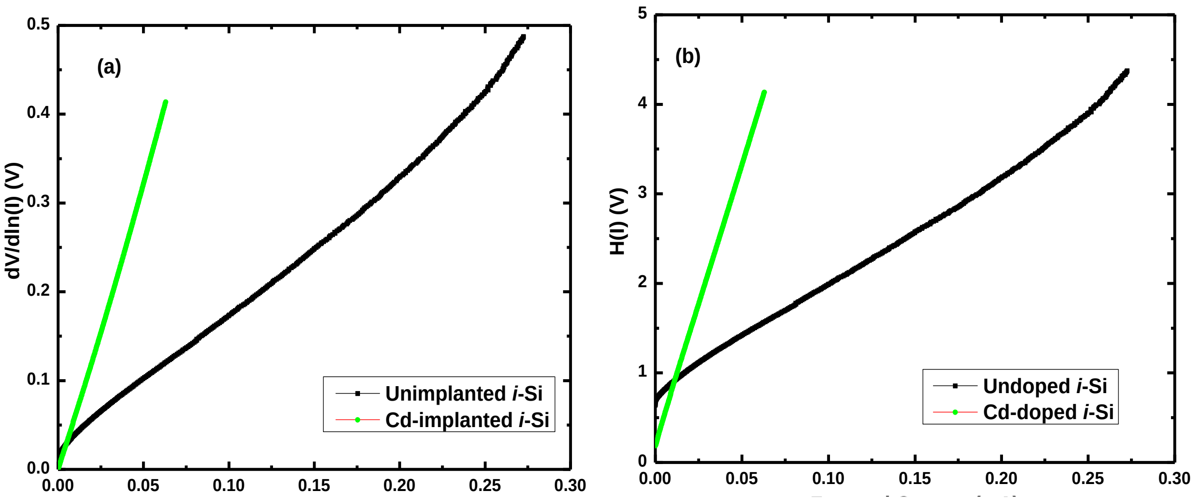

Fig. 6.21: *dV/dln(I)-I and H(I)-I plots on undoped (a) and Cd-doped (b) i-Si diodes.*

Fig. 6.22 presents the R_j-V plots for the diodes fabricated on the undoped and Cd-doped *i*-Si diode. The R_j trend is similar to the trend exhibited by the undoped *i*-Si but has reduced drastically, suggesting that charge carriers have been injected in SCR. The R_j in reverse bias of the Cd-doped *i*-Si with respect to undoped *i*-Si has decreased, confirming the generation of minority carriers due to Cd-induced defects. However, the R_j in forward bias increased, indicating the density of majority carriers has reduced as a result of recombination. The R_{sh} and R_s are obtained from Fig. 6.22 and are presented in Table 6.5.

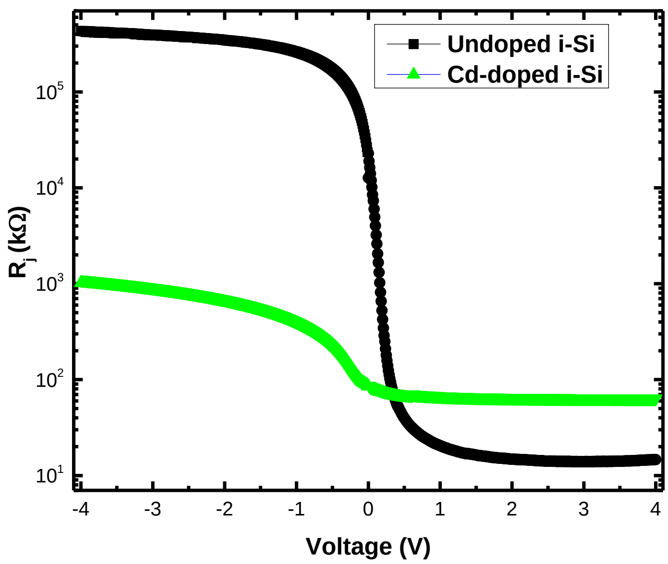

Fig. 6.22: *Diode resistances for undoped and Cd-doped i-Si diodes.*

The average of device parameters evaluated from ln*(I)-V*, d*V*/dln*(I)-I*, *H(I)-I, and* R_j-V plots for diodes fabricated on undoped and Cd-doped *i*-Si are presented in Table 6.5.

Table 6.5: Device parameters evaluated using different methods for diodes fabricated on undoped and Cd-doped *i*-Si.

	ln(*I)-V*			**d*V*/dln(*I*)-*I***		***H(I)-I***		***R**$_j$**-V***	
Diodes	η	I_s **(nA)**	ϕ_B **(eV)**	R_s **(kΩ)**	η	R_s **(k Ω)**	ϕ_B **(eV)**	R_{sh} **(MΩ)**	R_s **(k Ω)**
Undoped i-Si	1.65 ± 0.19	2.78 ± 0.97	0.78 ± 0.02	4.15 ± 1.28	1.54 ± 0.08	32.41 ± 12.39	0.66 ± 0.10	93.26 ± 17.94	34.93 ± 8.11
Cd-doped i-Si	4.81 ± 1.21	700.0 ± 208.0	0.63 ± 0.01	5.19 ± 0.91	1.06 ± 0.31	42.78 ± 11.19	0.60 ± 0.04	1.15 ± 0.04	38.06 ± 11.68

The evaluated η for Cd-doped *i*-Si diode evaluated using ln(*I*)-*V* method was found to be, 4.81, higher than 1.65 evaluated on undoped *i*-Si diode, indicating that other diode conduction mechanisms than TE and tunnelling mechanism have been introduced after Cd-doping. The evaluated η for the Cd-doped *i*-Si diode using d*V*/dln(*I)-I* method is 1.06, close to unity, indicating an ideal diode behaviour despite the trend in Fig. 6.20 showing otherwise. The η of unity evaluated using Cheung's method probably indicates that the parameter is less dependent on the defects induced in the material, hence, meaningless when the diode conduction mechanism is dominated by charge carrier distribution in the bulk.

The evaluated I_s increased from 2.78 to 700 nA after Cd-doping, confirming the generation of minority carriers as a result of the Cd-induced defects in *i*-Si. The ϕ_B values evaluated using different methods are found to decrease which agrees with the increase in I_s. The values of R_{sh} decreased after Cd-doping, indicating Cd generates minority carriers in Si while R_s increased after Cd-doping, indicating that Cd-induced defects recombines with majority carriers.

The double logarithmic *I-V* characteristics for the diodes fabricated on the Cd-doped *i*-Si were presented in Fig. 6.23. The forward current trend shows a single linear region with a slope of unity, indicating that the whole voltage region is completely ohmic. Furthermore, at low voltage region, (0-0.1 V) the reverse and forward current trend are the same, suggesting that the Cd-induced *g-r* centres are responsible for the ohmic region of the diode but the gap between the trends starts to widen at higher voltage of ~ 0.11 V, possibly because the densities of Cd-induced *g-r* centres are not enough to make $g = r$ for the entire voltage range.

A change in rectifying behaviour of a diode due to Cd-doping is investigated by RR evaluated from both diodes. The RR is found to reduce from 33470 to 17.94 after Cd-doping. As shown in Fig. 6.23, the reverse and forward current trends have increased and decreased, respectively, confirming the decrease in RR.

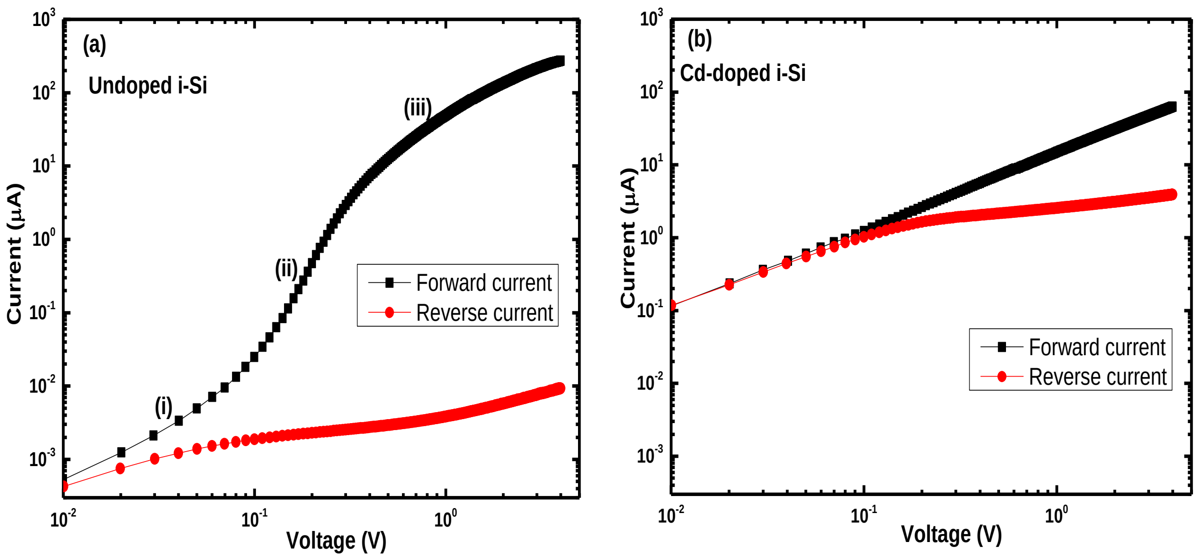

Fig. 6.23: *I-V characteristics of the diodes fabricated on undoped (a) and Cd-doped (b) i-Si in a double logarithmic scale.*

6.2 Capacitance-voltage (*C-V*) measurements

The *C-V* measurements were carried out to investigate the electrical properties of the fabricated diodes. The C^{-2}-V plots were presented to extract the diode parameters. The parameters extracted include the built-in potential (V_{bi}), doping concentration ($N_{D(A)}$) for *n*(*p*)-Si, Schottky barrier height (ϕ_B), and the depletion region width (W_D).

6.2.1 Fe-doped Si diodes

6.2.1.1 *n*-Si diodes

The *C-V* characteristics of the diode fabricated on undoped and *n*-Si doped with Fe different fluences are presented in Figs. 6.24 (a-d). As shown in Fig. 6.24 (a), the capacitance of undoped *n*-Si diode decreases with an increase in voltage as charge carriers are being withdrawn from the SCR. The drastic fall in capacitance observed at the low reverse voltage region indicates that the charge withdrawal rate is high at this region. Furthermore, an absence of saturation of the capacitance trend indicates a voltage higher than -2 V is needed to attain a full depletion of SCR for the undoped *n*-Si diode. The *C-V* trend exhibited by the undoped *n*-Si diode is similar to the typical *C-V* behaviour of a diode, confirming that our diode is well fabricated [19, 48-50] using Au as the Schottky contact. Thus, *C-V* measurements complement the data acquired using *I-V* measurements showing that the diodes are well fabricated.

Fig. 6.28 (b) presents the *C-V* characteristics of *n*-Si doped to a fluence of 10^{15} ion/cm^2. The *C-V* trend is similar to that of the undoped *n*-Si diode with the capacitance higher, indicating that the Fe-doping at this fluence generates charge carriers which in turn contributes to the measured capacitance. The capacitance tends to saturate at ~ 0.71 V, indicating that the SCR is fully depleted after Fe-doping to the fluence of 10^{15} ion/cm^2. It has been reported that a diode with high FDV results in a high level of noise during their operation as radiation detectors due to the high electric field in SCR [49-50]. At high FDV, the diode would operate at breakdown voltage or higher where the efficiency of the detector during operation is impossible [1, 50]. For a low FDV, on the other hand, the diode would operate at the voltage range lower than breakdown voltage [47-50]. Low FDV is important for devices because of a reasonable operating voltage for the device. Also, full depletion of SCR at low voltage results to a large SNR which is a good quality for detectors. Thus, the properties of the diode have been improved by doping the material with Fe to this fluence.

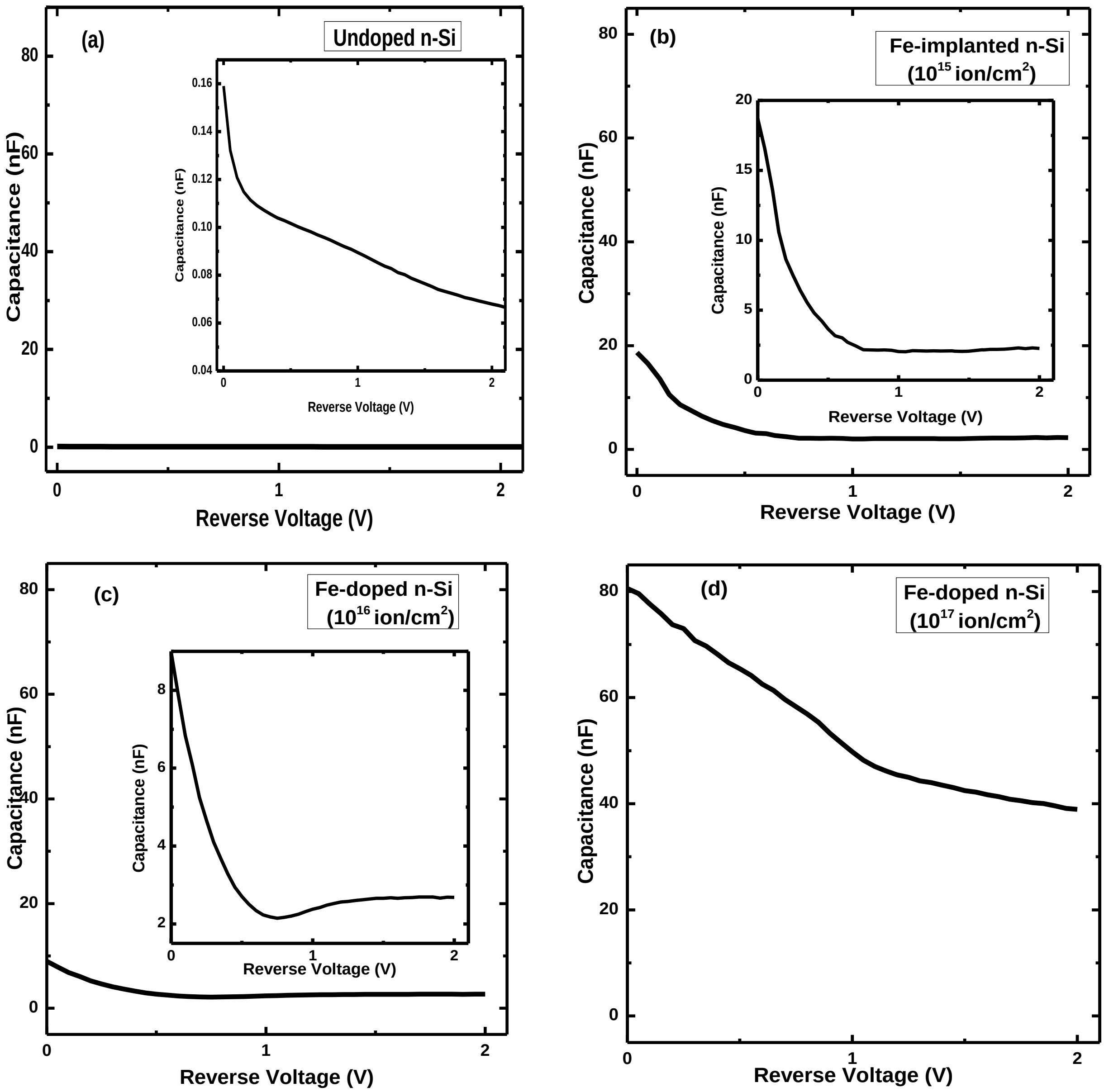

Fig. 6.24: *C–V characteristics of diodes fabricated on undoped n-Si (a), n-Si doped with Fe to a fluence of* 10^{15} *(b),* 10^{16} *(c), and* 10^{17} *(d) ion/cm*^{2}*.The inset are the rescaled C-V trend of diodes fabricated on undoped, Fe-doped n-Si to a fluence of* 10^{15} *and* 10^{16} *ion/cm*^{2}*.*

The *C-V* characteristics of the diode fabricated on *n*-Si doped to a fluence of 10^{16} ion/cm^2 is shown in Fig. 6.24 (c). The *C-V* trend is similar to that of the undoped *n*-Si diode with a higher capacitance, indicating that the Fe doping to the fluence of 10^{16} ion/cm^2 generates defects that increases the measured capacitance. The higher capacitance could be due to the high density of *g-r* centres generated at this fluence. It is to be noted that *I-V* measures charges across the junction while *C-V* measures the charges stored in the SCR. Furthermore, at ~ 0.51 V, the capacitance starts to saturate, indicating that full depletion of SCR has been attained after Fe-doping to the fluence of 10^{16} ion/cm^2. The low FDV observed at this fluence indicates that the active carriers in the SCR have reduced hence are fast to be withdrawn. The decrease in the density of active carriers indicates that the resistivity of the Si material has increased at this fluence. This is in agreement with high resistivity reported in the *I-V* results which shows that the density of *g-r* centres is the highest at this fluence, and they dominate the diode conduction mechanism.

Fig. 6.24 (d) shows the *C-V* characteristics of the diode fabricated on *n*-Si doped to a fluence of 10^{17} ion/cm^2. The rate of decrease in capacitance with reverse voltage have decreased compared to the rate of decrease observed on undoped *n*-Si diodes, indicating a slow ejection rate of charge carriers due to the high density of charge carriers generated by Fe-doping at this fluence. Furthermore, at ~ 1 V, the rate of decrease in capacitance decreased even further, but there was no saturation, indicating that a voltage higher than 2 V is required to achieve full depletion of the SCR.

The C^{-2}-V plots presented in Fig. 6.25 show the doping profile of the diodes fabricated on undoped and *n*-Si doped with Fe to different fluences. The trend of the plots observed on the undoped and *n*-Si doped with Fe diodes showed three linear regions, indicating a non-uniform doping profile. Two linear regions were identified on the plot of undoped *n*-Si diode in Fig. 6.25 (a). The first linear region observed at the low voltage region (0-0.19 V) is small due to the high density of charge carriers present at the metal-semiconductor interface contributing to the measured capacitance at this region. In this region, the SCR begins to move from metal-semiconductor interface into the semiconductor bulk. The second linear region is observed at the high voltage region (0.2-2 V), indicating that the doping profile is uniform over a large area of the SCR [51].

Three linear regions were identified on the C^{-2}-V plot of the diode fabricated on *n*-Si doped with Fe to the fluence of 10^{15} ion/cm^2 presented in Fig. 6.25 (b). The first region (0-0.22 V) is short with an infinitesimal slope, suggesting that the density of interface charges has increased, confirming that the defects introduced by doping with Fe at this fluence also affect the *m-s* interface. However, the second region (0.23-1.50 V) and a third region (1.51-2.0 V) are found in the high voltage region, suggesting that doping concentration is not uniform in the SCR.

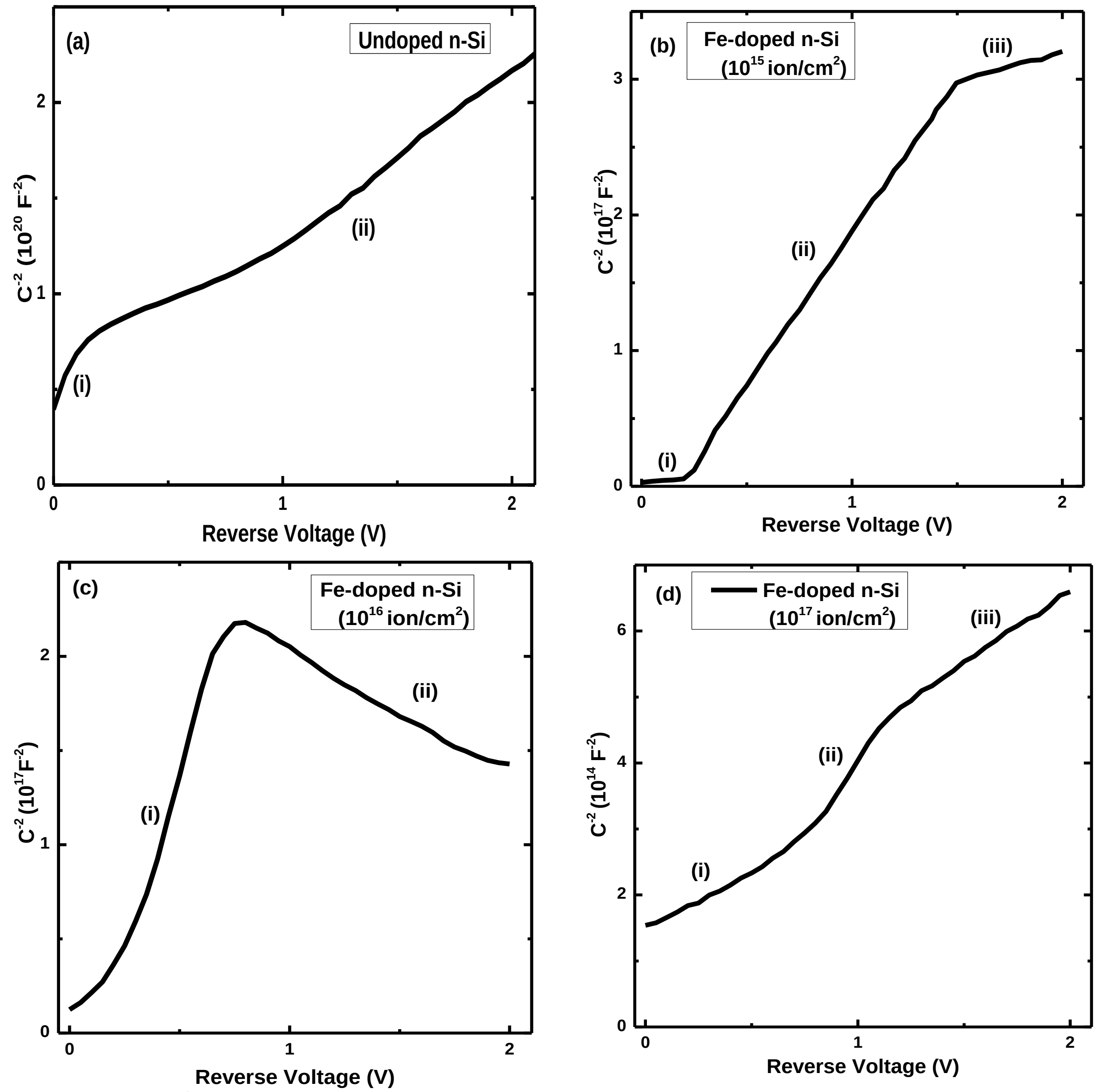

Fig. 6.25: *C^{-2}–V characteristics of diodes fabricated on undoped n-Si (a), Fe-doped n-Si to a fluence of 10^{15} (b), 10^{16} (c), and 10^{17} (d) ion/cm^2.*

Two linear regions were observed in the C^{-2}-V plot of diode fabricated on *n*-Si doped with Fe to the fluence of 10^{16} ion/cm^2 presented in Fig. 6.29 (c). The first linear region is observed at the low voltage region (0-0.76 V) and is the region at which the SCR begins to move from *m-s* interface into the semiconductor bulk. The second linear region (0.77-2 V) showed a negative slope, indicating that diode conduction at this region is dominated by minority carriers. A negative slope was also reported on Au doped *n*-Si [16] and proton-irradiated Si diode [52] and the negative slope was said to be as a result of minority carriers dominating the diode conduction. This work confirms that Fe doping to this fluence is responsible for a change in conductivity-type of the material by inducing defects that are responsible for the generation of holes, minority carriers in *n*-Si.

The C^{-2}-V plot of diode fabricated on *n*-Si doped by Fe to the fluence of 10^{17} ion/cm^2 is presented in Fig. 6.29 (d). Three linear regions were also observed, the first region was observed in the low voltage region, 0-0.82 V. The second and third regions were observed in the high voltage regions, 0.83-1.18 V and 1.19-2 V, respectively. The first linear region at the low voltage region is the region at which the SCR begins to move from metal-semiconductor interface into the semiconductor bulk.

The diode parameters such as V_{bi}, N_D, ϕ_B and W_D for the undoped and Fe-doped *n*-Si diodes are extracted from the linear regions of C^{-2}-V plot and presented in Table 6.6. The N_D evaluated from regions i and ii for the undoped *n*-Si diode are 0.007×10^{18} and 0.016×10^{18} cm^{-3}, these values are greater than 0.0007×10^{18} cm^{-3} reported on Au/*n*-Si diode [20] and lower than 0.5×10^{18} cm^{-3} reported on Al/OG/*n*-Si/AuSb diode [53]. Our value is within the range of values reported in the literature, indicating that the diode is well fabricated. The N_D increased after Fe-doping at all fluences in both regions, confirming that Fe induces defects that increase the density of charge carriers in Si as it penetrates the bulk.

Table 6.6: Diode parameters evaluated from C^{-2}-V plots for diodes fabricated on undoped and *n*-Si doped by Fe to different fluences.

Fluence (Fe/cm^2)	Region	V_{bi} (V)	N_D (10^{18} cm^{-3})	ϕ_B (eV)	W_D (10^{-6} cm)
0	**i**	0.22	0.007	0.43	20.7
	ii	0.37	0.016	0.57	18.0
15	**i**	0.23	117.00	0.19	0.17
	ii	0.17	6.64	0.13	0.62
	iii	4.32	29.50	4.32	1.38
16	**i**	0.09	4.43	0.14	0.59
	ii	4.07	22.60	4.08	0.15
17	**i**	1.21	10200.00	1.06	0.04
	ii	14.1	3200.00	13.9	0.24
	iii	1.00	68200.00	0.86	0.04

The value of ϕ_B evaluated from region ii of undoped *n*-Si diode is higher than those evaluated from region i, this is expected, since the evaluated N_D in region i is higher than that of region ii. The *n*-Si doped by Fe diodes followed the normal trend except the diode fabricated on *n*-Si doped by Fe to the fluence of 10^{15} ion/cm^2. Furthermore, ϕ_B is expected to decrease after Fe doping at all fluence due to the increase in N_D but the value obtained in region i increased after Fe-doping at all fluences. This discrepancy could be an indication that the ϕ_B is more of the surface property than bulk.

The value of W_D evaluated from the two regions are 20.7×10^{-6} and 18.0×10^{-6} cm, respectively. These values are close to 68.8×10^{-6} cm reported on Au/PVA (Bi-doped)/*n*-Si [8]. The value of W_D decreased after Fe-doping at all fluences corresponding to the increase in N_D.

6.2.1.2 *p*-Silicon diodes

The *C*-*V* characteristics of the diode fabricated on undoped and *p*-Si doped by Fe were shown in Fig. 6.26. As shown in Fig. 6.26 (a), the capacitance of the undoped *p*-Si diode decreases with voltage as charge carriers are being withdrawn from SCR. An absence of saturation indicates that more than 2 V is needed for the SCR to be fully depleted. The capacitance trend is similar to those that are presented in the literature to show that the diodes were well fabricated [18, 54] with Al as the Schottky contact.

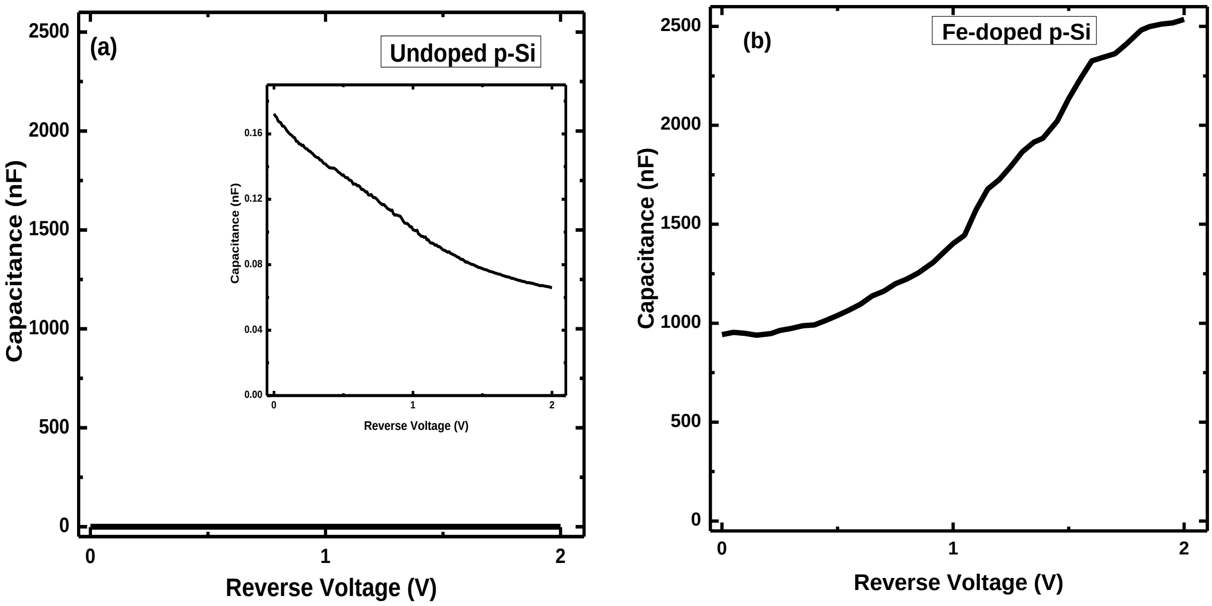

Fig. 6.26: *C–V characteristics of diodes fabricated on undoped (a) and Fe-doped p-Si (b) with a frequency of 5kHz.*

However, the *C-V* trend of *p*-Si doped by Fe diode shown in Fig. 6.26 (b) increased significantly, indicating that Fe generates high density of minority carriers in *p*-Si. Furthermore, an opposite *C-V* trend was observed, suggesting a conductivity-type inversion. A conductivity-type inversion was reported on the diodes that were fabricated on Pt-doped *n*-Si diodes [30-31] and on the neutron-irradiated diode [29, 55]. The measured capacitance increased rapidly after Fe-doping, confirming that Fe generates high density of charge carriers in *p*-Si. The observed increase in capacitance agrees with increase in conductivity reported in *I-V* results. An increase in capacitance was also reported on erbium-doped *p*-Si and was said to be due to the defect levels created in the upper half of Si band gap [51]. Thus, Fe creates defect levels in the upper half of Si band gap.

The C^{-2}-V plot for undoped and *p*-Si doped by Fe diode were presented in Fig. 6.27. Two linear regions were observed on the undoped *p*-Si diode presented in Fig. 6.27 (a), indicating a non-uniform doping profile. The first linear region was observed on the low voltage region (0-0.78

V), while the second linear region was observed on the high voltage region (0.79-2 V). The first linear region is smaller because at low voltage region, charges at the interface contributes to the measured capacitance.

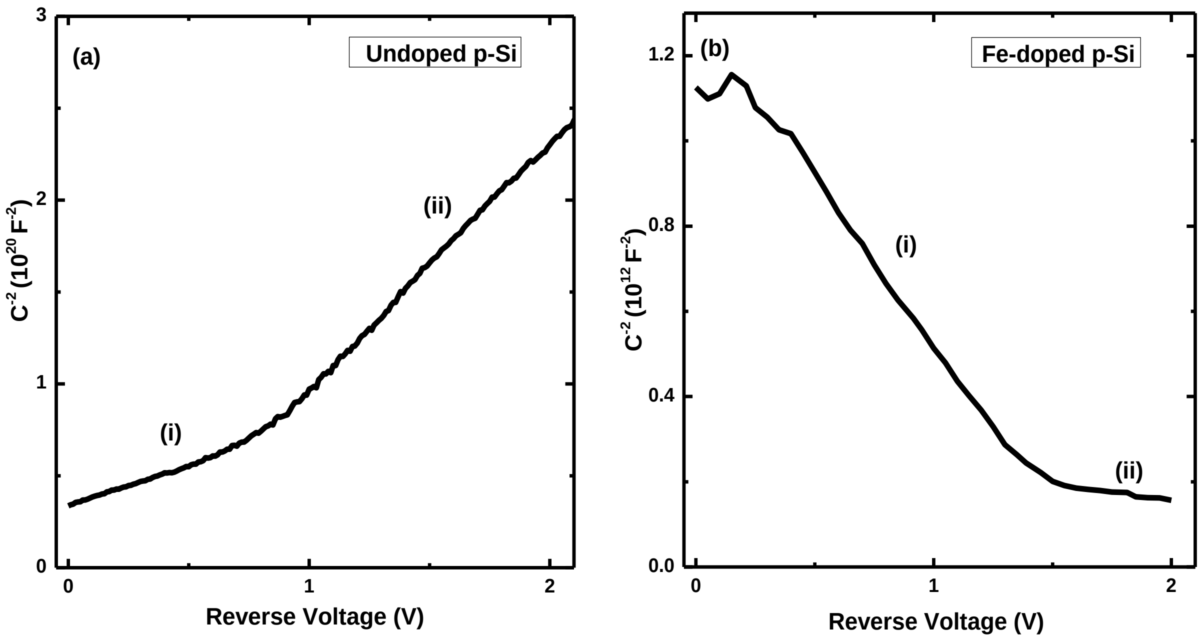

Fig. 6.27: *C^{-2}–V characteristics of diodes fabricated on undoped (a) and Fe-doped p-Si (b) with a frequency of 5kHz.*

As presented in Fig. 6.27 (b), the plot shows two linear regions for the Fe-doped *p*-Si diode, indicating a non-uniform doping profile. Unlike in the undoped *p*-Si diode, the second linear region is short because of the high density of charge carriers available in the SCR due to the Fe-induced defects. The opposite trend also confirmed the conductivity-type inversion mentioned earlier. The diode parameters such as V_{bi}, N_D, ϕ_B and W_D for the undoped and Fe-doped *p*-Si were extracted from the two linear regions and are presented in Table 6.7.

Table 6.7: Diode parameters evaluated from C^{-2}-V plots for diodes fabricated on undoped and Fe-doped *p*-Si.

***p*-Si diode**	**V_{bi} (V)**		**N_A (10^{18} cm^{-3})**		**ϕ_{cv} (eV)**		**W_D (10^{-6}cm)**	
	i	**ii**	**i**	**ii**	**i**	**ii**	**i**	**ii**
Undoped	0.65	0.50	0.03	0.01	0.80	0.68	17.10	19.30
Fe-doped	1.69	3.94	1970000	18700000	1.38	3.57	0.003	0.002

The value of N_D evaluated from regions i and ii on undoped *p*-Si diode are 0.03×10^{18} and 0.01×10^{18} cm^{-3}, respectively. These values are higher than 0.001×10^{18} cm^{-3} reported on Sn/*p*-Si diode [56] but close to 0.01×10^{18} cm^{-3} obtained on Au/*p*-Si diode [57]. Our value is within the range of those obtained in the reviewed literature [56-57], confirming that the diodes are well fabricated. Furthermore, the N_D evaluated from region i is higher than that of region ii because at low voltage region (region i), charges at the interface contributes to the measured capacitance.

The value of N_D increased in both regions after Fe doping confirming that Fe induces defects that generates charge carriers as it penetrates the Si material. This increase in N_D agrees with the increase in conductivity observed in *I-V* results after Fe-doping. A similar observation was also reported on neutron-irradiated Si *p-i-n* diodes [25]. Thus, the effects of Fe in Si are similar to that of radiation damage by 1 MeV neutrons.

The value of ϕ_B evaluated from regions i and ii on undoped *p*-Si diode are 0.80 and 0.68 eV, respectively. These values are within a range of those obtained in the reviewed literature [11, 51], confirming that our diodes are well fabricated. However, on Fe-doped *p*-Si diode, ϕ_B increased with N_D, which is contrary to the normal diode behaviour, but such observation has been reported on erbium doped *p*-Si diode [51]. This unusual trend shown by erbium was said to be due to erbium creating acceptors in the upper half of the band gap that increases the value of N_D so that the total N_D is higher and independent of ϕ_B. This trend suggests that Fe also creates acceptors in the upper half of the band gap of Si.

The value of ϕ_B evaluated from region i is higher than that evaluated from region ii for the undoped *p*-Si diode. Although it is expected that ϕ_B from region ii should be higher since the N_D evaluated at this region is lower. This discrepancy could indicate that the ϕ_B is more of the surface property than bulk. A conjecture of the parameter being more surface property is confirmed by unreasonably high ϕ_B evaluated on the linear regions, especially at region ii for the *p*-Si doped by Fe diode. These ϕ_B may also indicate that the parameter is meaningless for a diode fabricated on a material rich of defects positioned at the centre of the band gap.

The evaluated W_D from regions i and ii of undoped *p*-Si diode are 17.1×10^{-6} and 1.93×10^{-6} cm, respectively. These values are lower than 118×10^{-6} cm reported on Au/*n*-si [8] and higher than 1.77×10^{-6} cm reported on Au/pyronin-Y/*p*-Si/Al [18], indicating that our value is within the range of values reported in the reviewed literature [8, 18]. The W_D decreased after Fe-doping, confirming the generation of charge carriers in the SCR as a result of Fe-induced defects.

6.2.1.3 *i*-Silicon diodes

The *C-V* characteristics of the diode fabricated on undoped and *i*-Si doped by Fe were presented in Fig. 6.28. As shown in Fig. 6.28 (a), the capacitance of the undoped *i*-Si diode increased linearly at low voltage due to the presence of interface charges following the ac signal [54]. At 0.30 V, the capacitance starts to decrease rapidly with applied voltage, suggesting that the region has moved to the SCR and charge carriers are being withdrawn out of SCR. The capacitance completely saturates after 0.79 V, indicating a full depletion of SCR. This is typical behaviour of a diode confirming that our device is well fabricated [16].

Fig. 6.28 (b) presents the *C-V* trend of Fe-doped *i*-Si diode. The general capacitance has increased, indicating that Fe generates charge carriers in *i*-Si material. Furthermore, there was no trend of saturation of capacitance at high voltage, suggesting that a voltage higher than 2 V is needed to attain full depletion of SCR. The trend of capacitance observed in Fig. 6.28 (b) is opposite of Fig. 6.28 (a), indicating the conduction in Fe-doped *i*-Si diode is now dominated by minority carriers.

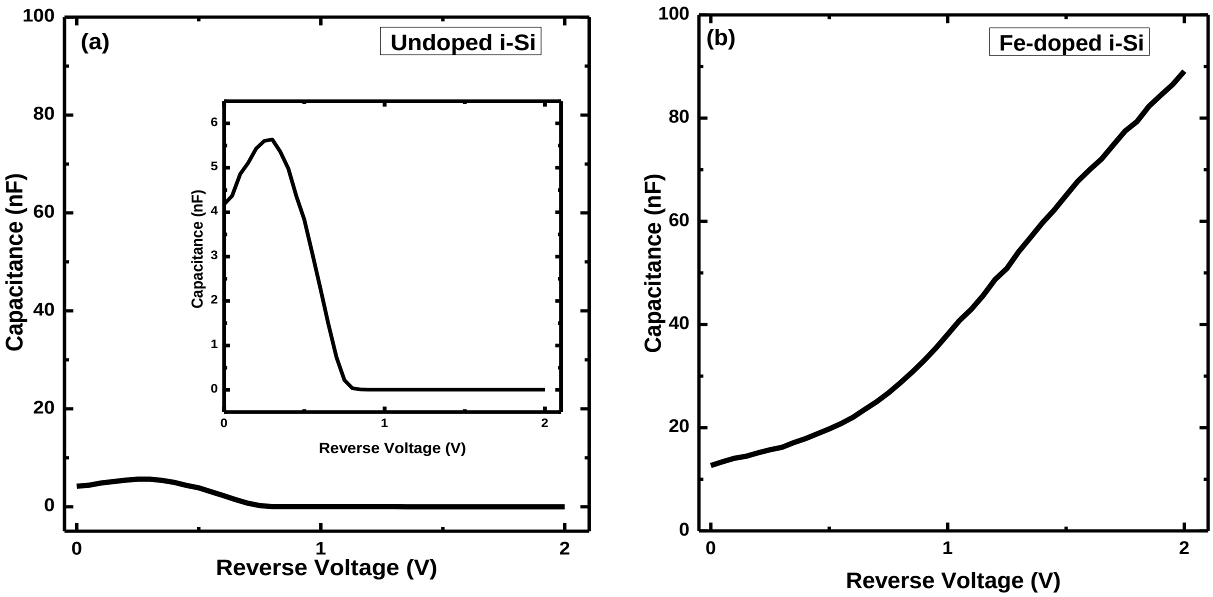

Fig. 6.28: *C–V characteristics of diodes fabricated on undoped (a) and Fe-doped (b) i-Si with a frequency of 5kHz.*

The C^{-2}-V plots for undoped and Fe-doped *i*-Si diodes are presented in Fig. 6.29. Two linear regions were observed in Fig. 6.29 (a) and (b). However, unlike the undoped *i*-Si diode, the regions on the Fe-doped *i*-Si diode have a negative slope, suggesting that the diode conduction is dominated by minority carriers. The *C-V* parameters such as V_{bi}, N_{D}, ϕ_{B}, and W_{D} are extracted from these linear regions and presented in Table 6.8.

Table 6.8: Diode parameters evaluated from C^{-2}-V plots for diodes fabricated on undoped and Fe-doped *i*-Si.

***i*-Si diode**	V_{bi} **(V)**		N_{D} **(10^{15} cm^{-3})**		ϕ_{B} **(eV)**		W_{D} **(10^{-5} cm)**	
	i	**ii**	**i**	**ii**	**i**	**ii**	**i**	**ii**
Undoped	0.25	0.23	4.40	0.01	0.48	0.61	2.85	48.0
Fe-doped	1.03	2.10	281000	3000000	0.97	1.97	0.02	0.01

The evaluated N_{D} from regions i and ii on the undoped *i*-Si diode are 4.40×10^{15} and 0.01×10^{15} cm^{-3}. The value obtained from region i is greater than 0.71×10^{15} cm^{-3} reported on Au/*n*-Si diode [16] and lower than 0.5×10^{15} cm^{-3} reported on Ni/*p*-Si diode [58]. The value obtained from region ii is lower than the ones reported in the reviewed literatures [16, 58], possibly due to a low thickness of the Au-Si interface formed. N_{D} increased in both regions after Fe-doping, confirming that Fe introduces charge carriers at the interface and in the SCR. The evaluated parameters are similar to *n*-Si diode and the effect of Fe-doping is expected to be the same since Au is used as a Schottky contact in both diodes.

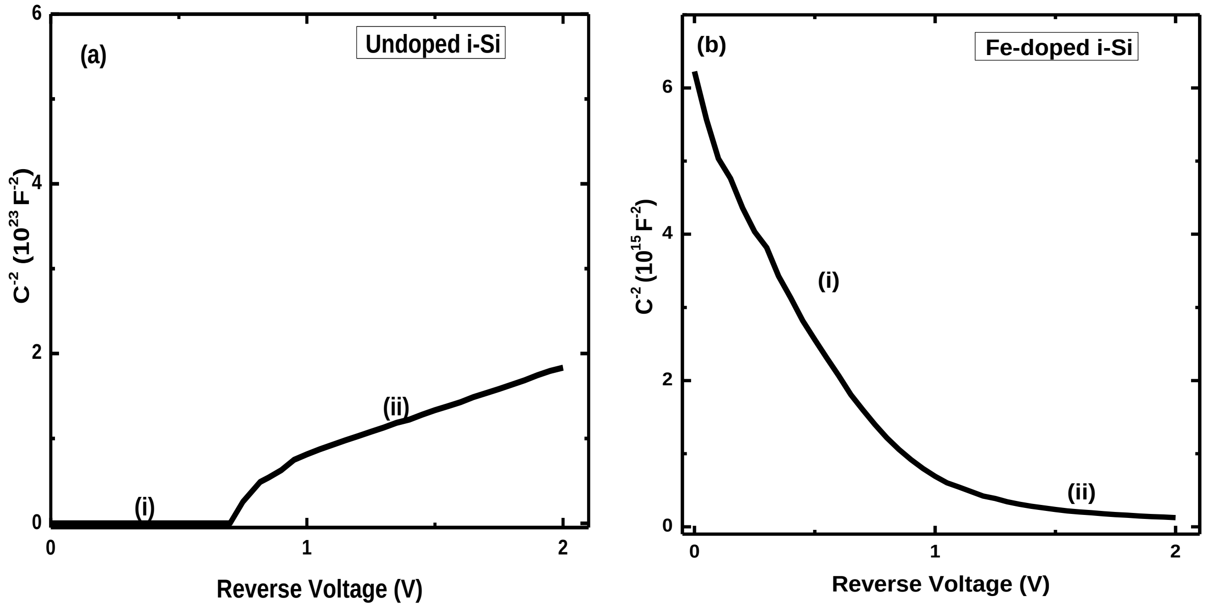

Fig. 6.29: *The C^{-2}–V characteristics of diodes fabricated on undoped (a) and Fe-doped (b) i-Si with a frequency of 5kHz.*

6.2.2. Effects of Cd dopant

6.2.2.1 *p*-Si diodes

The *C-V* characteristics of the diode fabricated on undoped and Cd-doped *p*-Si are presented in Fig. 6.30. The capacitance trend exhibited by the Cd-doped *p*-Si diode is opposite of the undoped *p*-Si diode, indicating a conductivity-type inversion. Also, the capacitance has decreased after Cd-doping, indicating the density of charge carriers has reduced in the SCR due to recombination of charge carriers by Cd-induced defects.

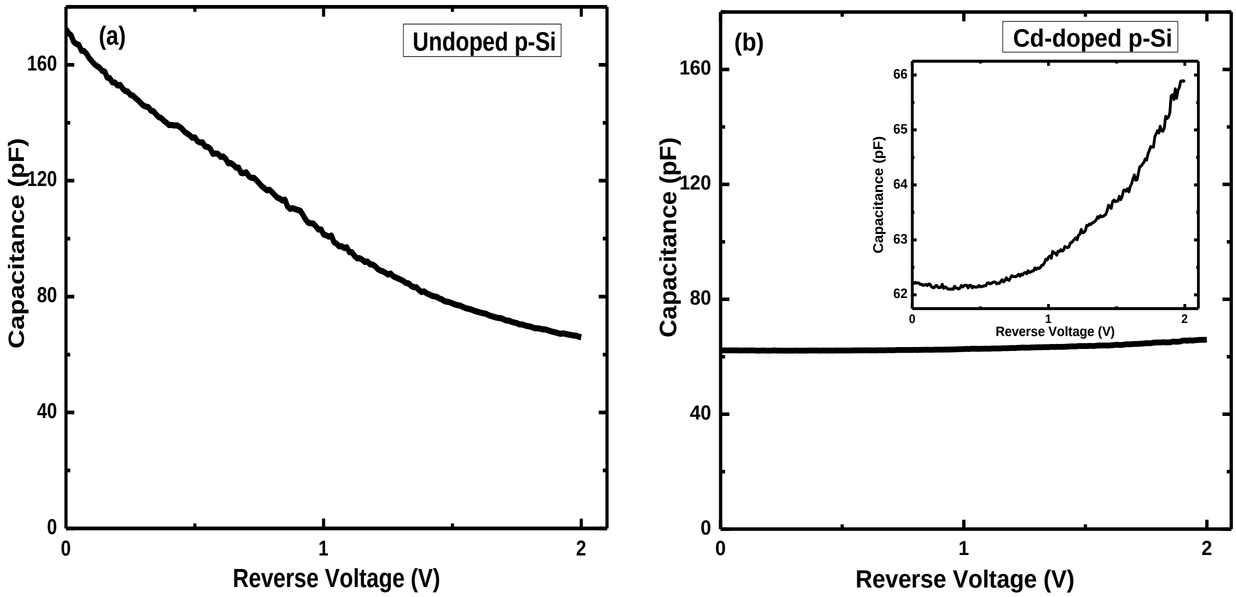

Fig. 6.30: *C–V characteristics of diodes fabricated on undoped (a) and Cd-doped p-Si (b) with a frequency of 5kHz.*

The first linear region of C^{-2}-V plot has increased after Cd-doping to show that as it penetrates the bulk, Cd induces defects from the surface. These defects recombine with the interface charges resulting in a decrease in the N_D. A decrease in N_D as shown by high C^{-2} at a low reverse voltage range indicates that as they are generated by Cd-induced defects, minority carriers recombine with majority carriers, resulting in a decrease in charge carrier density in SCR. At a high reverse voltage range a slope of C^{-2}-V plot in Fig. 6.31 (b) is opposite from that observed in Fig. 6.31 (a), confirming that at this region, the diode conduction is dominated by minority carriers after Cd-doping. The diode parameters such as V_{bi}, N_D, ϕ_B and W_D are calculated from the C^{-2}-V plots and presented in Table 6.9.

Table 6.9: Diode parameters evaluated from C^{-2}-V plots for diodes fabricated on undoped and Cd-doped *p*-Si.

***p*-Si diode**	**V_{bi} (V)**		**N_A (10^{16} cm^{-3})**		**ϕ_{cv} (eV)**		**W_D (10^{-5} cm)**	
	i	**ii**	**i**	**ii**	**i**	**ii**	**i**	**ii**
Undoped	0.65	0.50	3.11	1.10	0.80	0.68	1.71	1.93
Cd-doped	10.40	2.41	0.57	0.39	10.80	2.81	322	396

The N_D decreased in Cd-doped diodes reaffirming that Cd induces defects that recombine with charge carriers in Si. This decrease agrees with the increase in resistivity observed in *I-V* results after Cd-doping. A decrease in N_D was also reported on Au- and Pt-doped *p*-Si diodes [51] and gamma-irradiated Si diodes [50]. The decrease was said to be due to the induced defects that recombine with charge carriers. Given this, Cd-doping has a similar effect in Si to gamma-irradiation and doping Si with metals like Au and Pt. The ϕ_B and W_D increased after Cd-doping confirming the recombination of charge carriers in the SCR.

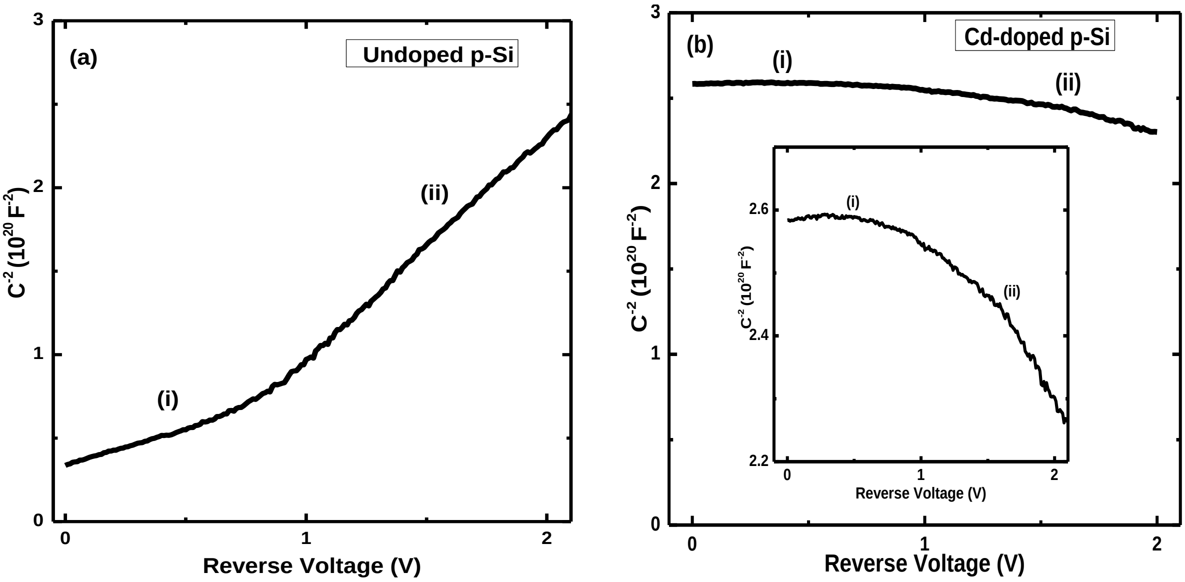

Fig. 6.31: *C^{-2}–V characteristics of diodes fabricated on undoped (a) and Cd-doped (b) p-Si with a frequency of 5kHz.*

6.2.2.2 *i*-Si diodes

The *C-V* characteristics of the diode fabricated on undoped and Cd-doped *i*-Si was shown in Fig. 6.32. The capacitance of the Cd-doped *i*-Si diode decreased rapidly at low voltage region (0-1 V), indicating a high rate of charge withdrawal at this region. In comparison with undoped *i*-Si diode, the capacitance has increased, suggesting that more charge carriers are being generated due to the Cd-induced defects. At ~ 1 V, the capacitance starts to saturate, indicating a full depletion of SCR. The FDV has increased due to the increased numbers of charge carriers available in the SCR as a result of the Cd-induced defects.

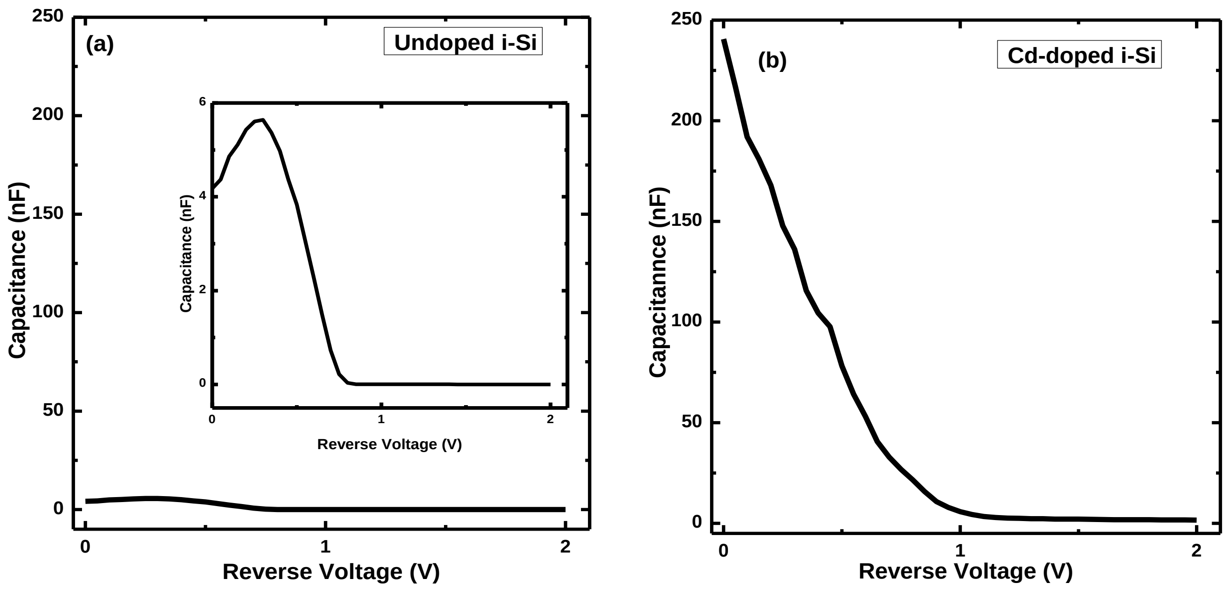

Fig. 6.32: *C–V characteristics of diodes fabricated on undoped (a) and Cd-doped (b) i-Si with a frequency of 5kHz.*

The C^{-2}-V plots for unimplanted and Cd-implanted *i*-Si diodes are presented in Fig. 6.33. The trend of the C^{-2}-V plot shows two linear regions, indicating a non-uniform doping profile. The first linear region is in the low voltage region, the region is the region at which the SCR begins to move from metal-semiconductor interface to the semiconductor bulk. The second linear region represents the SCR, and the doping concentration is uniform in SCR.

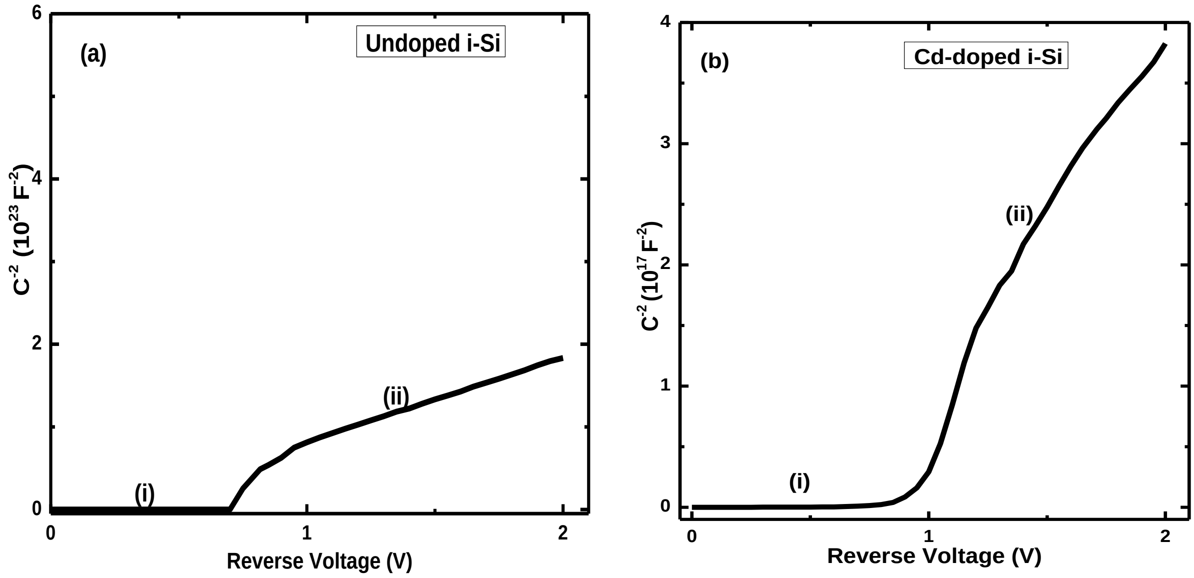

Fig. 6.33: *The C^{-2}–V characteristics of diodes fabricated on undoped (a) and Cd-doped (b) i-Si with a frequency of 5kHz.*

The *C*-*V* parameters are extracted from the two regions and presented in Table 6.10. The evaluated N_D increased after Cd-doping confirming that Cd-induced defects generate carriers in *i*-Si material. As expected, the decrease in W_D corresponds to the increase in N_D after Cd-doping, confirming the generation of carriers in the *i*-Si material.

Table 6.10: Diode parameters evaluated from C^{-2}-V plots for diodes fabricated on undoped and Cd-doped *i*-Si.

***i*-Si diode**	V_{bi} **(V)**		N_D **(10^{15} cm^{-3})**		ϕ_B **(eV)**		W_D **(10^{-5} cm)**	
	i	**ii**	**i**	**ii**	**i**	**ii**	**i**	**ii**
Undoped	0.25	0.23	4.40	0.01	0.48	0.61	2.85	48.0
Cd-doped	0.25	0.80	306000	445000	0.19	0.74	0.02	0.01

References

[1] E. H. Rhoderick and E. H. Rhoderick, Metal-semiconductor contacts, *Clarendon Press*, Oxford, 1978.

[2] S. M. Sze, Physics of Semiconductor Devices, *Wiley*, New York, 1981.

[3] M. Msimanga, M. McPherson, and C. Theron, *Radiat. Phys. Chem.*, **71** (2004) 733.

[4] S. M. Sze, Semiconductor devices: physics and technology, *Wiley,* NewYork, 2008.

[5] A. A. M. Farag, B. Gunduz, F. Yakuphanoglu, and W. A. Farooq, *Synth. Met.*, **160** (2010) 2559.

[6] Ö. Güllü, M. Çankaya, M. Biber, and A. Türüt, *J. Phys. D. Appl. Phys.*, **41** (2008) 135103.

[7] S. K. Cheung and N. W. Cheung, *Appl. Phys. Lett.*, **49** (1986) 85.

[8] S. Alialy, H. Tecimer, H. Uslu, and Ş. Altındal, *J Nanomed Nanotechol*, **4** (2013) 1000167.

[9] İ. Taşçıoğlu, U. Aydemir, Ş. Altındal, B. Kınacı, and S. Özçelik, *J. Appl. Phys.*, **109** (2011) 54502.

[10] H. S. Soliman, A. A. M. Farag, N. M. Khosifan, and T. S. Solami, *J. Alloys Compd.*, **530** (2012) 157.

[11] I. Dökme and Ş. Altindal, *Semicond. Sci. Technol.*, **21** (2006) 1053.

[12] Ö. F. Bakkaloğlu, K. Ejderha, H. Efeoğlu, Ş. Karataş, and A. Türüt, *Silicon*, **1** (2021) 1.

[13] M. J. Thebe, S. J. Moloi, and M. Msimanga, *Mater. Sci. Eng. B,* **273** (2021) 115392.

[14] S. Amor, A. Ahaitouf, A. Ahaitouf, J. P. Salvestrini, and A. Ougazzaden, *IOP Conf. Series: Mate. Sci. Eng.*, **186** (2017) 12001.

[15] Q. K. Yang, F. Fuchs, J. Schmitz, and W. Pletschen, *Appl. Phys. Lett.*, **81** (2002) 4757.

[16] M. Msimanga and M. McPherson, *Mater. Sci. Eng. B,* **127** (2006) 47.

[17] S. Mahato and J. Puigdollers, *Phys. B Condens. Matter*, **530** (2018) 327.

[18] S. J. Moloi, and M. McPherson. *Phys. B: Condens. Matter* **404** (2009) 3922.

[19] P. G. Litovchenko, A. A. Groza, V. F. Lastovetsky, L. I. Barabash, *et al. Nucl. Instr. Meth. Phys. Res. Sect. A Accel. Spect., Detect. Assoc. Equip.*, **568** (2006) 78.

[20] I. S. Yahia, H. Y. Zahran, F. H. Alamri, M. A. Manthrammel, S. AlFaify, and A. M. Ali, *Phys. B Condens. Matter,* **543** (2018) 46.

[21] Q. K. Yang, F. Fuchs, J. Schmitz, and W. Pletschen, *Appl. Phys. Lett.*, **81** (2002) 4757.

[22] L. D. Rao and V. R. Reddy, *AIP Conf. Proceed.*, **1731** (2016) 120020.

[23] I. Missoum, Y. S. Ocak, M. Benhaliliba, C. E. Benouis, and A. Chaker, *Synth. Met.*, **214** (2016) 76.

[24] A. Kaya, E. Marıl, Ş. Altındal, and İ. Uslu, *Microelectron. Eng.*, **149** (2016) 166.

[25] S. J. Moloi and M. McPherson, *Nucl. Instr. Meth. Phys. Res. Sect. B Beam Interact. with Mater. Atoms*, **440** (2019) 64.

[26] M. McPherson, T. Sloan, and B. K. Jones, *J. Phys. D. Appl. Phys.*, **30** (1997) 3028.

[27] B. K. Jones, J. Santana, and M. McPherson, *Solid State Commun.*, **105** (1997) 547,

[28] V. N. Brudnyi, S. N. Grinyaev, and V. E. Stepanov, *Phys. B Condens. Matter*, **212** (1995) 429.

[29] B. K. Jones and M. McPherson, *Semicond. Sci. Technol.*, **14** (1999) 667.

[30] M. Moll, J. Adey, A. Al-Ajili *et al.*, *Nucl. Instr. Meth. Phys. Res. Sect. A Accel. Spect., Detect. Assoc. Equip.*, **546** (2005) 99.

[31] M. K. Parida, S. T. Sundari, V. Sathiamoorthy, and S. Sivakumar, *Nucl. Instr. Meth. Phys. Res. Sect. A Accel. Spect., Detect. Assoc. Equip.*, **905** (2018) 129.

[32] I. W. Anokhin, A. B. Rosenfeld, and O. S. Zinets, *Radiat. Prot. Dosimetry*, **101** (2002) 107.

[33] Y. K. Kwon, T. Ishikawa, and H. Kuwano, *J. Appl. Phys.*, **61** (1987) 1055.

[34] H. Carchano and C. Jund, *Solid. State. Electron.*, **13** (1970) 83.

[35] H. Tanaka, T. Isogai, T. Goto, A. Teramoto, S. Sugawa, and T. Ohmi, *Jpn. J. Appl. Phys.*, **49** (2010) 04DA03.

[36] R. T. Tung, *Phys. Rev. B*, **45** (1992) 13509.

[37] Ş. Aydoğan, M. Sağlam, and A. Türüt, *Microelectron. Eng.*, **85** (2008) 278.

[38] Ö. Güllü, Ş. Aydoğan, M. Biber, and A. Türüt, *Vacuum*, **82** (2008) 1264.

[39] S. R. Forrest and P. H. Schmidt, *J. Appl. Phys.*, **59** (1986) 513.

[40] Ö. Güllü, M. Çankaya, M. Biber, and A. Türüt, *J. Phys. D. Appl. Phys.*, **41** (2008) 13.

[41] S. J. Moloi, and M. McPherson. *Phys. B: Condens. Matter* **404** (2009) 2251.

[42] M. Sağlam, D. Korucu, and A. Türüt, *Polymer (Guildf).*, **45** (2004) 7335.

[43] Y. S. Ocak, M. Kulakci, T. Kılıçoğlu, R. Turan, and K. Akkılıç, *Synth. Met.*, **159** (2009) 1603.

[44] İ. Dökme, T. Tunç, İ. Uslu, and Ş. Altındal, *Synth. Met.*, **161** (2011) 474.

[45] H. Çulcu, M. Gökçen, A. Allı, and S. Allı, *J. Phys. Chem. Solids*, **103** (2017) 197.

[46] Ö. Güllü, F. Demir, F. E. Cimilli, and M. Biber, *Vacuum*, **82** (2008) 789.

[47] G. Lutz, Semiconductor radiation detectors, *Springer*, Heidelberg, 2007.

[48] L. Rajan, C. Periasamy, and V. Sahula, *Perspect. Sci.*, **8** (2016) 66.

[49] C. Morosanu *et al.*, *J. Non. Cryst. Solids*, **164** (1993) 8.

[50] D. K. Schroder, Semiconductor material and device characterization, *Wiley*, NewYork, 2015.

[51] S. J. Moloi and M. McPherson, *Radiat. Phys. Chem.*, **85** (2013) 3.

[52] G. Casse, P. P. Allport, and M. Hanlon, *IEEE Trans. Nucl. Sci.*, **47** (2000) 527.

[53] Ö. Güllü, Ş. Aydoğan, and A. Türüt, *Microelectron. Eng.*, **85** (2008) 1647.

[54] B. Şahin, H. Çetin, and E. Ayyildiz, *Solid State Commun.*, **135** (2005) 490.

[55] D. Pitzl *et al.*, "Type inversion in silicon detectors," *Nucl. Instr. Meth. Phys. Res. Sect. A Accel. Spect., Detect. Assoc. Equip.*, **311** (1992) 98.

[56] Ö. Güllü, F. Demir, F. E. Cimilli, and M. Biber, *Vacuum*, **82** (2008) 1647.

[57] M. A. Yeganeh and S. H. Rahmatollahpur, *J. Semicond.*, **31** (2010) 74001.

[58] R. Kumar and S. Chand, *Solid State Sci.*, **58** (2016) 115.

Chapter 7

I-V characteristics of 4 MeV proton-irradiated Si diodes

This chapter presents and analyses the effect of proton-irradiation on the fabricated diodes to establish the radiation-hardness of fabricated devices. *I-V* measurements were performed on the unirradiated and irradiated Si diodes.

7.1 Undoped and Fe-doped *n*-Si diodes

Figs. 7.1 (a-d) show ln(*I*)-*V* characteristics of diode fabricated on undoped and Fe-doped *n*-Si prior to and after proton-irradiation to the fluence of 10^{16} ion/cm^2. The ln(*I*)-*V* plot of the undoped *n*-Si diode was presented in Fig. 7.1 (a). The forward current for both diodes increases linearly at low voltage and deviates from linearity at high voltage, indicating the presence of R_s at the high voltage region [1]. After irradiation, the reverse current remained unchanged, indicating that irradiation does not affect the minority carriers. However, the forward current of the diode decreased by a factor of ~ 10^3, indicating that there is a recombination of majority carriers (electrons) due to the defects induced by proton-irradiation. This observation agrees with literature, where a decrease in the current was reported on diode irradiated with γ-particles [2-3]. These results can be explained in terms of radiation-induced defect centres that act as trapping or recombination centres to reduce the density of free charge carriers and hence the measured current [4-7].

The ln(*I*)-*V* characteristics of the diode fabricated on Fe-doped *n*-Si to the fluence of 10^{15} ion/cm^2 is shown in Fig. 7.1 (b), the reverse current decreased by a factor of ~ 10 after proton-irradiation, indicating that the diode is sensitive to radiation. However, the change in forward current is negligible, indicating that proton-irradiation has a negligible effect on the majority carriers. This trend confirms that the effect of irradiation on the forward current has been suppressed. The effect of irradiation was found to be suppressed on Au-doped Si material [4] and the suppression effect was said to be as a result of the *g-r* centres already present due to Au-doping somewhat hinders the formation of any additional defect levels by proton-irradiation.

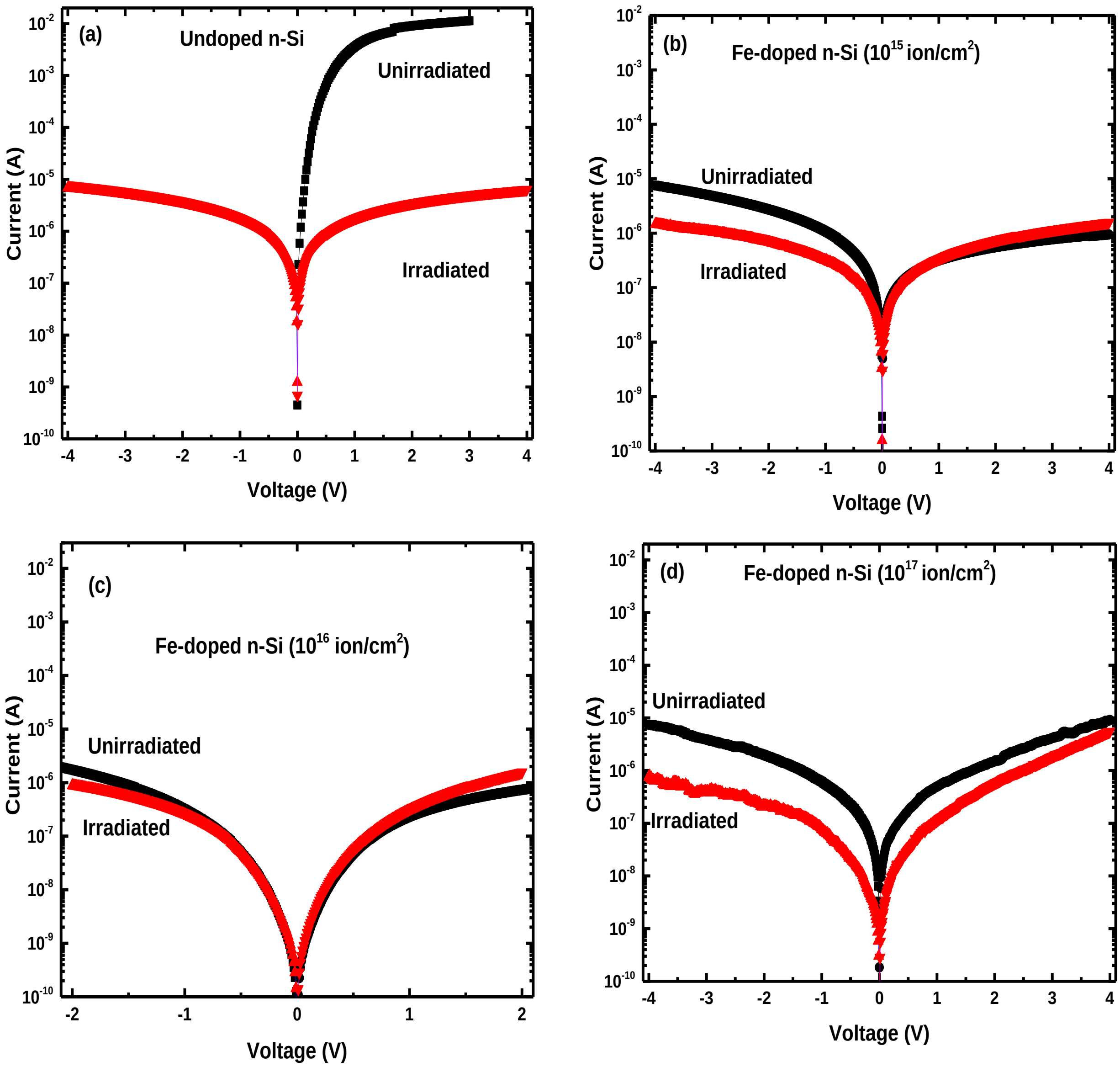

Fig. 7.1: *ln(I)-V characteristics of the diodes fabricated on undoped (a), Fe-doped n-Si to the fluence 10^{15} (b), 10^{16} (c), and 10^{17} (d) ion/cm^2 prior to and after proton-irradiation.*

The *I-V* characteristics of the diode fabricated on Fe-doped *n*-Si to the fluence of 10^{16} ion/cm^2 is shown in Fig. 7.1 (c), the trends of the reverse current reduced by a factor of ~ 1.92 and the forward current increased by a factor of ~ 2 after proton irradiation, indicating that the effect of irradiation is suppressed in the diode. For this diode, the effects of radiation are suppressed in both reverse and forward bias.

Fig. 7.1 (d) shows the *I-V* characteristics of the diode fabricated on Fe-doped *n*-Si to the fluence of 10^{17} ion/cm^2. After irradiation, the reverse and forward current trend was reduced by a factor of ~9 and 1.74, respectively. The decrease in reverse current suggests that the diode is sensitive to irradiation while the small decrease in forward current suggests that the effect of irradiation on forward current has been suppressed.

7.2 Undoped and Fe-doped *p*-Si diodes

Fig. 7.2 shows ln*(I)-V* characteristics of undoped and Fe-doped *p*-Si diodes prior to irradiation and after irradiation in a semilogarithmic scale. Fig. 7.2 (a) shows the ln*(I)-V* plot of undoped *p*-Si diode. After irradiation, the forward current and the reverse current of the diode decreased by a factor of ~ 12 and 31, respectively. A decrease in both current trends indicate recombination of majority and minority charge carriers (electrons and holes) leading to a low charge carrier density in the SCR because of the defects induced by proton-irradiation. This observation agrees with the reviewed literature, where a decrease in the current trends was reported on diode irradiated with γ-particles [2-3]. These results can be explained in terms of radiation-induced defect centres that act as trapping or recombination centres to reduce the density of free charge carrier and hence the measured current [4-7].

Fig.7.2 (b) present the *I-V* characteristics of Fe-doped *p*-Si diodes prior to irradiation and after irradiation on a semilogarithmic scale. The reverse and forward current decreased by a factor of ~1.6 and 2.5, respectively. The rate of decrease in the trends has decreased confirming that the radiation effect has been suppressed. This observation shows that Fe supresses the effect of radiation in Si.

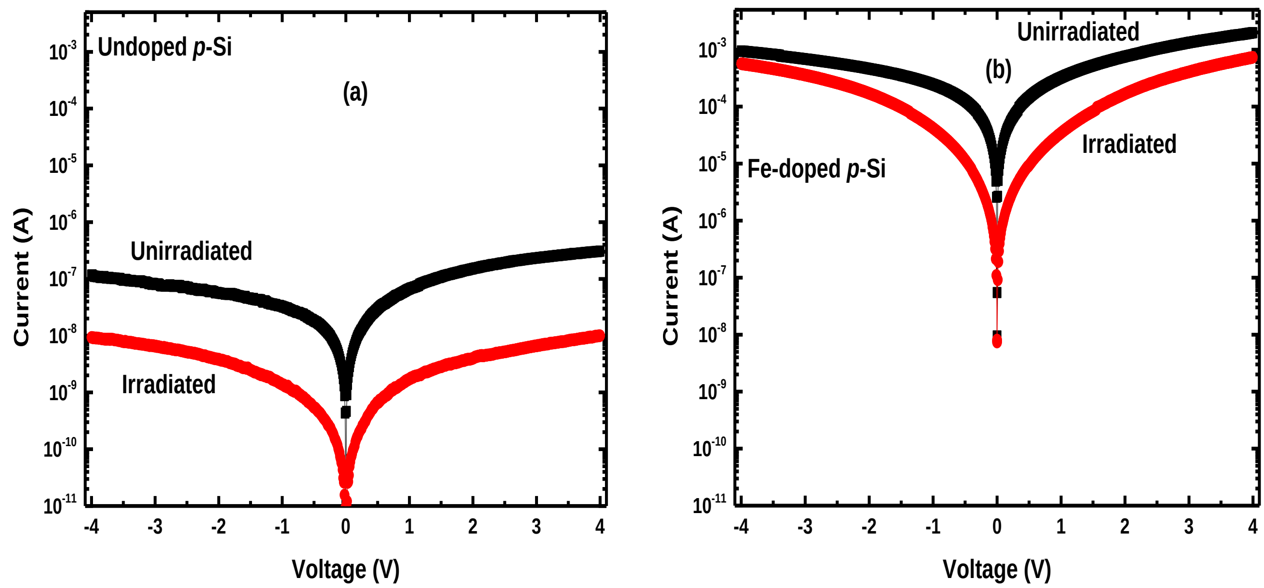

Fig. 7.2: *ln(I)-V characteristics of the diodes fabricated on undoped (a) and Fe-doped (b) p-Si prior to irradiation and after irradiation.*

7.3 undoped and Cd-doped diodes

Fig. 7.3 (b) present the *I-V* characteristics of Cd-doped *p*-Si diodes prior to irradiation and after irradiation on a semilogarithmic scale. The reverse and forward current decreased by a factor of ~1.6 and 2.5, respectively. The rate of decrease in the trends has decreased, confirming that the radiation effect has been suppressed. For this diode, the effects of radiation are suppressed in both reverse and forward bias.

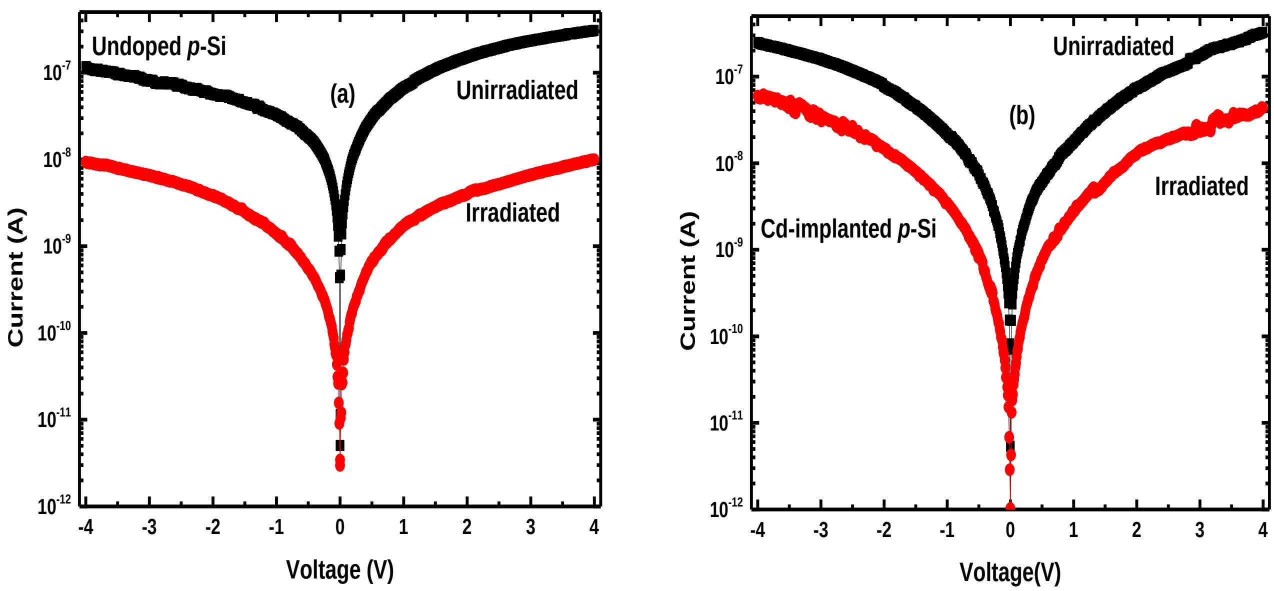

Fig. 7.3: *ln(I)-V characteristics of the diodes fabricated on undoped (a) and Cd-doped (b) p-Si prior to irradiation and after irradiation.*

References

[1] Ö. Güllü, M. Çankaya, M. Biber, and A. Türüt, *J. Phys. D. Appl. Phys.*, **41** (2008) 135103.

[2] S. R. Forrest and P. H. Schmidt, *J. Appl. Phys.*, **59** (1986) 513.

[3] İ. Dökme, T. Tunç, İ. Uslu, and Ş. Altındal, *Synth. Met.*, **161** (2011) 474.

[4] M. McPherson, T. Sloan, and B. K. Jones, *J. Phys. D. Appl. Phys.*, **30** (1997) 3028.

[5] R. L. Dixon, and K. E. Ekstrand, *Radiat. Protect. Dosimet.***17** (1986) 527.

[6] S. J. Moloi, and M. McPherson. *Phys. B: Condens. Matter* **404** (2009) 3922.

[7] P. G. Litovchenko, A. A. Groza, V. F. Lastovetsky, L. I. Barabash, *et al. Nucl. Instr. Meth. Phys. Res. Sect. A Accel. Spect., Detect. Assoc. Equip.*, **568** (2006) 78.

Chapter 8

Conclusions and future work

The conclusions presented in this chapter were reached after a thorough analysis of data obtained from Si wafers doped with Fe and Cd through ion implantation, as well as Schottky diodes fabricated on undoped, Fe and Cd-doped Si material. This chapter also discusses the findings of an analysis of data from devices that were irradiated with 4 MeV protons to ascertain the radiation-hardness of Si as a result of Fe and Cd doping. The focus of this research was to investigate the effects of Fe and Cd doping on the electrical characteristics of Si in the context of radiation detection applications.

8.1 Material characterisation

Material characterisation was carried out to establish the presence of the expected elements in the samples. In this study, *EDS* and *XRD* characterisation techniques were used for elemental and structural analysis of the samples, respectively. *RBS* characterisation technique was used to study the depth profile of Fe and Cd in Si.

8.1.1 *EDS* measurements

The elemental analysis of the samples using *EDS* characterisation technique confirmed the presence of the expected elements in the samples. For unimplanted samples, *EDS* results showed that Si with traces of other impurities such as oxygen and carbon were detected. For implanted samples, besides Si and traces of the impurities, Fe was only detected at the highest fluence. Cd was detected at low fluence because after implantation, Cd ions are closer to the surface of the material due to its high atomic mass, unlike Fe ions that travels deep into the material. *EDS* results show that the doping metals (Fe and Cd) are implanted in Si material.

8.1.2 *XRD* measurements

XRD analysis of the undoped samples shows two prominent peaks which was attributed to SiO_2 and Si, respectively. A low-intensity peak identified was attributed to O_2. The peaks attributed to SiO_2 and O_2 confirmed the presence of oxide layer on the surface of Si material. In the doped samples, besides the prominent peaks, other low-intensity peaks were attributed to Fe and Cd, indicating that the two dopants were fully incorporated into Si. Furthermore, a broad peak was observed on the doped samples which indicates SiO_2. However, this oxide layer does not affect the crystal structure of Si bulk. The *XRD* results show that the doping metals (Fe and Cd) are present in the Si material.

8.1.3 *RBS* measurements

The *RBS* analysis confirmed the existence of Fe and Cd at a certain depth from the surface of Si. Further, using the *RBS* technique, we determined the thickness and penetration depth of Fe and Cd in Si. The thickness of Fe and Cd in Si were calculated to be 70.32 and 103.48 nm, respectively. The depth of Fe was calculated to be 116.59 nm while the depth of Cd in Si could not be determined by *RBS* method because the simulated and experimental peaks were the same. The *RBS* analysis shows that the metals (Fe and Cd) are present in the Si material.

In general, the material characterisation results confirmed that Fe and Cd are well implanted in the Si material.

8.2 Device characterisation

Schottky diodes were well fabricated on undoped and metal (Fe- and Cd-) doped Si material. The fabricated diodes were characterised using the *I-V* and *C-V* techniques to investigate a change in diode properties as a result of metal (Fe- and Cd-) doping. Diodes that were fabricated on *n*-Si doped by Fe to different fluences (10^{15}, 10^{16}, and 10^{17} ion/cm^2) all exhibited an ohmic *I-V* behaviour. This ohmic behaviour indicates that in Si, Fe induces *g-r* centres, defect levels that are positioned at the centre of the band gap of Si. Additionally, the obtained *I-V* results indicated that in *n*-Si, Fe also generates minority carriers (holes) in *n*-Si which was responsible for a change in conductivity-type of the material from *n*-to *p*-type. At the point of conductivity-type inversion, the resistivity of the material was at maximum and the trends were ohmic for almost all through the voltage range. For *p*-Si doped by Fe, an ohmic behaviour was also observed, confirming that Fe induces *g-r* centres in Si. Further, an increase in reverse and forward current was observed, indicating that Fe is also responsible for the generation of minority and majority carriers (holes and electrons) in *p*-Si material, thereby reducing the conductivity of the Si material. For *i*-Si doped by Fe, an ohmic behaviour was also observed, confirming that Fe induces *g-r* centres in Si. Also, an increase in reverse current indicates that Fe generates more holes in Si which then recombines with electrons, resulting to increase in material resistivity.

An ohmic behaviour was observed on *p*-Si doped by Cd, indicating that Cd induces *g-r* centres in *p*-Si. In addition, Cd generates electrons which recombines with holes, hence, resulting to an increase in the resistivity of the Si material. The increased resistivity is confirmed by an increase in diode parasitic resistance. For *i*-Si doped by Cd, an ohmic behaviour was also observed, confirming that Cd induces *g-r* centres in *i*-Si. In addition, Cd generates holes in *i*-Si which recombines with electrons, thereby increasing the resistivity of the Si material.

The *C-V* results showed that Fe doping in *n*-Si diodes enables the full depletion of SCR at a reasonable voltage, indicating that doping with Fe improves the properties of diodes fabricated on *n*-Si. Furthermore, the change in conductivity-type inversion was observed on the *C-V* trend of *n*-Si doped with Fe to a fluence of 10^{16} ion/cm^2, confirming that Fe induces defect that generate holes in *n*-Si. This confirms that the results from *I-V* and *C-V* techniques complement each other. For *p*-and *i*-Si, the *C-V* results show that the capacitance increased significantly, indicating that Fe generates high density of charge carriers in the band gap of Si. Furthermore, the increase in doping concentration confirmed the high density of carriers generated by Fe in *p*- and *i*-Si diode. Furthermore, a change in conductivity-type inversion was also observed on the *p*-Si doped by Fe. The conductivity-type inversion from *p*-to-*n*-Si is due to the high density of minority carriers introduced by Fe-induced defects in Si. The increase in capacitance and doping concentration observed in the *C*-*V* results is in agreement with the increased material conductivity reported on *I*-*V* results.

The *C*-*V* results showed that Cd doping in *p*-Si diodes enables the full depletion of SCR at a reasonable voltage, indicating that doping with Cd improves the properties of diode fabricated on *p*-Si. The observed decrease in capacitance trend and doping concentration of the *p*-Si doped by Cd diode showed that Cd induces defects that generates minority carriers which recombines with majority carriers in Si. The decrease in capacitance and doping density is in agreement with the increase in material resistivity observed on *I*-*V* results. For *i*-Si, the *C*-*V* results that the capacitance increased significantly, indicating that Cd-induced defect generates high density of minority carriers in *i*-Si. Furthermore, the increase in doping concentration shows that carriers are being generated by Cd in *i*-Si diode.

8.3 Radiation-hardness test

The effect of irradiation was studied by exposing the fabricated diodes to 4 MeV proton-irradiation to ascertain their radiation-hardness due to Fe and Cd doping. *I*-*V* characteristics of the irradiated diodes showed that the effect of irradiation on the current trends has been suppressed on Fe and Cd-doped Si. The results were like those of the diodes that are resistant to radiation damage. Therefore, these metals can offer an alternative dopant to replace expensive dopants like Au and Pt. In general, both metals are promising dopants to improve the radiation-hardness of Si to be used in high energy physics experiments.

8.4 Future work

On these diodes, further characterisation techniques such as deep level transient spectroscopy (DLTS) will be done to further characterise the defects induced by the metals in the Si band gap. Furthermore, it is also imperative to characterise the diodes using the charge collection efficiency (CCE) technique to determine the detector's efficiency in collecting charges.

Appendix A

Table 6.1: The device parameters obtained from diodes fabricated on undoped *n*-Si.

	ln(*I*)-*V*			**d*V*/dln(*I*)-*I***		***H(I)-I***		***R*j-*V***	
	η	**I_s (nA)**	**ϕ_B(eV)**	**R_s (kΩ)**	**η**	**R_s (kΩ)**	**ϕ_B(eV)**	**R_{sh} (M Ω)**	**R_s (k Ω)**
Diode 1	1.11	44.00	0.70	0.05	1.38	0.17	0.71	0.98	0.20
Diode 2	1.31	20.30	0.72	0.74	2.37	1.45	0.74	5.12	2.24
Diode 3	1.27	22.90	0.72	0.22	2.43	1.14	0.78	5.72	1.51
Diode 4	1.40	30.10	0.71	0.05	2.95	0.19	0.71	5.88	0.29
Average	1.27 ± 0.10	29.33 ± 9.20	0.72 ± 0.01	0.27 ± 0.28	2.28 ± 0.57	0.74 ± 0.57	0.74 ± 0.03	4.43 ± 2.01	1.06 ± 0.86

Table 6.2: The device parameters obtained from diodes fabricated on Fe-doped *n*-Si to a fluence of 10^{15} ion/cm^2.

	ln(*I*)-*V*			**d*V*/dln(*I*)-*I***		***H(I)-I***		***R*j-*V***	
	η	**I_s (µA)**	**ϕ_B(eV)**	**R_s (kΩ)**	**η**	**R_s (kΩ)**	**ϕ_B(eV)**	**R_{sh} (M Ω)**	**R_s (k Ω)**
Diode 1	3.40	0.31	0.65	0.62	5.73	4.15	0.72	1.15	5.54
Diode 2	2.18	0.34	0.65	0.21	1.83	1.10	0.77	1.18	1.32
Diode 3	3.27	0.89	0.6 3	0.35	3.21	2.02	0.73	1.14	2.48
Diode 4	3.08	1.01	0.62	0.39	3.42	2.34	0.71	0.82	2.87
Average	2.98 ± 0.48	0.65 ± 0.32	0.64 ± 0.01	0.39 ± 0.15	3.55 ± 1.40	2.40 ± 1.11	0.73 ± 0.02	1.07 ± 0.15	3.05 ± 1.55

Table 6.3: The device parameters obtained from diodes fabricated on Fe-doped *n*-Si to a fluence of 10^{16} ion/cm^2.

	ln(*I*)-*V*			**d*V*/dln(*I*)-*I***		***H(I)-I***		***R*j-*V***	
	η	**I_s (nA)**	**ϕ_B(eV)**	**R_s (kΩ)**	**η**	**R_s (kΩ)**	**ϕ_B(eV)**	**R_{sh} (M Ω)**	**R_s (k Ω)**
Diode 1	2.34	68.90	0.73	1.65	1.84	11.88	0.91	10.43	47.28
Diode 2	2.48	68.40	0.73	3.35	1.36	26.60	0.99	10.52	55.45
Diode 3	1.90	65.70	0.75	8.93	1.72	48.23	0.96	79.68	94.03
Diode 4	2.56	108.00	0.70	6.58	1.92	11.47	0.87	24.41	104.34
Average	2.32 ± 0.25	77.75 ± 17.51	0.73 ± 0.02	5.13± 2.82	1.71 ± 0.21	24.55± 14.97	0.93± 0.05	31.26 ± 28.53	75.28 ± 24.36

Table 6.4: The device parameters obtained from diodes fabricated on Fe-doped *n*-Si to a fluence of 10^{17} ion/cm^2.

	ln(*I*)-*V*			**d*V*/dln(*I*)-*I***		***H(I)-I***		***R*j-*V***	
	η	**I_s (µA)**	**ϕ_B(eV)**	**R_s (kΩ)**	**η**	**R_s (kΩ)**	**ϕ_B(eV)**	**R_{sh} (k Ω)**	**R_s (k Ω)**
Diode 1	2.55	4.10	0.59	0.26	4.70	1.28	0.41	11.54	1.18
Diode 2	5.46	6.89	0.57	0.53	4.64	3.19	0.37	13.26	2.51
Diode 3	3.90	10.60	0.56	3.07	4.56	1.56	0.41	11.87	1.42
Diode 4	2.63	1.87	0.61	7.76	2.18	5.29	0.39	13.09	4.60

Average	3.64 ± 1.18	5.87 ± 3.26	0.58 ± 0.02	4.69± 3.01	4.02 ± 1.06	2.83 ± 1.60	0.40 ± 0.02	12.44 ± 0.75	2.43 ± 1.35

Table 6.5: The device parameters obtained from diodes fabricated on undoped *p*-Si.

	ln(*I*)-*V*			**d*V*/dln(*I*) - *I***		***H(I)-I***		***R*j-*V***	
	η	**I_s (nA)**	**ϕ_B(eV)**	**R_s (kΩ)**	**η**	**R_s (kΩ)**	**ϕ_B(eV)**	**R_{sh} (k Ω)**	**R_s (k Ω)**
Diode 1	2.50	87.41	0.65	0.48	2.34	3.01	0.77	209.65	4.44
Diode 2	2.08	47.83	0.67	0.71	3.11	4.55	0.77	213.24	4.73
Diode 3	1.77	26.82	0.68	1.31	2.44	9.83	0.79	213.24	10.20
Diode 4	3.05	128.01	0.64	0.52	3.27	3.24	0.74	203.03	3.42
Average	2.35 ± 0.48	72.52 ± 38.73	0.66 ± 0.02	0.76 ± 0.33	2.79 ± 0.41	5.16 ± 2.76	0.77 ± 0.02	209.79 ± 4.17	5.70 ± 2.64

Table 6.6: The device parameters obtained from diodes fabricated on Fe-doped *p*-Si.

	ln(*I*)-*V*			**d*V*/dln(*I*)-*I***		***H(I)-I***		***R*j-*V***	
	η	**I_s (μA)**	**ϕ_B(eV)**	**R_s (kΩ)**	η	**R_s (kΩ)**	**ϕ_B(eV)**	**R_{sh} (k Ω)**	**R_s (k Ω)**
Diode 1	2.89	8.35	0.54	0.24	0.59	1.33	0.73	2.34	1.37
Diode 2	2.94	4.75	0.55	0.34	1.11	2.14	0.73	3.47	2.21
Diode 3	2.25	3.86	0.56	0.25	0.61	1.37	0.80	2.55	1.49
Diode 4	2.50	5.91	0.54	0.22	0.45	1.24	0.81	2.16	1.27
Average	2.65 ± 0.25	6.94 ±1.58	0.55 ± 0.01	0.26 ± 0.04	0.69 ± 0.22	1.52 ± 0.32	0.77 ± 0.03	2.63± 0.45	1.59 ± 0.33

Table 6.7: The device parameters obtained from diodes fabricated on undoped *i*-Si.

	ln(*I*)-*V*			**d*V*/dln(*I*)-*I***		***H(I)-I***		***R*j-*V***	
	η	**I_s (nA)**	**ϕ_B(eV)**	**R_s (kΩ)**	η	**R_s (kΩ)**	**ϕ_B(eV)**	**R_{sh} (MΩ)**	**R_s (kΩ)**
Diode 1	1.36	1.10	0.80	4.25	1.67	35.14	0.50	115.56	25.21
Diode 2	1.80	3.39	0.77	5.66	1.52	45.05	0.65	80.85	46.93
Diode 3	1.62	3.28	0.76	4.58	1.45	37.54	0.70	71.19	37.08
Diode 4	1.83	3.33	0.77	2.12	1.51	11.91	0.78	105.44	30.48
Average	1.65 ± 0.19	2.78 ± 0.97	0.78 ± 0.02	4.15 ± 1.28	1.54 ± 0.08	32.41 ± 12.39	0.66 ± 0.10	93.26 ± 17.94	34.93 ± 8.11

Table 6.8: The device parameters obtained from diodes fabricated on Fe-doped *i*-Si.

	ln(*I*)-*V*			**d*V*/dln(*I*)-*I***		***H(I)-I***		***R*j-*V***	
	η	**I_s (μA)**	**ϕ_B(eV)**	**R_s (kΩ)**	η	**R_s (kΩ)**	**ϕ_B(eV)**	**R_{sh} (kΩ)**	**R_s (kΩ)**
Diode 1	2.63	0.56	0.62	0.56	0.77	3.72	0.94	29.00	13.78
Diode 2	2.18	0.02	0.72	1.43	3.43	9.92	0.85	465.26	16.68
Diode 3	2.24	0.04	0.70	1.56	2.52	11.17	0.87	244.69	13.92
Diode 4	4.63	0.47	0.64	0.66	2.85	4.20	0.80	89.74	15.29

Average	2.92± 1.00	0.27 ± 0.24	0.67 ± 0.04	1.05 ± 0.45	2.39 ± 0.99	7.25 ± 3.33	0.87 ± 0.05	207.17± 168.49	14.92 ± 1.18

Table 6.9: The device parameters obtained from diodes fabricated on Cd-doped *p*-Si.

	ln(*I*)-*V*			**d*V*/dln(*I*)-*I***		***H(I)-I***		***R*j-*V***	
	η	**I_s (nA)**	**ϕ_B(eV)**	**R_s (kΩ)**	η	**R_s (MΩ)**	**ϕ_B(eV)**	**R_{sh} (M Ω)**	**R_s (kΩ)**
Diode 1	3.38	0.05	0.84	866.30	3.62	17.70	0.94	316.94	19.10
Diode 2	2.96	0.01	0.89	751.12	3.15	12.90	1.09	302.63	17.46
Diode 3	3.56	0.34	0.80	251.46	6.89	5.50	0.45	125.65	10.42
Diode 4	3.34	0.29	0.80	378.79	3.42	7.79	1.04	94.29	9.29
Average	3.31 ± 0.22	0.17 ± 0.14	0.83 ± 0.04	561.92 ± 254.15	4.27 ± 1.52	10.97 ± 4.72	0.88 ± 0.25	209.88 ± 100.65	14.07 ± 4.24

Table 6.10: The device parameters obtained from diodes fabricated on Cd-doped *i*-Si.

	ln(*I*)-*V*			**d*V*/dln(*I*)-*I***		***H(I)-I***		***R*j-*V***	
	η	**I_s (μA)**	**ϕ_B(eV)**	**R_s (kΩ)**	η	**R_s (kΩ)**	**ϕ_B(eV)**	**R_{sh} (MΩ)**	**R_s (kΩ)**
Diode 1	5.26	0.99	0.62	4.94	1.35	33.45	0.55	1.22	31.20
Diode 2	2.92	0.31	0.65	4.7	0.99	37.72	0.58	1.13	35.53
Diode 3	6.25	0.55	0.64	6.72	0.57	61.91	0.67	1.12	57.71
Diode 4	4.82	0.95	0.62	4.38	1.32	38.04	0.59	1.13	27.78
Average	4.81 ± 1.21	0.70 ± 0.28	0.63 ± 0.01	5.19± 0.19	1.06 ± 0.31	42.78 ± 11.19	0.60 ± 0.04	1.15 ± 0.04	38.06 ± 11.68

Appendix B

Materials Science in Semiconductor Processing 123 (2021) 105524

Contents lists available at ScienceDirect

Materials Science in Semiconductor Processing

journal homepage: http://www.elsevier.com/locate/mssp

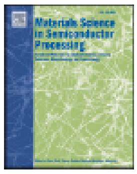

Current-voltage characteristics of iron-implanted silicon based Schottky diodes

J.O. Bodunrin, D.A. Oeba, S.J. Moloi *

Department of Physics, College of Science, Engineering and Technology, University of South Africa, Private Bag X6, Florida, 1710, South Africa

ARTICLE INFO

Keywords:
Silicon
Diode
Ohmic I–V
Radiation detectors

ABSTRACT

Current-voltage (*I–V*) measurements were carried out on undoped and iron (Fe) doped *n*-silicon (*n*-Si) to establish and study a change in electrical properties of the material-based diodes with Fe doping concentration. Fe doping was achieved by implantation at the energy of 160 keV to fluences of 10^{15}, 10^{16} and 10^{17} ion/cm^2. The obtained results indicated that the diodes were well fabricated and Fe doping resulted in a diode behaviour changing from normal exponential to ohmic *I–V* behaviour. This ohmic behaviour was explained in terms of Fe-induced defect levels that were positioned at the centre of the energy gap. An *I–V* ohmic region increased with fluence indicating that the density of defect levels has increased with Fe implantation fluence. A change in diode conduction mechanism domination and parameters with fluence were investigated. The obtained *I–V* properties of Fe doped Si-based diodes were similar to those of the diodes that were fabricated on radiation-hard materials indicating that Fe, too, is a promising dopant in a quest to improve radiation-hardness of Si to be used in high energy physics experiments.

1. Introduction

Crystalline silicon is used for fabrication of radiation detectors in high energy physics experiments due to its unique advantages like moderate energy gap, stability in high temperature and cost-friendly due to its abundance in nature, to mention the few. Detectors that are made from this material, however, gets damaged by the same radiation they intend to detect. The damage results in defect levels in the energy gap of Si that are responsible for a change in the microscopic properties of detectors. It is therefore important that radiation-hardness of Si is improved to make the material suitable for the fabrication of efficient radiation detector to be used in the current and future high energy physics experiments [1].

In trying to improve radiation-hardness of the material, numerous studies have shown that a heavy pre-irradiation [2] oxygenation [3] and doping Si with metals such as gold (Au) and platinum (Pt) [4] are promising methods. In Si, Au and Pt were found to be responsible for relaxation behaviour of the material [5] but they are, however, relatively expensive resulting in very limited research on radiation-hardness of Si. It is, therefore, important that the effects of other metal dopants in Si are established and studied. These dopants should be abundant and have similar behaviour as Au and Pt in Si.

In *p*-Si, Fe acts as donor impurity consequently reducing the concentration of holes [6], hence, reducing the conductivity of the material. The resistivity of *n*-Si, on the other hand, has been found to remain unchanged after doping with Fe concentration of 10^{14} cm^{-3} [7]. Based on the literature reviewed, the effects of Fe on electrical properties of Si at a concentration higher than 10^{14} cm^{-3} have not been studied. In Si, Fe creates defect levels at E_V +0.40, E_C -0.55 and E_C -0.27 eV in the energy gap [8]. The main motive of studying the effects of Fe dopants in Si is due to ~0.55 eV defect level, which was found to be induced by Au and Pt [9,10]. A defect level at ~0.56 eV in the energy gap is responsible for relaxation behaviour of Si [11]. Devices fabricated on relaxation material show ohmic *I–V* behaviour [5,11] and they have been proven to be resistant to radiation damage [12]. These devices, however, have high leakage current showing that their radiation detection sensitivity is low. This shortfall encourages a search of the most suitable dopant to improve Si properties for radiation detection applications.

In this work, diodes were characterized using *I–V* technique to investigate the effects of Fe doping on the electrical properties of Si-based devices. The results indicate, for the first time, that in Si, Fe exhibits similar properties as other metals (Au and Pt) that have been found promising to improve radiation-hardness of Si. Hence, Fe could be a suitable replacement in case these two metals are disqualified due to

* Corresponding author.
E-mail address: moloisj@unisa.ac.za (S.J. Moloi).

https://doi.org/10.1016/j.mssp.2020.105524
Received 24 April 2020; Received in revised form 6 September 2020; Accepted 20 October 2020
Available online 4 November 2020

Appendix C

Sensors and Actuators A 331 (2021) 112957

Contents lists available at ScienceDirect

Sensors and Actuators A: Physical

journal homepage: www.elsevier.com/locate/sna

Current-voltage and capacitance-voltage characteristics of cadmium-doped p-silicon Schottky diodes

J.O. Bodunrin, D.A. Oeba, S.J. Moloi*

Department of Physics, College of Science, Engineering and Technology, University of South Africa, Private Bag X6, Florida, 1710, South Africa

ARTICLE INFO

Article history:
Received 20 January 2021
Received in revised form 8 June 2021
Accepted 28 June 2021
Available online 5 July 2021

Keywords:
Silicon
Cadmium-doping
Schottky diodes
Current
Capacitance
Resistivity
Radiation detectors

ABSTRACT

This study reports on a change in current-voltage (*I–V*) and capacitance-voltage (*C–V*) characteristics of silicon (Si) diodes due to doping Si with cadmium (Cd). Effects of Cd-doping on diode parameters and conduction mechanism are investigated. The results obtained here indicate that the diodes are well fabricated and introducing Cd in Si results in a diode *I–V* behaviour changing from normal exponential to ohmic. An ohmic behaviour indicates that the diode conduction mechanism is dominated by defect levels at the centre of the Si energy gap. These defects are responsible for generation of minority carriers to recombine majority carriers resulting in an increase in material resistivity. A change in a direction of a *C–V* trend showing an inversion of a material conductivity-type confirms the generation of minority carriers after doping Si with Cd. A high resistivity material is important for radiation detection since a full space charge region width can be attained at a reasonable operating voltage. The ohmic behaviour and a conductivity-type inversion have been observed on diodes that are resistant to radiation damage. Cd is, therefore, a suitable dopant in defect-engineering studies to improve radiation hardness of Si for high energy physics experiments.

1. Introduction

Using Si-based detectors in high energy physics experiments (HEPE) is of great interest due to the qualities that are possessed by Si. Qualities such as abundance in nature, a reasonable energy gap, a possibility of changing the material properties by doping, a presence of natural oxide, and microscopic structuring [1] make Si a suitable material for fabrication of radiation detectors and other electronic devices. Despite these qualities, detector performance degrades during the operation due to defect levels that are created in the Si energy gap. These levels change the electrical properties of the detectors [2], resulting in instability and unreliability of detectors when used in extreme radiation environments. The detectors cannot meet future demands, like in Large Hadron Collider experiments, where they would be expected to operate in environments harsher than the current ones [3].

To improve the efficiency of Si detectors operating in extreme radiation environments, defect-engineering of Si has been a promising method [4]. The method involves a deliberate introduction of defects in a controllable manner such that the desired properties are improved while the unfavourable ones are minimized or suppressed. Gold (Au) and platinum (Pt) are promising dopants to improve the properties of Si for the fabrication of an efficient radiation detector [5,6]. However, these metals, Au and Pt, are relatively expensive for studies, and their diffusion mechanisms in Si are not fully understood to associate the induced crystal defects with the formed levels in the energy gap. In addition, doping Si with Au and Pt results in a high leakage current of the detector, limiting the radiation sensitivity of the material-based detector [6]. It is, therefore, important to establish a relatively cheap alternative dopant to improve radiation-hardness of Si. Material resistivity needs to be increased to attain a full space charge region (SCR) width of the detector at a reasonable low voltage.

Cd is a group II element with electronic configuration (Kr)$4d^{10}5s^2$ having two valence electrons. Acceptor levels induced by Cd at $E_C - 0.54$ eV and at $E_C - 0.33$ eV in the energy gap are attributed to substitutional Cd in Si [7]. Similar to Au and Pt, Cd is a lifetime killer and it creates recombination centres in Si [8]. It is, therefore, expected that a free charge carrier density will reduce, resulting in an increase in the resistivity of Si after doping with Cd. Shallow donors, in contrast, are attributed to the intrinsic interstitial Cd atoms and oxygen vacancies in Si [9,10]. The donors are expected to increase the resistivity of *p*-Si. A study of the electrical character-

* Corresponding author.
E-mail address: moloisj@unisa.ac.za (S.J. Moloi).

https://doi.org/10.1016/j.sna.2021.112957
0924-4247/

Appendix D

Solid State Communications 341 (2022) 114575

Contents lists available at ScienceDirect

Solid State Communications

journal homepage: www.elsevier.com/locate/ssc

Electrical properties and conduction mechanisms of heavily iron implanted silicon diodes

J.O. Bodunrin, S.J. Moloi *

Department of Physics, College of Science, Engineering and Technology, University of South Africa, Private Bag X6, Florida, 1710, South Africa

ARTICLE INFO

Communicated by: Bell Gavin

Keywords:
Silicon
Defect-engineering
Device fabrication
Electrical characterisation
Radiation sensors

ABSTRACT

A change in current-voltage (*I–V*) and capacitance-voltage (*C–V*) properties of silicon (Si) diodes due to the doping of the material with iron (Fe) is presented. The deviation of diode *I–V* behaviour from normal exponential to ohmic behaviour indicates that the conduction mechanism is dominated by generation-recombination (*g-r*) centres after Fe doping. The effects of *g-r* centres are more pronounced at low-frequency *C–V* measurements, where the low-mobility minority carriers are active. Due to the recombination of charge carriers, the charge ejection rate out of the space charge region (SCR) is low and less dependent on frequency measurements, possibly, showing that as they dominate the conduction mechanism, *g-r* centres are stable at one level in the band gap of Si. The results presented here are very important since they explain the properties of *g-r* centres and they show that in Si, Fe exhibits properties similar to dopants (Au and Pt) found responsible for the improvement of Si radiation-hardness.

1. Introduction

Silicon radiation detectors are devices used for scientific research in astrophysics, nuclear physics, and high-energy physics experiments [1–3]. The detectors have been preferred among others because of the material thermal stability, making the detectors operate at a temperature higher than room temperature. They are also mechanically rigid, needing no special supporting structures during operation. The large density of Si offers average energy loss per unit length, which makes the production of thin detectors a possibility without losing the ability to produce measurable signals [4]. Despite all these unique advantages, the performance of these devices gets deteriorated by the same radiation they intend to detect. This failure is attributed to defect levels created within the band gap of Si by incident radiation. The radiation-induced defect levels change electrical properties, hence, the instability of the detectors when exposed to extreme radiation conditions [5,6]. The performance, therefore, of the detectors needs to be improved for current and future use.

Studies have shown that the desired performance of the detectors can be achieved by engineering defects in Si through doping [7–9]. In these studies, defects in Si are introduced in a controllable manner such that the material properties are improved for radiation sensing applications. A controllable manner, implies the dopants, the density of the dopants, and the doping method [7,8]. As it is found to improve radiation-hardness, however, doping also increases the leakage current, limiting the radiation sensitivity of the material-based detectors. Further studies on defect-engineering are necessary to have the sensitivity of the devices not compromised at the expense of radiation-hardness of Si.

Gold (Au) and platinum (Pt) are promising dopants to improve the properties of Si for the fabrication of stable detectors during operation [7,8]. The improvement of the properties is associated with midgap defect (0.56 eV), a defect level positioned at the centre of the band gap, created by Au and Pt. This level is responsible for ohmic *I–V* diode behaviour since at this position the charge generation rate (g) is the same as the recombination rate (r). Thus, the Fermi energy of the material with a high density of midgap defects is pinned at an intrinsic position. At this position, the Fermi energy is independent of incident radiation [10]. However, Au and Pt create other defect levels that are responsible for a change in conductivity, rendering the material useless for radiation detecton applications. This shortcoming has initiated an urgent need to find other suitable dopants in a study to improve the properties of Si for radiation detection applications.

Iron (Fe) as a common element in nature that belongs to the transition metal group can be introduced into Si crystals [11]. Fe introduces deep levels into the band gap of Si generating minority carriers in *n*-Si material [12]. These minority carriers recombine with the excess

* Corresponding author.
E-mail address: moloisj@unisa.ac.za (S.J. Moloi).

https://doi.org/10.1016/j.ssc.2021.114575
Received 3 May 2021; Received in revised form 13 September 2021; Accepted 21 October 2021
Available online 23 October 2021

Appendix E

Silicon
https://doi.org/10.1007/s12633-022-01767-8

ORIGINAL PAPER

Current-Voltage Characteristics of 4 MeV Proton-Irradiated Silicon Diodes at Room Temperature

J. O. Bodunrin [1] · S. J. Moloi [1]

Received: 11 January 2022 / Accepted: 15 February 2022

Abstract
A change in current-voltage (*I-V*) behaviour of the *p*-Si-based diodes as a result of 4 MeV proton-irradiation to the fluence of 10^{16} p/cm^{-2} was investigated using *I-V* techniques at room temperature. The diode *I-V* behaviour changed from normal exponential to ohmic behaviour after proton-irradiation, indicating that proton introduce generation-recombination (*g-r*) centres, defect levels that are positioned in the middle of the band gap of Si. These centres recombine mobile charge carriers, thereby, reducing the concentration of carriers through the space charge region (SCR). The reduction of the concentration results in an increase in material resistivity as confirmed by the increase in series resistance after proton-irradiation. Furthermore, a change in diode parameters such as saturation current (I_s), ideality factor (η), Schottky barrier height (ϕ_b), and series resistance (R_s) due to the irradiation is also investigated. A change in diode parameters and conduction mechanism due to proton-irradiation presented in this work is of great importance for an ongoing study on radiation-induced damages and radiation-hardness of Si material.

Keywords Si-based diode · Proton damage · Current-voltage · Series resistance · Rectification ratio · Conduction mechanism

1 Introduction

Silicon radiation detectors are used in outer space probes in astronomy [1], monitoring nuclear weapons in the military [2], radiation dosimetry in medical applications [3], and detection of new particles in high energy physics experiments [4]. Si as a preferred material to fabricate detectors has gained more attention due to their scientific interest and technological advancement. Its advantages over other semiconductors include susceptibility to miniaturization, well-known technology, decent band gap, abundance in nature making it available at affordable cost, fast signal response, good intrinsic detection efficiency, and low voltage operation [5]. However, the diodes fabricated from Si material tends to get damaged by the incident radiation they are meant to detect. The damage is due to radiation-induced defects that result in defect levels in the band gap [6]. These defect levels change the electrical properties of Si-based diodes [7]. It is, therefore, a necessity to improve the radiation-hardness of Si to make the material suitable for the fabrication of efficient radiation detectors to be used in the current and future high energy physics experiments, thereby, making the Si-based detectors stable and efficient under harsh radiation environments [8].

A heavy Pre-irradiation has been identified as one of the effective ways of improving the radiation-hardness of Si [9, 10]. Although studies on radiation-damaged Si have been ongoing for so long, the electrical properties of the irradiated detectors have not been fully understood nor explained, hence impossible to fabricate detectors that would meet the current and future demands. Furthermore, a study on a change in the conduction mechanisms of the detector due to radiation is so insufficient to understand the properties of irradiation-induced defects in Si [11].

Devices that show high resistivity and ohmic *I-V* behaviour have been reported to be resistant to radiation damage [6, 10–13], indicating an improvement in the radiation-hardness of Si material-based devices. An increase in the material resistivity as a result of incident radiation was reported on Si-based devices irradiated by neutrons [14] and protons [15]. The increase in the resistivity was explained in terms of the defects introduced by radiation which acts as recombination centres thereby recombining with charge carriers and reducing the concentration of charge carriers in the space charge region (SCR) [14, 15]. Also, a rapid decrease in forward current was

✉ J. O. Bodunrin
bodunrinjoseph01@gmail.com

[1] Department of Physics, College, Science, Engineering and Technology, University of South Africa, Private Bag X6, Florida 1710, South Africa

Published online: 22 February 2022